

---

# Bohmian Trajectories in a Double Slit Experiment

Carlotta Versmold

---



München, Februar 2021

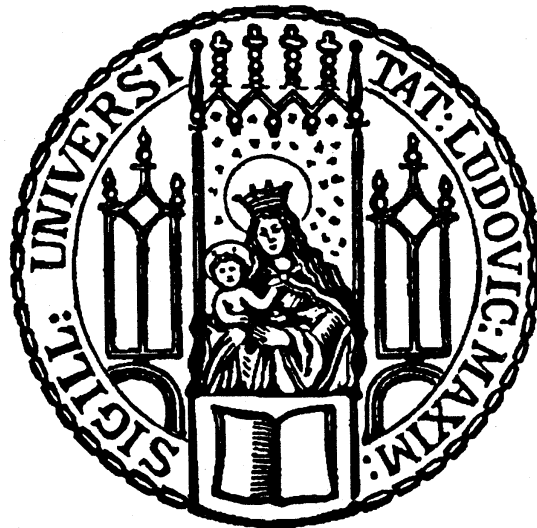


---

# Bohmian Trajectories in a Double Slit Experiment

Carlotta Versmold

---



Munich, 15<sup>th</sup> of February 2021

Master Thesis  
Faculty of Physics  
Ludwig-Maximilians-Universität  
Munich

handed in by  
Carlotta Versmold  
from Munich

supervised by  
Prof. Dr. Harald Weinfurter

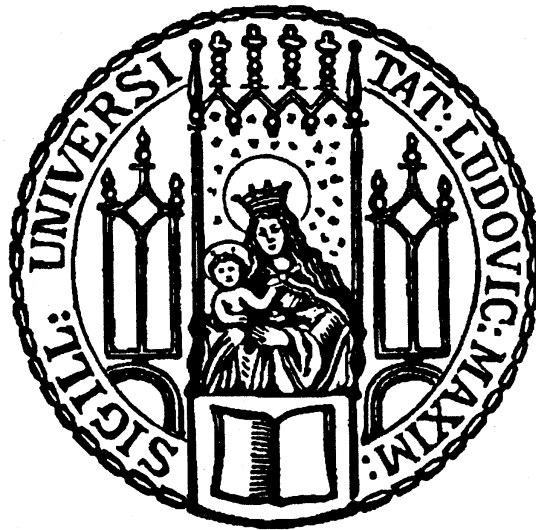


---

# Bohmsche Trajektorien im Doppelspaltexperiment

Carlotta Versmold

---



München, 15. Februar 2021

Masterarbeit  
an der Fakultät für Physik  
der Ludwig-Maximilians-Universität  
München

vorgelegt von  
Carlotta Versmold  
aus München

Betreuer der Arbeit:  
Prof. Dr. Harald Weinfurter



# Abstract

Bohmian mechanics is one of many alternative interpretations of quantum mechanics. Attributing a definite position to particles at all times it allows the introduction of particle trajectories, which are forbidden in orthodox quantum mechanics. In order to investigate the non-locality of this theory we are implementing an experiment where one photon, initially entangled with another photon, is sent through a double slit apparatus, where its average Bohmian trajectory can be observed. This will enable us to analyze different cases where the state and possible evolution of the interfering photon depend on the observation of the second photon.

The work in this thesis focuses on the creation of an entangled photon source, where the entanglement is created via spontaneous parametric down conversion in a PPKTP crystal and the special arrangement of birefringent crystals which results in a Bell state, entangled in polarization. The double slit setup is also built exploiting the anisotropy of birefringent crystals, which separate a single incoming beam into two orthogonally polarized ones, such that the photon's which-way-information depends on its initial polarization or the observation of the entangled photon, respectively. The average trajectories in the interference region can be measured via weak measurement. This technique makes it possible to obtain information about the system without changing it significantly. This is at the expense of the amount of information obtained, so that a large number of such measurements is needed. By varying the point in time of the polarization-measurement of the second photon, delayed choice measurements can be performed.

Average trajectories have already been measured in experiments and are shown to correspond with those calculated in the Bohmian theory. Nevertheless, the meaning of average trajectories and Bohmian mechanics is much discussed. This experiment will soon contribute to a better understanding of this theory.



# Contents

<b>Abstract</b>	<b>vii</b>
<b>Introduction</b>	<b>1</b>
<b>1 Standard quantum mechanics and quantum measurement</b>	<b>3</b>
1.1 Fundamentals of quantum mechanics . . . . .	3
1.1.1 Quantum states in a hilbert space . . . . .	3
1.1.2 Composite systems . . . . .	7
1.2 Quantum measurement . . . . .	9
1.2.1 Projective measurement . . . . .	9
1.2.2 Indirect measurement . . . . .	10
1.3 Pre- and postselected systems . . . . .	13
1.3.1 Two-state vector formalism . . . . .	13
1.3.2 Measurements on pre- and postselected systems . . . . .	14
1.4 Weak value formalism . . . . .	15
1.4.1 Definition of the weak value . . . . .	15
1.4.2 Unusual properties . . . . .	17
<b>2 Bohmian mechanics and the double slit experiment</b>	<b>19</b>
2.1 Bohmian mechanics . . . . .	19
2.1.1 Criticism on standard quantum mechanics . . . . .	19
2.1.2 Non-local hidden variables . . . . .	22
2.1.3 Mathematical description of the Bohmian theory . . . . .	23
2.2 The Double slit experiment . . . . .	26
2.2.1 Standard quantum mechanics explanation . . . . .	27
2.2.2 Bohmian mechanics explanation . . . . .	27
2.3 Observing Bohmian trajectories . . . . .	36
2.3.1 Bohmian velocity as a weak value . . . . .	36
2.3.2 Poynting vector as Bohmian velocity . . . . .	37
2.3.3 Uncertainty analysis . . . . .	38
2.3.4 Demonstration of a wavefront measurement . . . . .	41
<b>3 Experimental implementation</b>	<b>45</b>
3.1 Optics . . . . .	45
3.1.1 Gaussian beam . . . . .	45
3.1.2 Optical components . . . . .	46
3.2 Birefringence and nonlinear optics . . . . .	48
3.2.1 Propagation of polarized light in birefringent crystals . . . . .	49
3.2.2 Principle of spontaneous parametric down-conversion . . . . .	51

## Contents

---

3.2.3	Spatial analysis of SPDC processes in biaxial crystals . . .	53
3.3	Experimental setup . . . . .	59
3.3.1	Double slit setup . . . . .	59
3.3.2	Weak measurement implementation . . . . .	60
3.3.3	Entangled photon source setup . . . . .	61
3.3.4	Tomography and Coincidence Detection . . . . .	65
<b>4</b>	<b>Alignment of the photon source</b>	<b>69</b>
4.1	Beam focus alignment . . . . .	69
4.2	Angular and spatial overlap of the beams . . . . .	74
4.3	Sources of coherence reduction . . . . .	76
4.3.1	Tilted crystals . . . . .	77
4.3.2	Collection of different wavelengths . . . . .	77
4.4	Increasing coherence . . . . .	79
4.5	Final state tomography . . . . .	83
	<b>Conclusion</b>	<b>85</b>
	<b>Abbreviations</b>	<b>87</b>
	<b>Bibliography</b>	<b>91</b>
	<b>Acknowledgments</b>	<b>99</b>
	<b>Declaration of authorship</b>	<b>101</b>

# Introduction

Since the discovery of quantum phenomena in the beginning of the 20th century there was an ongoing debate about different interpretations of quantum theory. Finally, standard quantum mechanics (SQM) with the Copenhagen interpretation became the most accepted theory. Nevertheless, most of the alternative theories were never disproved and are still vivid. One among these is Bohmian mechanics (BM) [1, 2], a non-local realistic theory which owes its realism to the introduction of the particle positions as hidden variables. In contrast to the probabilistic Copenhagen interpretation BM is governed by determinism. Thus, the theory is able to satisfy the desire for a non-probabilistic and realistic quantum theory which was expressed by many physicists.

Even though all imaginable experiments lead to the same results as in SQM when considered in the Bohmian theory, the way of explaining the occurrence of the results is different, leading to new perspectives on well-known experiments. The most controversial experiment since the early days of quantum mechanics has always been the double-slit interferometer, holding the “mystery” [3] of quantum mechanics. Therein, the different interpretations of quantum mechanics also become clear. While SQM bases the observation of the interference pattern on the wave-particle duality, in BM it appears because actual quantum particles, which are following trajectories guided by the wavefunction, arrive at a determined position at the screen, resulting in an interference pattern.

Inspired by a gedanken experiment from 1992 [4], the average Bohmian trajectories in a double slit were observed by an quantum optical implementation of the theory of weak measurements [5, 6], while which-way measurements on the involved particles were performed [7], leading to a deeper understanding of the Bohmian theory. Nevertheless, which-way measurements on particles in the interference region have never been actually performed.

The experiment related to this thesis performs such kind of measurement, investigating the non-locality of BM: a polarizationally entangled photon pair is separated such that one photon is entering a double slit, where its trajectories are observed. The interferometer is constructed in a manner that the traversed slit is entangled with the polarization of the second photon. On this second photon, outside the double slit interferometer, polarization measurements are performed, realizing which-way measurements on the photon traversing the slits and the interference region. Since the moment of the polarization measurement on the second photon can be chosen arbitrarily with respect to the first particle crossing the interference region, this experiment enables to switch between interfering and non

## Introduction

---

interfering measurement scenarios and makes delayed choice experiments possible. For this an efficient entangled photon source is required, the implementation of which will be the main aim of this thesis.

The thesis begins with an introduction to SQM, quantum measurement and especially the weak value formalism in order to provide a basis for the following considerations. This is followed by an explanation of Bohmian theory as an alternative of SQM and the double slit experiment in this context. Furthermore, different possibilities to observe Bohmian trajectories are investigated. The next chapter then treats the experimental realization of the setup with a special focus on the implementation of the photon source, producing the pairs of polarizationally entangled photons later sent to the double slit and the polarization measurement. This is why the following chapter explains the techniques used for a proper alignment of the source and occurring difficulties. It also contains the final state tomography, characterizing the generated Bell state.

# 1 Standard quantum mechanics and quantum measurement

In order to provide a conceptual mathematical foundation for this thesis, in this chapter a brief summary about the fundamental concepts of standard quantum mechanics (SQM) is given, mainly based on [8–10]. Special attention is paid to quantum measurements in order to later derive the weak value formalism.

## 1.1 Fundamentals of quantum mechanics

### 1.1.1 Quantum states in a hilbert space

**Hilbert space** A Hilbert space  $\mathcal{H}$  is a complex vector space, whose dimension is specified by the physical nature of the system under consideration, with an inner product  $\langle \cdot, \cdot \rangle$ , which is complete. A physical state is represented by a state vector in an Hilbert space and is called, according to Dirac [11], a ket  $|v\rangle \in \mathcal{H}$ .

Those state vectors contain complete information about the physical state, and all linear combinations of the elements  $\{|v_i\rangle\} \in \mathcal{H}$  are again elements of the same vector space

$$|w\rangle = \sum c_i |v_i\rangle \in \mathcal{H}, \quad c_i \in \mathbb{C}, \quad (1.1)$$

from which it can be deduced that any superposition of states is another possible state of the quantum system, the so called *superposition principle*.

The inner product  $\langle v, w \rangle$  between two elements of the Hilbert space  $|v\rangle$  and  $|w\rangle$  is written as

$$\langle v, w \rangle := \langle v|w\rangle, \quad (1.2)$$

where the bra vector  $\langle v|$  is the element of the dual space corresponding to  $|v\rangle$ . The inner product has to be linear in the second argument, skew-symmetric, which means that  $\langle v|w\rangle$  is the complex conjugate to  $\langle w|v\rangle$ , and positive semi-definite  $\langle v|v\rangle \geq 0$ , which only becomes zero when  $|v\rangle = 0$ .

This induces firstly that two elements of a Hilbert space are orthogonal if and only if their inner product  $\langle v|w\rangle = 0$  and, secondly, that the norm  $|||v\rangle||$  is defined via

$$|||v\rangle|| := \sqrt{\langle v|v\rangle}. \quad (1.3)$$

Therefore, any non-zero vector can be normalized by dividing it by its norm. [12]

## 1 Standard quantum mechanics and quantum measurement

---

It is also possible to express a state of an infinite-dimensional Hilbert space in terms of a continuous basis  $\{|x\rangle\}$

$$|u\rangle = \int dx f(x)|x\rangle, \quad (1.4)$$

where in comparison to Eq. (1.1) the sum over the complex amplitudes  $c_i$  and the discrete basis is exchanged by an integral over the continuous space of the *wavefunction*  $f(x)$  often denoted with  $\psi(x) = \langle\psi|x\rangle$ .

**Operators** Another important class of objects are linear operators  $\hat{A}$  representing functions  $\hat{A} : \mathcal{H} \rightarrow \mathcal{H}$  which are linear in their inputs and act on states of the Hilbertspace

$$\hat{A} \left( \sum_i c_i |v_i\rangle \right) = \sum_i c_i \hat{A} |v_i\rangle. \quad (1.5)$$

The adjoint  $A^\dagger$  is defined via the dual space with

$$\hat{A}|v\rangle \leftrightarrow \langle v|\hat{A}^\dagger. \quad (1.6)$$

The addition of operators is commutative, associative and, in general, the commutator of two linear operators  $[\hat{A}, \hat{B}] = \hat{A}\hat{B} - \hat{B}\hat{A}$  is nonzero and the unity operator  $\mathbb{1}$  is defined as  $\mathbb{1}|v\rangle = |v\rangle$ .

Furthermore, an eigenstate  $|a\rangle$  of an operator  $\hat{A}$ , which plays an important role especially for quantum measurement, is defined together with its corresponding eigenvalue  $a$  via

$$\hat{A}|a\rangle = a|a\rangle. \quad (1.7)$$

The subspace of  $\mathcal{H}$  spanned by all eigenvectors of  $\hat{A}$  with one particular eigenvalue is called an eigenspace of operator  $\hat{A}$  corresponding to this certain eigenvalue.

There are different kinds of linear operators. Physical observables are represented by linear hermitian operators  $\hat{O}$ , where  $\hat{O} = \hat{O}^\dagger$  has only real eigenvalues. A special kind of observable is the so called projector  $\hat{\Pi}$ , which is a bounded hermitian operator with eigenvalues only 0 and 1; it is characterized by  $\hat{\Pi}^2 = \hat{\Pi} = \hat{\Pi}^\dagger$ .

**Evolution of a quantum state** A state of a closed quantum system evolving in time is described by the *Schrödinger equation*

$$i\hbar \frac{d|\psi\rangle}{dt} = \hat{H}|\psi\rangle, \quad (1.8)$$

where  $\hbar$  is Planck's constant and  $\hat{H}$  is the hamiltonian of the system, a hermitian operator. The evolution of the system is hence described by a unitary operator  $\hat{U}$  via

$$|\psi(t_2)\rangle = \hat{U}(t_1, t_2)|\psi(t_1)\rangle = e^{-\frac{i\hat{H}(t_2-t_1)}{\hbar}}|\psi(t_1)\rangle. \quad (1.9)$$

**Density matrix formalism** Besides the description by a normalized state vector, quantum states can also be described by a *density matrix*. The density operator  $\hat{\rho}$  of a state  $|\psi\rangle$  is

$$\hat{\rho} = |\psi\rangle\langle\psi|. \quad (1.10)$$

Density operators are by construction hermitian, positive semi-definite and have a normalized trace  $tr(\hat{\rho}) = 1$ . Moreover, density operators allow the representation of mixed states, which cannot be described in terms of vector states. In the state vector formalism quantum states can only be described completely by a combination of quantum states, whereas in the density operator formalism also scenarios where the physical state is in a statistical uncertainty can be described. The state of the system is then not completely known but can still be represented by a density matrix of the form

$$\hat{\rho} = \sum_i P_i |\psi_i\rangle\langle\psi_i|. \quad (1.11)$$

Here  $P_i$  is the probability of the system to be in the state  $|\psi_i\rangle$ . States which completely describe the system can be expressed by state vectors or density operators via an outer product as in Eq. (1.10) and are called *pure states*, while systems in a state of statistical uncertainty are *mixed states*.

**Qubit system** A minimum quantum system is a quantum bit or *qubit* system which is described by a 2-dimensional Hilbertspace with the principal orthonormal basis states  $|0\rangle$  and  $|1\rangle$ . In contrast to classical bits, which can only have the value 0 or 1, qubits can be – thanks to the superposition principle – in any normalized superposition state

$$|\psi\rangle = a|0\rangle + \beta|1\rangle, \quad (1.12)$$

with  $|a|^2 + |\beta|^2 = 1$ . Because of the normalization, it is also possible to write Eq. (1.12) as

$$|\psi\rangle = \cos\left(\frac{\theta}{2}\right)|0\rangle + e^{i\varphi}\sin\left(\frac{\theta}{2}\right)|1\rangle. \quad (1.13)$$

This state defines a point on the 3-dimensional Bloch-sphere (see Fig. 1.1). A possible basis for linear operators acting on the qubits is  $\{\mathbb{1}, \hat{\sigma}_x, \hat{\sigma}_y, \hat{\sigma}_z\}$  also often indicated as  $\{\hat{\sigma}_0, \hat{\sigma}_1, \hat{\sigma}_2, \hat{\sigma}_3\}$ , where  $\hat{\sigma}_i$  denote the Pauli matrices

$$\hat{\sigma}_x = \begin{pmatrix} 0 & 1 \\ 1 & 0 \end{pmatrix}, \quad \hat{\sigma}_y = \begin{pmatrix} 0 & -i \\ i & 0 \end{pmatrix}, \quad \hat{\sigma}_z = \begin{pmatrix} 1 & 0 \\ 0 & -1 \end{pmatrix}. \quad (1.14)$$

With this, any qubit state can be decomposed in the density operator representation into a superposition of operators via

$$\hat{\rho} = \frac{\mathbb{1} + \mathbf{n}\hat{\boldsymbol{\sigma}}}{2}, \quad (1.15)$$

where  $\mathbf{n}\hat{\boldsymbol{\sigma}} = \sum_i n_i \hat{\sigma}_i$  and  $\mathbf{n}$  is the state vector in the 3D Bloch sphere with  $|\mathbf{n}|^2 \leq 1$ , denoted as *Bloch vector*

$$\mathbf{n} = \begin{pmatrix} \cos\theta \sin\varphi \\ \sin\theta \sin\varphi \\ \cos\theta \end{pmatrix}. \quad (1.16)$$

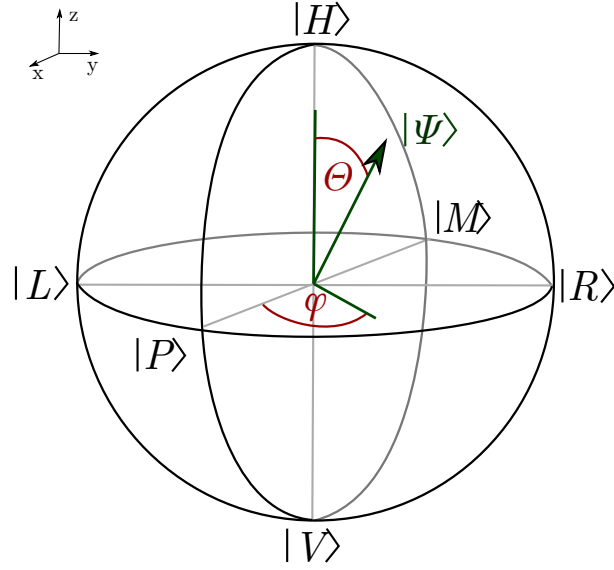


**Figure 1.1:** Description of a state  $|\psi\rangle$  on the Bloch sphere via its polar angle  $\varphi$  and its azimuthal angle  $\theta$ .

It can be shown that the components  $n_i$  correspond to the expectation value of a measurement of  $\langle \hat{\sigma}_i \rangle$ . Pure states lie on the surface of the sphere and thus have  $\|\mathbf{n}\|^2 = 1$ , whereas mixed states are inside it.

One possible physical realization of a qubit system is the polarization of light, where the horizontal and vertical polarization are defined as basis states  $|0\rangle := |H\rangle$  and  $|1\rangle := |V\rangle$ . The second natural basis for linear polarization is the one of plus and minus polarization

$$\begin{aligned} |P\rangle &= \frac{1}{\sqrt{2}}(|H\rangle + |V\rangle) \\ |M\rangle &= \frac{1}{\sqrt{2}}(|H\rangle - |V\rangle). \end{aligned} \tag{1.17}$$

Circular (left and right handed) polarized light, characterized by a phase difference of  $\frac{\pi}{2}$ , form the third natural basis.

$$\begin{aligned} |R\rangle &= \frac{1}{\sqrt{2}}(|H\rangle + i|V\rangle) \\ |L\rangle &= \frac{1}{\sqrt{2}}(|H\rangle - i|V\rangle). \end{aligned} \tag{1.18}$$

As each basis provides the eigenstates of one of the Pauli operators, they are representing the corresponding axis on the Bloch sphere. The eigen equations read

$$\begin{aligned} \hat{\sigma}_x |P/M\rangle &= \pm |P/M\rangle \\ \hat{\sigma}_y |R/L\rangle &= \pm |R/L\rangle \\ \hat{\sigma}_z |H/V\rangle &= \pm |H/V\rangle. \end{aligned} \tag{1.19}$$

### 1.1.2 Composite systems

A composition of quantum systems can result in two different kinds of states. Firstly, for a *separable state* the density matrix of a composed system is given by a complex combination of product states  $\hat{\rho}_S = \sum_i P_i \hat{\rho}_i^A \otimes \hat{\rho}_i^B \otimes \hat{\rho}_i^C \otimes \dots$ , which simplifies for pure *product states* ( $P_i = 1$ ) to  $\hat{\rho}_{ABC\dots} = \hat{\rho}_A \otimes \hat{\rho}_B \otimes \hat{\rho}_C \otimes \dots$  as the state vector of the pure composite system is equivalent to the tensor product of the component physical systems  $|\Psi\rangle_{ABC\dots}^{prod} = |\psi\rangle_A \otimes |\psi\rangle_B \otimes |\psi\rangle_C \otimes \dots$ . Secondly, *entangled states* cannot – in comparison to product or separable states – be described by tensor products ( $|\Psi\rangle_{ABC\dots}^{ent} \neq |\psi\rangle_A \otimes |\psi\rangle_B \otimes |\psi\rangle_C \otimes \dots$ ). These states are not only composed states, but also share correlations. This phenomenon is purely quantum and gave rise to a lot of discussion. The *partial trace*  $\hat{\rho}_A$  of the density matrix of a composite system living in  $\mathcal{H}_C = \mathcal{H}_A \otimes \mathcal{H}_B$  describes the state of the subsystem  $A$

$$\hat{\rho}_A = tr_B(\hat{\rho}_C). \quad (1.20)$$

It is interesting to see, that for a composite entangled state, the result of a partial trace is always a mixed state in the subsystems.

**Two qubits** A composite system consisting of two qubits has four computational basis states. Sticking to the basis of polarized light  $\{|H\rangle, |V\rangle\}$  they are denoted as  $|HH\rangle, |HV\rangle, |VV\rangle, |VH\rangle$ . Therefore, a general pure two-qubit state can be written as

$$|\psi\rangle = a|HH\rangle + \beta|HV\rangle + \gamma|VH\rangle + \delta|VV\rangle \quad (1.21)$$

with the normalization condition  $|a|^2 + |\beta|^2 + |\gamma|^2 + |\delta|^2 = 1$ . Dependent on the coefficients this state can be either written with a tensor product or not and therefore be a product state or an entangled state, respectively. [10, 13]

One important entangled state is for example one of the four *Bell states*

$$|\psi\rangle = \frac{1}{\sqrt{2}}(|HH\rangle + |VV\rangle), \quad (1.22)$$

where the two systems cannot be regarded separately and the outcomes of a measurement performed on one single system will be correlated with the other one in more than one basis.

Obviously, a basis for linear operators in this 4-dimensional Hilbertspace is given by the tensor product combinations of the Pauli matrices  $\hat{\sigma}_i \otimes \hat{\sigma}_j$ . As for single qubit states there is also a way to express the density matrix of two qubits in terms of the expectation values of the measurement in all basis directions:

$$\hat{\rho} = \frac{\mathbb{1} + \sum_{i,j} E_{ij} \hat{\sigma}_i \otimes \hat{\sigma}_j}{4}, \quad i, j = 0, 1, 2, 3, \quad (1.23)$$

where  $E_{ij}$  are the expectation values of a global  $\hat{\sigma}_i \otimes \hat{\sigma}_j$  measurement.

**Entanglement measures** There are different ways to define the degree of entanglement, which will be important later in this work. One of them is the so called *negativity of a quantum state*, directly connected to the *PPT criterion*. First of all, the partial transpose of any quantum state  $\hat{\rho} \in \mathcal{H}_A \otimes \mathcal{H}_B$

$$\hat{\rho} = \sum_{ij} \sum_{kl} \rho_{ij,kl} |i\rangle\langle j| |k\rangle\langle l| \quad (1.24)$$

is defined via

$$\hat{\rho}^{\text{T}A} = \sum_{ij} \sum_{kl} \rho_{ji,kl} |i\rangle\langle j| |k\rangle\langle l|, \quad (1.25)$$

where the matrix elements in the space of  $\mathcal{H}_A$  have been transposed. For separable states  $\hat{\rho} \in \mathcal{H}_A \otimes \mathcal{H}_B$ , which can be always written as a complex combination of product states

$$\hat{\rho}_S = \sum_i P_i \hat{\rho}_i^A \otimes \hat{\rho}_i^B, \quad (1.26)$$

therefore holds that

$$\hat{\rho}_S^{\text{T}A} = \sum_i P_i (\hat{\rho}_i^A)^{\text{T}} \otimes \hat{\rho}_i^B = \sum_i P_i \tilde{\rho}_i^A \otimes \hat{\rho}_i^B \geq 0. \quad (1.27)$$

Because  $\rho_i^A$  is a density matrix its partial transpose has only non-negative eigenvalues resulting in a positive partial transpose (PPT) of the composite state. Hence PPT criterion implies, that when  $\hat{\rho}_S^{\text{T}A}$  has at least one negative eigenvalue,  $\hat{\rho}$  is guaranteed to be entangled. [14–17]

From this, the negativity  $\mathcal{N}(\hat{\rho})$  is derived, which measures how much  $\hat{\rho}^{\text{T}A}$  fails to be PPT. The negativity is defined as the sum over the negative eigenvalues  $\lambda_i$  of the partial transposed density operator  $\hat{\rho}^{\text{T}A}$

$$\mathcal{N}(\hat{\rho}) = \sum_{\lambda_i < 0} \lambda_i = \sum_i \frac{|\lambda_i| - \lambda_i}{2}. \quad (1.28)$$

Therefore, a separable state, whose eigenvalues are only non-negative, has negativity  $\mathcal{N}(\hat{\rho}_S) = 0$ , while the negativity of an entangled states is  $\mathcal{N}(\hat{\rho}_E) > 0$ . [14–17]

## 1.2 Quantum measurement

In order to obtain information about the microscopic physical quantities, measurements have to be performed on the quantum states. Quantum measurements are since the very beginning under investigation and controversially discussed in the different interpretations of the theory. This section gives a brief summary about how to perform quantum measurements and how they affect the state.

### 1.2.1 Projective measurement

When a quantum measurement is performed the possible outcomes of this measurements are given by the eigenvalues of the measured observable. This restriction of the possible measurement outcomes results in a finite discrete set of results for measurements in a finite dimensional Hilbert space. The system state  $|\psi\rangle$  can be represented by a linear combination of eigenstates  $|a_i\rangle$  of the observable  $\hat{A}$

$$|\psi\rangle = \sum_i c_i |a_i\rangle = \sum_i |a_i\rangle \langle a_i | \psi \rangle. \quad (1.29)$$

The measurement of observable  $\hat{A}$  also can be seen as a measurement in an orthonormal basis with a real value  $a_i$  associated to each basis state  $|a_i\rangle$ , such that the observable is described by the set of projectors  $\{|a_i\rangle\langle a_i| := \hat{\Pi}_i\}$

$$\hat{A} = \sum_i a_i |a_i\rangle\langle a_i|. \quad (1.30)$$

That is why this ideal form of quantum measurement is also denoted as *projective measurement* or *strong measurement* [18].

In a measurement of  $\hat{A}$  on a state  $|\psi\rangle$  (1.29), which is not an eigenstate of  $\hat{A}$ , the outcome can only be predicted probabilistically. The probability  $P_j$  for a result  $a_j$  associated with the state  $|a_j\rangle$  is given by

$$P_j = \langle \psi | \hat{\Pi}_j | \psi \rangle = |\langle a_j | \psi \rangle|^2 = |c_j|^2. \quad (1.31)$$

and the expectation value of the measurement is given by [9]

$$\langle \hat{A} \rangle_\psi = \sum_j a_j P_j = \langle \psi | \hat{A} | \psi \rangle. \quad (1.32)$$

After the measurement with outcome  $a_j$  the system is in state

$$|\psi'\rangle = \frac{\hat{\Pi}_j |\psi\rangle}{\sqrt{\langle \psi | \hat{\Pi}_j | \psi \rangle}}, \quad (1.33)$$

which can be regarded as a collapse of the system into the corresponding eigenstate. Consequently, a repetition of the same measurement results again in the same state and outcome. [8–10]

## 1.2.2 Indirect measurement

To actually perform a measurement the system is brought in contact with a measurement apparatus, which is read off after the measurement. It is von Neumann's model [19] which combines this physical measurement with projective measurements and provides a basis for studies of quantum measurements and its generalizations [18].

The main idea of the model is that due to the effect of interaction on the state of the apparatus, the result of the measurement can be read off from the affected apparatus degree of freedom, also called pointer variable. For its implementation, the measurement apparatus is described by the canonically conjugate variables  $\hat{p}$  and  $\hat{q}$  with  $[\hat{q}, \hat{p}] = i\hbar$ , where  $\hat{q}$  is referred to as the pointer variable in the following.

In a direct extension of von Neumann's scheme [18], for a measurement of observable  $\hat{A}$  the quantum system  $S$  and the measurement apparatus is coupled via the interaction of the Hamiltonian

$$\hat{H} = g(t)\hat{A} \otimes \hat{p} \quad (1.34)$$

with the instantaneous coupling rate  $g(t)$  which differs from zero in the time interval  $(t_i, t_f)$ . The initially ( $t \leq t_i$ ) uncorrelated system- and apparatus state ( $|\Psi_i\rangle = |\psi_S\rangle \otimes |\phi_M\rangle$ ) then becomes correlated for times  $t \geq t_f$  by the unitary transformation

$$\hat{U} = \exp\left(-\frac{i}{\hbar}\gamma\hat{A} \otimes \hat{p}\right), \quad (1.35)$$

where  $\gamma$  is the coupling strength

$$\gamma = \int_{t_i}^{t_f} g(t)dt \quad (1.36)$$

resulting in the final state  $|\Psi_f\rangle = \hat{U}(|\psi_S\rangle \otimes |\phi_M\rangle)$ .

Assuming  $\hat{A}$  has discrete and non-degenerate eigenvalues (1.30), it can be shown that a measurement of the pointer variable  $\hat{q}$  at  $t \geq t_f$  provides information about the system

$$\begin{aligned} |\Psi_f\rangle &= e^{-\frac{i}{\hbar}\gamma\hat{A} \otimes \hat{p}} \sum_i c_i |a_i\rangle \otimes |\phi_M\rangle \\ &= \sum_i c_i |a_i\rangle \otimes e^{-\frac{i}{\hbar}\gamma a_i \hat{p}} |\phi_M\rangle \\ &= \sum_i c_i |a_i\rangle \otimes |\phi_M^{\gamma a_i}\rangle, \end{aligned} \quad (1.37)$$

as the pointer states  $|\phi_M^{\gamma a_i}\rangle$  are rotated or shifted by the amount  $\gamma a_i$  after the measurement with respect to the initial ones. This can be seen for a continuous

pointer state by introducing the identity operator in the p- and q-basis and using that  $\langle p|q\rangle = \frac{1}{\sqrt{2\pi\hbar}}e^{-\frac{i}{\hbar}pq}$  [8, 20].

$$\begin{aligned} |\Psi_f\rangle &= \sum_i c_i |a_i\rangle \int_{q'} \int_p dq' dp e^{-\frac{i}{\hbar}\gamma a_i p} |p\rangle \langle p|q'\rangle \langle q'|\phi_M\rangle \\ &= \frac{1}{\sqrt{2\pi\hbar}} \sum_i c_i |a_i\rangle \int_{q'} \int_p dq' dp e^{-\frac{i}{\hbar}p(\gamma a_i + q')} |p\rangle \phi_M(q') \end{aligned} \quad (1.38)$$

A measurement of the pointer variable q then results in

$$\begin{aligned} \langle q|\Psi_f\rangle &= \frac{1}{\sqrt{2\pi\hbar}} \sum_i c_i |a_i\rangle \int_{q'} \int_p dq' dp e^{-\frac{i}{\hbar}p(\gamma a_i + q')} \langle q|p\rangle \phi_M(q') \\ &= \sum_i c_i |a_i\rangle \int_{q'} dq' \underbrace{\int_p dp \frac{1}{2\pi\hbar} e^{-\frac{i}{\hbar}p(\gamma a_i + q' - q)}}_{\delta(q' - (q - \gamma a_i))} \phi_M(q') \\ &= \sum_i c_i |a_i\rangle \underbrace{\phi_M(q - \gamma a_i)}_{|\phi_M^{\gamma a_i}\rangle} \end{aligned} \quad (1.39)$$

**Strong measurement** The system and pointer states are maximally correlated when the pointer states are non-overlapping, i.e. when the  $|\phi_M^{\gamma a_i}\rangle$  are pairwise orthogonal [13]. Performing a projective measurement on the pointer state according to the projector  $\hat{\Pi}_{\gamma a_i} = \mathbb{1} \otimes |\phi_M^{\gamma a_i}\rangle \langle \phi_M^{\gamma a_i}|$  results in a pointer state shifted by  $\gamma a_i$  with probability  $P_{\gamma a_i}^\Phi$

$$P_{\gamma a_i}^\Phi = \langle \psi_f | \hat{\Pi}_{\gamma a_i} | \psi_f \rangle = |c_i|^2. \quad (1.40)$$

This is the same as the probability of measuring  $a_i$  in a projective measurement directly on the system and explains why this choice of interaction Hamiltonian yields to the ideal form of an indirect measurement, equivalent to a projective measurement [9, 13].

Non-overlapping pointer states are a necessary requirement for this projective measurement. It is realized when the coupling is sufficiently strong [18] which is the case when the uncertainty  $\Delta q = \sqrt{\langle q^2 \rangle - \langle q \rangle^2}$  is small compared to the measurement strength

$$\Delta q \ll |\gamma| \delta a, \quad (1.41)$$

where  $\delta a$  is the minimal distance between the different  $a_i$ 's. For a single measurement the pointer shift  $\delta q = \gamma a_m$  is proportional to the specific result  $a_m$  of the measurement of  $\hat{A}$ , and hence for multiple measurements the expectation value of  $\hat{A}$  can be determined with high precision. After this type of measurement and maximal gain of information the initial system state is destroyed and found now in the corresponding eigenstate corresponding to Eq. (1.33).

**Weak measurement** In case the final pointer states  $|\phi_M^{\gamma a_i}\rangle$  are very similar, such that the final state  $|\Psi_f\rangle$  is almost separable, a single measurement provides very little information and is called *weak measurement*. In weak measurements the

## 1 Standard quantum mechanics and quantum measurement

---

uncertainty of the pointer variable has to be large compared to the measurement strength [18]:

$$\Delta q \gg |\gamma| \delta a, \quad (1.42)$$

where  $\delta a$  is now the maximum distance between between two consecutive  $a_j$ .

It is still possible to measure the average value  $\langle \hat{A} \rangle = \langle \psi_S | \hat{A} | \psi_S \rangle$ . From Eq. (1.39)

$$\gamma \langle \hat{A} \rangle = \langle \hat{q}_f \rangle - \langle \hat{q}_i \rangle \quad (1.43)$$

holds, where  $\langle \hat{q}_i \rangle$  and  $\langle \hat{q}_f \rangle$  are the expectation values of  $q$  at  $t = 0$  and  $t \geq t_f$  respectively.

Therefore, to obtain information about the system in form of  $\langle \hat{A} \rangle$ , measurements on each member of a sufficiently large ensemble of systems prepared in the same state have to be performed and then averaged over. Obviously the precision of the measurement increases with increasing ensemble size and the error of  $\langle \hat{A} \rangle$  can be made arbitrary small [18]. The way of extracting  $\langle \hat{A} \rangle$  differs conceptually from the one of a projective measurement (1.32), where the expectation value is obtained by the different probabilities for the different eigenvalues, whereas in a weak measurement it is obtained directly from the pointer shift in equation (1.43) without measuring each  $P_i$  individually.

## 1.3 Pre- and postselected systems

### 1.3.1 Two-state vector formalism

Until now the measurement together with the system state were only considered in one direction of time. Even though the dynamical laws of SQM are time symmetric as its classical counterparts and the Hamiltonian defines the motion of the system for all future and past times, there is a time asymmetry in SQM, which arises from the standard measurement approach. The collapse of the system into one of the observable's eigenstates makes it impossible to make any general statement about the state of the system immediately before the measurement; to evolve back to the system state prior to the measurement [21].

In the two-state vector formalism additionally to the standard approach, where the behavior of a system is studied assuming the knowledge of the state at some initial time  $t_1$ , the knowledge about the final state at some time  $t_2$  is added, such that a system with fixed boundary conditions in the past and future given by two complete measurements is regarded [18, 21]. In the intermediate time interval at  $t \in [t_1, t_2]$  the system is completely symmetric under time reversal. The new description of a quantum system at time  $t$  is the two-state vector

$$\langle \Phi | | \Psi \rangle, \quad (1.44)$$

which consists of a quantum state  $|\Psi\rangle$  defined by the results of measurements performed on the system in the past at some time  $t_1$  and of a backward evolving quantum state  $\langle \Phi|$  defined by the results of measurements performed on this system at some time  $t_2$  (see Fig. 1.2) [22].

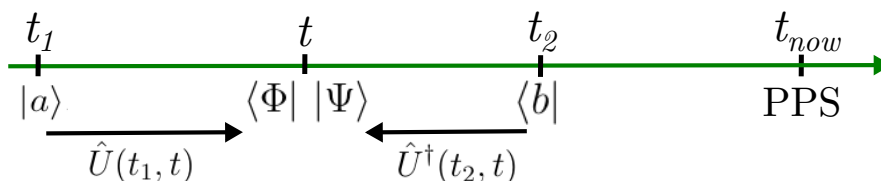


**Figure 1.2:** Definition of a pre- and postselected system described by a two-state vector [22].

Note that this definition of a quantum system yields, as the standard approach, maximal information about how this system can affect other systems. The only difference is the achieved symmetry. Whereas in the standard approach only the results of the measurements in the past are relevant for the state of the system, in the two-state vector formalism there is no preference to the results of measurements in the past relative to the results of measurements in the future [22].

A system described by a two-state vector is called *pre- and postselected system* (PPS). In order to have *now* at some time  $t_{now}$  a PPS, hence a system which is a

two-state vector at some previous time  $t$  there should be a complete measurement in the past of time  $t$  and a complete measurement after the time  $t$  [22] (see Fig. 1.2).

When the first measurement at some time  $t_1 < t$  of an observable  $\hat{A}$  gives an outcome  $a$  corresponding to the eigenstate  $|a\rangle$  of  $\hat{A}$ , then the system will evolve between  $t_1$  and  $t$  according to the unitary evolution

$$\hat{U}(t_1, t) = e^{-i \int_{t_1}^t \hat{H} dt'}, \quad (1.45)$$

where  $\hat{H}$  is the free Hamiltonian of the system, such that

$$|\Psi\rangle = \hat{U}(t_1, t)|a\rangle. \quad (1.46)$$

The second measurement at some time  $t_2 > t$  of observable  $\hat{B}$  results in  $b$  according to the eigenstate  $|b\rangle$  of  $\hat{B}$ , such that the backwards evolution results in

$$\langle\Phi| = \langle b|\hat{U}^\dagger(t_2, t). \quad (1.47)$$

The two-state vector  $\langle\Phi| |\Psi\rangle$  is the complete description of the system at time  $t$  starting from the time  $t_2$  [22].

### 1.3.2 Measurements on pre- and postselected systems

In order to apply the principle of indirect measurements from Section 1.2.2 to pre- and postselected systems, again an ensemble of systems and pointers in the initial state  $|\psi_S\rangle \otimes |\phi_M\rangle$  is considered, with the difference that now, instead of only reading off the pointer variables after the measurement, only pointer states belonging to a specific post-selection of the system states are regarded.

More precisely (see Fig. 1.3), each initial pair is prepared (pre-selected) such that the system and pointer state is a product state and they are then coupled via the interaction Hamiltonian from equation Eq. (1.34) in some time interval  $(t_i, t_f)$ . After having formed an ensemble of PPS by performing a strong measurement of observable  $\hat{B}$  on each system state at some time  $t_s \geq t_f$  and selecting only the system states which are in the eigenstate  $|\Phi\rangle$  of  $\hat{B}$  for further consideration, the PPS measurement is completed by measuring the pointer observable  $\hat{q}$  at  $t_M > t_f$ . [18]

With a statistical analysis of the results the average pointer value  $\langle\hat{q}_{PPS}\rangle$  and therefore also the measurement results of  $\langle\hat{A}\rangle$  on the PPS ensemble are gained. Note, that it is not relevant whether the pointer measurement is performed before or after the post-selection of the system states. It is only important that for the statistical evaluation only pointers corresponding to the PPS ensemble are included. [18]

It is interesting to notice, that the results of a measurement of  $\hat{A}$  on a post-selected subensemble depend on the chosen subensemble and differ from the results of this measurement without post-selection. Therefore, the measurement results are dependent on the initial and final state of the system.

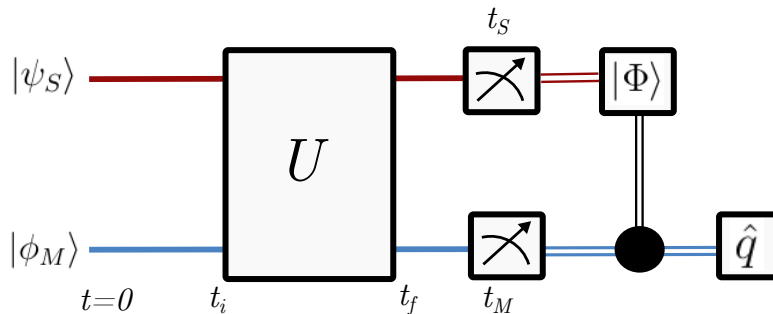


**Figure 1.3:** Schematic diagram of a model for pre- and postselected quantum measurement. Double lines carry classical information [18].

## 1.4 Weak value formalism

Since weak values as outcome of weak measurements on pre- and postselected systems were firstly introduced by Aharonov, Albert and Vaidman in 1988 [23], there was a lot of discussion about their meaning and interpretation [24–27]. Nevertheless, weak values have useful applications, such as for example in quantum foundations [28, 29] or Bohmian mechanics [4, 7, 30–33], and research on their meaning in various scenarios has made great progress [5, 21, 34–37]. Their definition and properties will be discussed in the following.

### 1.4.1 Definition of the weak value

The already mentioned measurement of  $\hat{A}$  on an ensemble of systems preselected in a state  $|\psi_1\rangle$  and postselected in a state  $|\psi_2\rangle$  results in an outcome called the weak value of  $\hat{A}$  [23]

$$A_w = \frac{\langle \psi_2 | \hat{A} | \psi_1 \rangle}{\langle \psi_2 | \psi_1 \rangle}. \quad (1.48)$$

This value arises naturally with a weak indirect measurement (see section 1.2.2) [18, 21, 23, 35, 38]. After the interaction (1.34) of system and apparatus, initially prepared in  $|\psi_1\rangle \otimes |\phi_M\rangle$ , has taken place, each system-pointer pair of the ensemble is in the state

$$|\Psi_f\rangle = e^{-\frac{i}{\hbar}\gamma\hat{A}\otimes\hat{p}}|\psi_1\rangle \otimes |\phi_M\rangle, \quad (1.49)$$

where the exponential can be series expanded as

$$e^{-\frac{i}{\hbar}\gamma\hat{A}\otimes\hat{p}} = \sum_n \frac{(-i)^n}{n!\hbar^n} \gamma^n \hat{A}^n \otimes \hat{p}^n, \quad (1.50)$$

such that the postselection of the system states on  $|\psi_2\rangle$  results in the final pointer state

$$\begin{aligned}
 |\phi_M^F\rangle &= N\langle\psi_2|\Psi_f\rangle = N\sum_n \frac{(-i)^n}{n!\hbar^n} \gamma^n \langle\psi_2|\hat{A}^n|\psi_1\rangle \hat{p}^n |\phi_M\rangle \\
 &= N\langle\psi_2|\psi_1\rangle \sum_n \frac{(-i)^n}{n!\hbar^n} \gamma^n \frac{\langle\psi_2|\hat{A}^n|\psi_1\rangle}{\langle\psi_2|\psi_1\rangle} \hat{p}^n |\phi_M\rangle \\
 &\stackrel{\gamma \ll 1}{\approx} N\langle\psi_2|\psi_1\rangle \left(1 - \gamma \frac{i\langle\psi_2|\hat{A}|\psi_1\rangle}{\hbar\langle\psi_2|\psi_1\rangle} \hat{p}\right) |\phi_M\rangle \\
 &\approx \underbrace{N\langle\psi_2|\psi_1\rangle}_{N'} e^{-\frac{i}{\hbar}\gamma A_w \hat{p}} |\phi_M\rangle
 \end{aligned} \tag{1.51}$$

with the normalization constants  $N$  and  $N'$  for which  $|N'|^2 = 1$  holds. The approximation becomes arbitrarily accurate since the interaction strength  $\gamma$  can be chosen very small. Comparing this result with the final pointer state in standard indirect measurements (1.37) it becomes clear that  $A_w$  plays the role of the equivalent of an expectation value for pre- and postselected systems in the weak regime. The fact that  $|\psi_1\rangle$  and  $|\psi_2\rangle$  can be nearly orthogonal can lead to the need for a very large ensemble of measured systems [38].

The following measurement of the conjugate pointer variable  $\hat{q}$  yields

$$\begin{aligned}
 \langle q \rangle_f &= \langle \Phi_M^F | \hat{q} | \Phi_M^F \rangle \\
 &\approx \langle \phi_M | \left(1 + \frac{i}{\hbar} \gamma A_w^* \hat{p}\right) \hat{q} \left(1 - \frac{i}{\hbar} \gamma A_w \hat{p}\right) | \phi_M \rangle \\
 &= \langle \hat{q} \rangle + \frac{i}{\hbar} \gamma (A_w^* \langle \hat{p} \hat{q} \rangle - A_w \langle \hat{q} \hat{p} \rangle) \\
 &= \langle \hat{q} \rangle + \frac{i}{\hbar} \gamma (\text{Re}[A_w] \langle [\hat{p}, \hat{q}] \rangle - i \text{Im}[A_w] \langle \{\hat{p}, \hat{q}\} \rangle) \\
 &= \left( \langle \hat{q} \rangle + \gamma \text{Re}[A_w] + \frac{\gamma}{\hbar} \text{Im}[A_w] \langle \{\hat{p}, \hat{q}\} \rangle \right) \\
 &= \left( \langle \hat{q} \rangle + \gamma \text{Re}[A_w] + \frac{2\gamma}{\hbar} \text{Im}[A_w] c_{qp} \right),
 \end{aligned} \tag{1.52}$$

where  $\{\hat{A}, \hat{B}\} = \hat{A}\hat{B} + \hat{B}\hat{A}$  is the anticommutator.

$$c_{qp} = \frac{\langle \{\hat{p}, \hat{q}\} \rangle}{2} \tag{1.53}$$

is introduced as the “quantum analog” of the classical covariance. For standard weak measurements usually pointers with zero covariance are assumed [18, 39] such that the pointer expectation value can be read off from a pointer shift which is proportional to the real part of the weak value of  $\hat{A}$

$$\langle q \rangle_f = \langle q \rangle_i + \gamma \text{Re}[A_w]. \tag{1.54}$$

Note that in a weak measurement the magnitude of the average pointer deflection  $\langle q \rangle_f - \langle q \rangle_i$  is much less than the statistical dispersion of the measurement result

$\Delta q$ , such that it becomes necessary to average over the measurement results obtained for many identical systems prepared and postselected in the same states [18].

As we have seen, the weak value depends on the future of the system after the measurement and therefore can only be obtained by weak measurement on a PPS. Accordingly, the system state is only slightly changed, which is why the weak value provides information about the undisturbed system.

### 1.4.2 Unusual properties

Nevertheless, the weak value is not the same as an expectation value. It has drastically different properties which will be described in the following.

**Definite values for several non-commuting variables** For any PPS ensemble either pre- or postselected in an eigenstate of an observable  $\hat{A}$ , such that  $|\psi_1\rangle = |a_j\rangle$  or  $|\psi_2\rangle = |a_j\rangle$ , the weak value of  $\hat{A}$  is equal to the corresponding eigenvalue  $a_j$ . In contrast to standard quantum measurement, where only the measurement results of two commuting observables can both be ascertained, a consequence of this property is the possibility to also obtain definite values in a PPS measurement of at least two non-commuting observables with no common eigenstates, when  $|\psi_1\rangle \neq |\psi_2\rangle$  [18, 40]. Therefore it is for example possible to ascertain the result of a simultaneous weak PPS measurement of  $\hat{\sigma}_x$  and  $\hat{\sigma}_y$ .

**Values not limited to the range of eigenvalues** It is easy to see that the formula for the weak value (1.48) with equal pre- and postselection, meaning  $|\psi_2\rangle = |\psi_1\rangle$  yields the expectation value  $\langle \hat{A} \rangle$ . For  $\langle \psi_2 | \psi_1 \rangle$  being very small, the weak value of  $\hat{A}$  can get very large, because  $A_w$  diverges for  $\langle \psi_2 | \psi_1 \rangle$  tending to zero, with the consequence that the weak value is not limited by the range of eigenvalues of an observable. This effect can be explained by interference of the differently displaced pointer components. For standard indirect measurement (1.38), no interference is possible as the pointer states are – even if they overlap due to the weakness of the measurement interaction – correlated to pairwise orthogonal eigenstates of the observable. For a weak measurement on a pre- and postselected system the components overlap significantly and the postselection creates interference which strongly affects the measurement results. [18]

**Complex values** Moreover, in general the weak value is a complex quantity. As it was already shown above, the imaginary part of  $A_w$  does not affect the probability distribution of the pointer position  $\hat{q}$  for standard weak measurements, but it does affect the distribution of the conjugate variable  $\hat{p}$ . The shift of the momentum of the pointer is proportional to the imaginary part of the weak value of  $\hat{A}$  [18]

$$\langle \hat{p} \rangle_f = \langle \hat{p} \rangle_i + 2\gamma(\Delta p)^2 \text{Im}[A_w], \quad (1.55)$$

## 1 Standard quantum mechanics and quantum measurement

---

where  $\Delta p$  is the statistical dispersion of the measurement results of the pointer momentum.

Due to these unusual properties, that a weak value can be far outside the range of the eigenvalues of the observable, negative or even complex, the probability distribution of the pointer values is in general non-classical and therefore the weak value cannot be understood as a usual mean value of a weak PPS measurement, as it is taken over a non-classical distribution [18].

# 2 Bohmian mechanics and the double slit experiment

## 2.1 Bohmian mechanics

Louis de Broglie's PhD thesis from 1924 addresses not only the famous wave-particle-duality of matter, but also a theory of new dynamics in which particle velocities are determined by guiding waves. Three years later, in 1927, he presented an even more complete form of his pilot-wave-theory at the fifth Solvay conference [41, pp. 116].

This theory was neglected and considered wrong for many years. In 1952, the theory was elaborated by David Bohm [1], but still largely ignored by the physics community. Since the 1990s with the publication of textbooks explaining quantum mechanical phenomena through pilot wave theory [42, 43], Bohmian mechanics, as Bohm's theory is often called, has been recognized as an alternative interpretation to SQM by most of the physics world [44]. The following chapter will discuss the ideas of Bohmian mechanics and summarize the formalism.

### 2.1.1 Criticism on standard quantum mechanics

“If the ontology is clear – if it is clear what the fundamental entities in nature are that the theory seeks to describe – there can't be any paradoxes.”

*D. Dürr and D. Lazarovici, 2020 [45]*

#### Ontology of quantum theories

As it was explained, SQM is a statistical description of the results of a measurement process. Compared to previous theories like Newtonian or classical statistical mechanics, where the predictions are also statistical, but both measurement and statistics are based on assumptions on what is happening in the system, the standard quantum theory can be formulated *only* in terms of the results of the measurement process. Therefore, SQM does not, like previous theories, deal with the ontology of individual actual systems but seems to have an epistemological and statistical component, as it is only described by the results of the measurement. That means that without the measurement results there is nothing left but pure mathematics without any physical interpretations. [42]

For many opponents of the standard quantum theory this lack of ontology invites doubt. Dürr and Lazarovici, for example, explain in their book “Under-

standing Quantum Mechanics” that the question *What is the theory about?* is a physical question, which has to be answered by the theory itself and should not be left open to interpretation. It is fundamental in order to understand what a theory tells about nature [45].

Arguing against SQM and for his alternative theory, David Bohm points out that the assumptions SQM is making and the resulting lack of precision are unnecessary. These assumptions contain, firstly, that the wave function and its probability interpretation are the most complete specification of the state of an individual system, and, secondly, that its collapse, the process of transfer of a single quantum from observed system to measuring apparatus is inherently unpredictable, uncontrollable and unanalyzable [1]. This leads to a self consistent formulation, with the uncertainty principle as an inherent and unavoidable limitation on the precision of all possible measurements. However, he argues that this consistency of the formulation is not sufficient to exclude other possible interpretations with additional parameters. Also there is no proof for the necessity of the assumptions, which remove the “possibility of even conceiving precisely what might determine the behavior of an individual system at quantum level” [1].

In order to restore precision and understand what is ‘really’ happening, Bohm adds the particle’s position to the wavefunction as the theory’s ontology. By the description of the particle’s movement, it is possible to explain what is happening in the real physical world without assuming a fundamental role for the human observer [42].

### The Measurement problem

Since the beginning of quantum mechanics the measurement of a quantum observable was a subject of discussion and paradoxes. The individual solution of the problem by each different interpretation of QM is very important for the judging of each theory.

Considering the measurement of a spatial observable with an non-degenerate spectrum of eigenvalues  $n$ , normalized eigenstates  $\psi_n(x)$  and an initial wave function of the observed system

$$\psi(x) = \sum_i c_n \psi_n(x). \quad (2.1)$$

which is coupled to a measurement apparatus with initial wave function  $\varphi_0(y)$  such that the combined wave function reads

$$\Psi_i(x, y) = \varphi_0(y) \sum_n c_n \psi_n(x). \quad (2.2)$$

After a suitable interaction the final state of system and apparatus is given by

$$\Psi_f(x, y) = \sum_n c_n \varphi_n(y) \psi_n(x). \quad (2.3)$$

This is an entangled state of the system and the non-overlapping pointer-states  $\varphi_n(y)$ , displaying the different ‘ $\psi_n$ ’. Hence, the pointer seems to indicate several states at the same time. This state doesn’t represent a pointer displaying one specific state by pointing into one definite direction, as it is actually experienced when measurements are performed [45]. This is the measurement problem.

**SQM’s solution** The first ideas solving the dilemma were proposed by Heisenberg in his uncertainty paper 1927 [46] and later elaborated by van Neumann in his book about the mathematical foundations of QM in 1932 [19]. They postulated the *collapse* of the wavefunction as a dynamical process independent of Schrödinger’s equation which reduces the superposition (2.3) to  $\varphi_m(y)\psi_m(x)$  with probability  $|c_m|^2$  [45, 47] as it was explained in the previous chapter 1.2.2.

Hence, in SQM there are two different dynamics: Firstly, the deterministic one given by Schrödinger’s equation, when the system is not measured, and, secondly, a probabilistic one which collapses the wave function to an eigenstate of a measured observable. [19]

This incompatibility of the dynamics and the resulting importance of the observer’s role of is often criticized. “When the ‘system’ in question is the whole world, where is the ‘measurer’ to be found? [...] What exactly qualifies some subsystems to play this role? [...] Is there ever then a moment when there is no jumping and the Schrödinger equation applies?” [48, p. 117]. The ambiguity, consisting in the lack of clear distinction between “macroscopic definiteness” and “microscopic indefiniteness” [44, p. 156], is leading to many different theories that treat the measurement problem differently compared to the standard interpretation of QM.

**BM’s solution** Prominent alternatives to SQM are for example the GRW theory [49], which replaces the Schrödinger evolution by a non-linear, stochastic equation that already contains the possibility of collapse, or the Many Worlds theory, which accepts the macroscopic superposition of the measurement device, but extends it to the experimenter and his or her whole universe [50].

Nevertheless, this thesis is about the Bohmian way of thinking and in this theory, as already mentioned above, the assumption that the wavefunction provides a complete description of the physical state of a system is denied. In order to turn an incomplete description into a complete one the motion of point particles is used to describe the occurrence of the particular measurement outcomes. The complete description of a system is therefore given by a pair  $(\psi, Q)$  of the wave function  $\psi$  and the position  $Q$  of the system’s particles. The wavefunction is responsible for the guidance of the particle’s motion. Thus, a macroscopic superposition of the measurement device is possible on the level of the wavefunction (2.3), and the *actual* configuration describes a pointer pointing into one definite direction [45].

### 2.1.2 Non-local hidden variables

These actual particle positions represent *hidden variables* compared to SQM. Subensembles are not anymore classified only by quantum mechanical observables but in terms of inner properties, which can later influence the directly observable behavior of the system [51]. This turns QM from a probabilistic to a deterministic theory. BM is one of the most popular hidden variable theories in a whole cosmos of theories explaining quantum phenomena using additional variables.

**No-hidden-variable proof and its refutation** This attribution as a hidden variable theory became the theory's undoing after its first formulation by de Broglie [52], when von Neumann formulated a proof which ruled out hidden variable theories for QM [19].

In his proof von Neumann's main assumption was, that any real linear combination of any two hermitian operators represents an observable, and that the same linear combination of expectation values is the expectation of the combination. This is, when  $\hat{O} = \hat{A} + \hat{B}$ , then  $\langle \hat{O} \rangle = \langle \hat{A} \rangle + \langle \hat{B} \rangle$ , which is true for SQM states, but von Neumann sets it also as an requirement for those hypothetical states, which are said to be *dispersion free* because they are further specified by hidden variables such that given values of these variables together with the state vector determine precisely the outcome of individual measurements [53]. For dispersion free states, which do not have statistical character, the expectation value of the observable must equal one of its eigenvalues and therefore the additivity of expectation values is not given anymore [53]. Von Neumann then concluded that there is no other description of the quantum mechanical process possible than the statistical one.

Even though already in 1935 Grete Hermann recognized the limited validity of his proof [54], von Neumann's *No Hidden Variable* proof was regarded as a complete repudiation of hidden variable interpretations by the physics community for many years. Contrary to her own opinion, that QM could be seen as causal and complete and there is no need for the assumption of hidden variables, Hermann, a young female mathematician, physicist and philosopher, was the first to show that von Neumann's proof was not consistent [55]. Unfortunately this knowledge had been ignored by the physics society until John S. Bell in 1966 – inspired by the counterexample to von Neumann's proof by Bohm in 1952 [1] – redid the argumentation unaware of Hermann's effort.

Bell explains – similar to Hermann – that there is no reason to demand the additivity of expectation values, which is a quite peculiar property of quantum mechanics, a priori from the hypothetical dispersion free state, “whose function is to reproduce the measurable peculiarities of quantum mechanics when averaged over” [53].

**Non-locality** In contrast to classical physics, which is ruled by the principle of locality, which means that no influence on a given physical system can travel

faster than light, in QM systems can be influenced by actions at a remote distance non-locally. After a long ongoing debate on the incompleteness of the wave function and the necessity of hidden variables [56, 57] to explain phenomena like entanglement, where the measurement of one part of the system is instantaneously correlated with the outcome of the measurement of the other part of the system independent of their distance, in 1964 Bell [58] provided a way to experimentally show, that no physical theory using local hidden variables can ever reproduce all predictions of QM [57, 59].

Forgotten, because considered wrong until Bell's rescue of non-local hidden variable theories, Bohm's model indeed explained the non-locality in QM by using a quantum potential, which is formed by the wave function, guides the particle's position and instantaneously reacts on changes of any element involved in the quantum mechanical process. Therefore, if entanglement is present, the position of a Bohmian particle can affect the motion of an arbitrarily distant particle, which is clearly a non-local effect [60]. The exact mathematical properties of the theory are explained in the following section.

### 2.1.3 Mathematical description of the Bohmian theory

Particles in motion are the main idea of BM. The motion of  $N$  particles is governed by a vector field on the  $3N$ -dimensional configuration space of the particles

$$\mathbb{R}^{3N} = \{q \mid q = (\mathbf{q}_1, \dots, \mathbf{q}_N), \mathbf{q}_k \in \mathbb{R}^3\}$$

A complete description of the system is provided by not only the wavefunction  $\psi(q, t) = \psi(\mathbf{q}_1, \dots, \mathbf{q}_N, t)$ , defined on the space of possible configurations  $q$  of the system, but also the actual configuration  $Q$ , defined by the actual positions  $Q_1, \dots, Q_N$  of its particles [45, 61].

#### Particles and the wave function

The complete Bohmian theory can be described by only two equations. On the one hand, there is *Schrödinger's equation* for the wave function's evolution:

$$i\hbar \frac{\partial}{\partial t} \psi(q, t) = \left[ -\frac{\hbar^2}{2m} \nabla^2 + V(q) \right] \psi(q, t) = \hat{H} \psi(q, t), \quad (2.4)$$

with the Hamiltonian  $\hat{H}$ , containing the masses of the particles and a potential energy term. Thus, the evolution of the wave function in BM does not differ from their evolution in SQM. Due to the wave function's statistical relevance for the system, measurement results are the same for all time in BM and SQM. [45, 62, 63]

On the other hand, the wavefunction defines the velocity vector field, which is the *guiding equation* for the evolution of the position of the particles:

$$v^\psi(q, t) = \frac{d}{dt} Q(t) = \frac{\hbar}{m} \operatorname{Im} \left[ \frac{\nabla \psi(q, t)}{\psi(q, t)} \right] \Big|_{q=Q(t)} \quad (2.5)$$

## 2 Bohmian mechanics and the double slit experiment

---

**The quantum potential** To motivate Eq. (2.5) we can write the complex wave function in its polar form

$$\psi(q, t) = R(q, t)e^{\frac{i}{\hbar}S(q, t)}, \quad (2.6)$$

insert it to Schrödinger's equation (2.4) and separate real and imaginary parts. Then, Schrödinger's equation reduces to the two following equations:

$$\frac{\partial S}{\partial t} + \frac{(\nabla S)^2}{2m} + V - \frac{\hbar^2}{2m} \frac{\nabla^2 R}{R} = 0 \text{ and} \quad (2.7a)$$

$$\frac{\partial R}{\partial t} - \frac{\hbar^2}{2m}(R\nabla^2 S + 2\nabla R\nabla S) = 0 \quad (2.7b)$$

In the classical limit ( $\hbar \rightarrow 0$ ) Eq. (2.7a) resembles the Hamilton-Jacobi equation. Considering an ensemble of particle trajectories which are solutions of the equations of motion, then if all of these trajectories are normal to any given surface of constant  $S$ , they are normal to all surfaces of constant  $S$  and  $\nabla S(q)/m$  will be equal to the velocity vector  $v(q)$  for any particle passing the point  $q$  [1]. This idea can be transformed to the guiding equation (2.5).

The particle may therefore be regarded as particle with momentum  $\mathbf{p} = \nabla S$ , subject not only to the classical potential  $V$ , but also to the *quantum potential*  $U$  [42]

$$U(q, t) = -\frac{\hbar^2}{2m} \frac{\nabla^2 R}{R}, \quad (2.8)$$

which goes to zero in the classical limit.

**The continuity equation** Another way to understand the guiding equation (2.5) is to rewrite Eq. (2.7b) in terms of the probability density  $\rho = |\psi(q, t)|^2 = R^2$  [62]

$$\frac{\partial \rho}{\partial t} + \nabla \frac{\rho \nabla S}{m} = 0. \quad (2.9)$$

By inserting the polar form of the wavefunction (2.6) into Madelung's [64] definition for the probability current or quantum flux  $j^\psi$

$$j^\psi(q, t) = \frac{\hbar}{2im}(\psi^* \nabla \psi - \psi \nabla \psi^*) \quad (2.10)$$

one finds out that equation (2.9) is nothing else but a *continuity equation*

$$\frac{\partial \rho}{\partial t} + \nabla j^\psi = 0. \quad (2.11)$$

Rewriting equation (2.10) as

$$j^\psi(q, t) = \frac{\hbar}{m} \text{Im} [\psi^* \nabla \psi] \quad (2.12)$$

and considering

$$\nabla j^\psi = \nabla \frac{j^\psi}{|\psi|^2} |\psi|^2 =: \nabla v^\psi |\psi|^2, \quad (2.13)$$

one obtains the vector field

$$v^\psi(q, t) = \frac{j^\psi(q, t)}{|\psi(q, t)|^2} = \frac{\hbar}{m} \operatorname{Im} \left[ \frac{\psi^*(q, t) \nabla \psi(q, t)}{|\psi(q, t)|^2} \right], \quad (2.14)$$

which can be reduced to the guiding equation.

### Statistical properties of BM

On its way to provide a realistic theory of QM Bohmian mechanics reveals itself as a deterministic theory. Once an initial wavefunction  $\psi_{t_0}$  is specified for a certain initial time  $t_0$ , the wavefunction  $\psi_t$  can be calculated for every time  $t$  by Schrödinger's equation. The guiding equation (2.5) then defines the particle position for all times, such that, once an initial configuration  $Q(t_0)$  is specified, it determines the entire history of the system. As shown by the continuity equation (2.11) it is consistent to interpret  $|\psi|^2 = \rho$  as a probability density in a statistical ensemble of well-defined trajectories, each following the causal laws above. Hence, an initial configuration  $Q(t_0)$  chosen at random with probability density  $|\psi_{t_0}|^2$  will have later at some time  $t$  a configuration  $Q(t)$  corresponding to the probability density  $|\psi_t|^2$ . This compliance of the configuration with the Born rule is known as *equivariance*. [63]

The position of Bohmian particles is therefore theoretically determined for all times by their initial position and wavefunction. Practically it is not to disregard that the positions of Bohmian particles cannot be controlled with arbitrary precision, they are hidden variables. Therefore, one has to focus on typical initial values when using the theory to explain phenomena [45, 65]. Thus, a measure of typicality is needed to define which configurations are typical, which has to be preserved under the dynamics of the system. In BM this measure is naturally given by the probability density  $\rho = |\psi(t)|^2$  for all times, which means that Born's rule here is not an axiom but a theorem [62], also called *quantum equilibrium hypothesis*. An important consequence of this is the empirical equivalence between BM and SQM, which implies that for every conceivable experiment BM makes the same predictions as SQM [32].

In summary, the Bohmian theory can be explained in only three steps: Firstly the  $\psi$ -field satisfies Schrödinger's equation, secondly the guiding equation (2.5) holds and thirdly there is a statistical ensemble of particle positions with a probability density  $\rho = |\psi(q, t)|^2$  [2]. Therefore, the wavefunction carries out two important tasks in the Bohmian theory. On the one hand it is responsible for the definition of the quantum potential and on the other it is, as in SQM, responsible for the probability density as Born suggested. The main difference to Born's idea of a probability density to *find* a particle at a certain position in a suitable measurement is that in the Bohmian interpretation it is the probability density for a particle to *be* at a certain position [45]. Hence, even though measurement results are the same in both theories, different interpretations lead to different perspectives on the observation. This becomes clear by a closer look at the double slit experiment in the following section.

### 2.2 The Double slit experiment

When Young presented his experimental proof of the “general law of the interference of light” in 1803 [66], he did not know that it would become one of the most influential experiments in physics, due to its tight connection to quantum mechanics. By sending coherent light through a plate with two parallel slits in it and later detecting an interference pattern on a screen (see Fig. 2.1), Young discovered the wavelike behavior of light. After Einstein’s explanation for the photoelectric effect via light quanta, the so called photons [67], and the verification of de Broglies idea [52] that also quantum particles create such interference patterns, with electrons by Davisson and Germer [68], it was clear that light like every other quantum particle can be both: particle and wave, also called *wave-particle duality*. So, the interference pattern is even preserved if only a single particle enters at a time, and then the impact points of many particles are accumulated. This completely contradicts classical intuition. [69, 70]

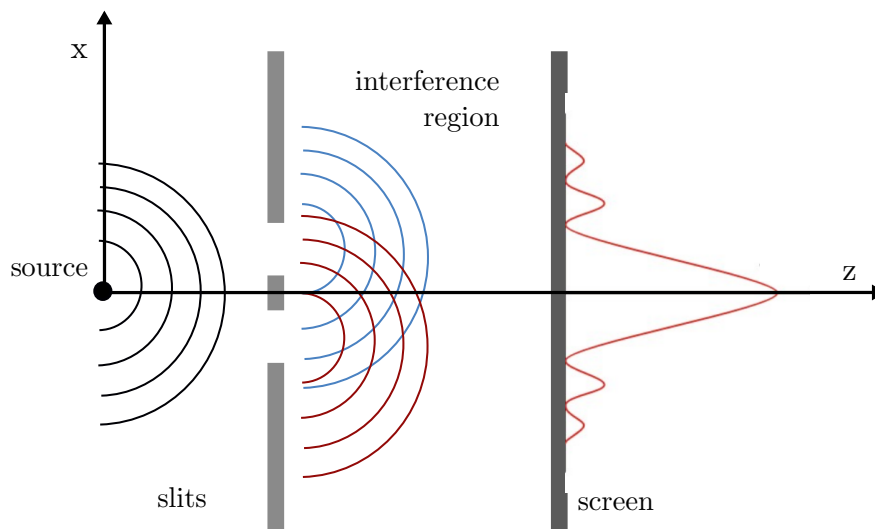


**Figure 2.1:** Illustration of a double slit experiment

Of course, the various interpretations of QM treat the wave-particle duality differently, but all agree that the double-slit experiment reflects the extraordinary nature of QM. In his *Lectures on Physics* Richard Feynman expresses powerfully the importance of this experiment for quantum mechanics:

“We choose to examine a phenomenon which is impossible, absolutely impossible, to explain in any classical way, and which has in it the heart of quantum mechanics. In reality, it contains the only mystery. We cannot make the mystery go away by ‘explaining’ how it works. We will just tell you how it works. In telling you how it works we will have told you about the basic peculiarities of all quantum mechanics.”

*Richard Feynman, 1963* [3]

### 2.2.1 Standard quantum mechanics explanation

In the usual interpretation of quantum mechanics the interference pattern arises, because the properties of the particle is described by a wave function, which gets modified by interference and diffraction when passing through the slit system, such that the characteristic intensity pattern is created. The probability to detect the particle between  $x$  and  $x + dx$  is  $|\psi(x)|^2 dx$ , such that, if the experiment is repeated many times with the same initial conditions, one eventually obtains the interference pattern, known from classical optics [1].

But there are several questions left open. The particle can not be identical with its associated wave, as the wave spreads out over a wide region, whereas when measuring the particle's position a certain value is obtained. On the other hand an interference pattern or the question, why particles can reach different detection regions when one slit is closed, cannot be explained without a wavelike nature of the particle. [1]

Thus, SQM takes advantage of the so called *principle of complementarity*, introduced by Niels Bohr in 1927 [71], where elements from both views – wave and particle – are equally valid and equally needed for an exhaustive description of the data, but their applicability is dependent on the experimental context [72]. Therefore, it is impossible to measure the full properties of the wave and particle at a particular moment.

Applied to the double slit, this means that while the electron goes through the slit system its position is said to be ambiguous, such that it is meaningless to ask through which slit an individual electron actually passed as long as the interference pattern is present. Here the wave mode can be used and describes the occurring of interference. On the other hand, there are conditions under which the particle model becomes defined more precisely corresponding to a decrease of wave behavior. When for example the position of the electron passing the slit system is measured, the interference pattern and therefore its wavelike property is completely destroyed. [1]

### 2.2.2 Bohmian mechanics explanation

In contrast to the standard way in the Bohmian picture wave and particle exist simultaneously. Thus, the causal and continuous Bohmian description is possible in terms of a single precisely definable conceptual model [1], where the physical particle goes through only one slit, whereas the wave passes through both and therefore interferes [62]. The same wavefunction as in the standard interpretation is here regarded as a mathematical representation of a real field, determining parts of the force acting on the particle via the quantum potential (2.8)

$$U(q, t) = -\frac{\hbar^2}{2m} \frac{\nabla^2 R}{R},$$

which is dependent on the amplitude of the wavefunction  $R(q, t)$ . The quantum potential guides the particle through the interference region which results in well

## 2 Bohmian mechanics and the double slit experiment

---

defined particle trajectories, defined as the integral curves along the vector field  $\mathbf{v}^\psi(\mathbf{q}, t)$  (2.14). The first calculation of this potential by Philippidis et al. [73] can be seen in Fig. 2.2.

### Interference and quantum potential

For a plane wave, before entering the slit the potential vanishes as the amplitude is constant, whereas in the interference region the particle experiences a quantum potential which changes rapidly with position, resulting in a quite complicated motion of the particle. Nonetheless, the probability that a particle will arrive in a certain region  $dx$  on the screen, is given by  $|\psi(x)|^2 dx$  as in the standard theory. It can be easily seen that, due to the quantum potential, the particle never reaches a point where the wave function vanishes. For an amplitude of the wavefunction going to zero the quantum potential goes to infinity. [1]

Another important property of the quantum potential is its non-locality. Properties of all participating elements, like masses, particle velocities or the geometry of the slits, are combined in an irreducible way in it. This suggests that space no longer plays the role of “a neutral back cloth” [73], but appears to be structured in a way that imposes constraints on all processes embedded within it, such that the position of a particle, guided by the quantum potential, defines e.g. the value of the involved wave functions. This puts Bohr’s claim that quantum phenomena and the experimental situation are inseparable in a new light: changing anything involved in the process changes instantaneously the whole quantum potential and possibly gives rise to the observation of completely different phenomena even at distant positions. [73]

Hence, closing one slit alters the  $\psi$ -field and thus the quantum potential is changed. That is why particles can now reach other regions than they could have reached before, when both slits were open. The slit can therefore affect the motion of the particles only indirectly, through its effect on the  $\psi$ -field. Contrary to SQM the fact, that the measurement of the particle’s position at the moment of its passage through the slit system destroys the interference pattern, is explained by the disturbance of the wave function by such an measurement apparatus, but not by the conceptual structure of the theory. [1]

### Interference and trajectories

Guided by and therefore accumulating in lower valued regions of the quantum potential, the particles travel from the slits to the screen. The calculated trajectories of various initial positions within each of the slits by Philippidis et al. [73] can be seen in figure 2.3. The connection of the trajectories and the quantum potential becomes visible by comparing Fig. 2.2 and Fig. 2.3. Dependent on their position particles experience a force given by the value of the quantum potential at their position. Particles entering a region of a trough, i.e. a region where the potential goes to minus infinity, are strongly accelerated into a region of a plateau, where the potential is weak again until they reach a trough again. That’s why most of

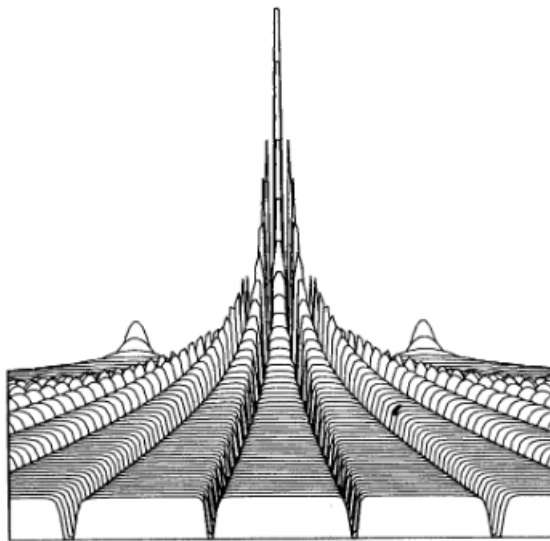


**Figure 2.2:** Quantum potential for two Gaussian slits. First theoretical calculation, by Philippidis et al. [73].

the trajectories run along the plateau regions resulting in bright fringes, whereas troughs coincide with dark fringes [73].

Another point of view, which is also important for the experimental realization, is to understand, that the distribution of the transverse momentum shows at every  $z$ -position in the interference region a different profile (see Fig. 2.4). Dependent on the quantum potential at the given  $z$ -position, the absolute value of the velocity in  $x$ -direction is either high, changing particle's motion in  $x$  direction in the region of an interference minimum for example, or low when the particle does not change its propagation direction.

Visible in Fig. 2.2, Fig. 2.3, and Fig. 2.4 both the potential, the trajectories and the Bohmian momentum show a common symmetry. It stems from the symmetry of the double-slit configuration, which can be seen in the total wavefunction

$$\psi(x, z, t) = \frac{1}{\sqrt{2}}(\psi_L(x, z, t) + \psi_R(x, z, t)), \quad (2.15)$$

where the wavefunction from the left slit can be obtained by the one from the right slit by reflection at the  $x = 0$ -plane:

$$\psi_R(x, z, t) = \psi_L(-x, z, t). \quad (2.16)$$

Thus, the  $z$ -component of the current vector (2.12)  $\mathbf{j} \propto \text{Im}[\psi \nabla \psi]$  is odd in  $x$  and so is also the velocity field (2.14)  $\mathbf{v} = \mathbf{j}/|\psi|^2$ , while the probability density is even. Therefore, the  $x$ -component of the velocity vanishes at the  $x = 0$ -axis. This implies, that Bohmian trajectories do not cross the  $x = 0$ -line [48]. Hence, according to the Bohmian theory a particle detected on the left side of the screen

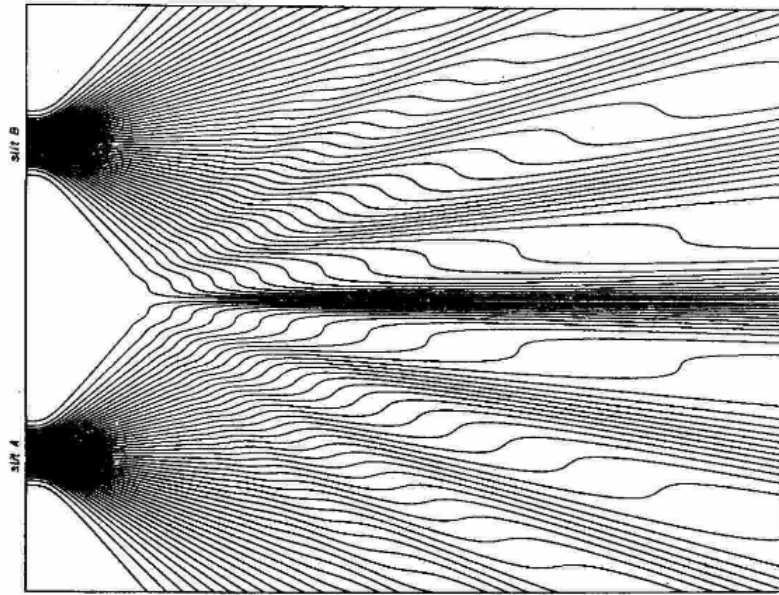


**Figure 2.3:** Particle trajectories in the interference region of a double slit apparatus. First theoretical calculation, by Philippidis et al. [73].

( $x < 0$ ) must have passed through the left slit and vice versa. In SQM this statement is completely meaningless. Due to the complementarity principle no assertions about the slit or position can be made, as long as no measurement is performed. [4]

### Surreal trajectories

Continuing this thought about the dependence of the traversed slit on the point of incidence of the photon on the screen, the Bohmian theory was strongly criticized by Englert, Scully, Süssmann and Walther (ESSW) in 1992, who claimed that “the reality attributed to Bohm trajectories is not physical, it is metaphysical” [4]. This paper led to an intense debate about the realism of Bohmian trajectories.

**Accusation of surrealism** In their Paper ESSW consider a double-slit experiment with additional which-way-detectors. These detectors are ideally chosen such, that they do not disturb the motion of the particle’s center of mass and do not induce macroscopic displacement of the detector’s particles until after the observed particle reached the screen. Now, the wavefunction in the interference region is entangled with the which-way detector status as

$$\Psi(x, t) = \frac{1}{\sqrt{2}}(\psi_L(x, t)|_{\text{no}}^{\text{yes}} + \psi_R(x, t)|_{\text{yes}}^{\text{no}}). \quad (2.17)$$

This definitively destroys the interference pattern but the symmetry of the system and of the trajectories is not changed. The crucial element of this scenario is now the fact that the wavefunction  $\psi_L$  does not vanish in the left half of the screen and consequently there will always be particles detected on the “wrong” half of

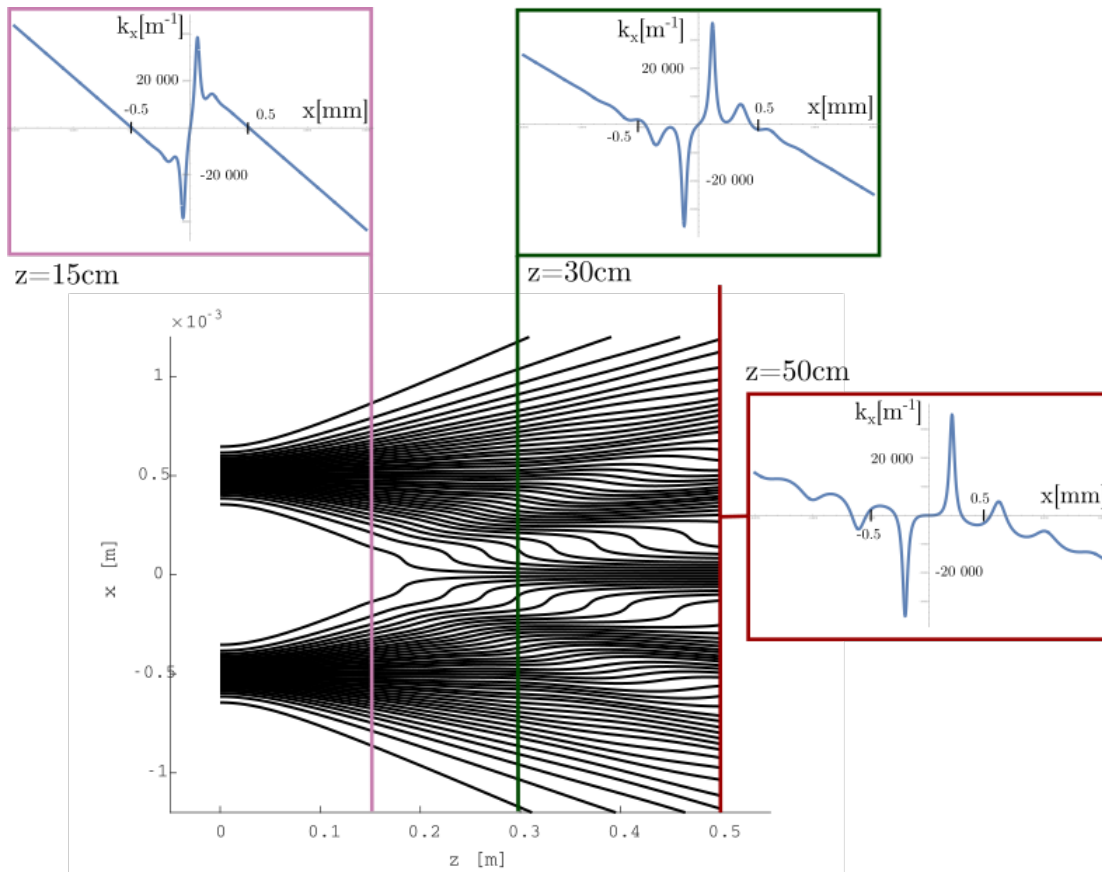


**Figure 2.4:** Bohmian trajectories of a Gaussian double slit together with their transverse momentum profile at  $z = 15$  cm,  $z = 30$  cm and  $z = 50$  cm. The slit geometry is chosen with a width of  $w_0 = 130$   $\mu\text{m}$  and a slit separation of 1 mm.

the screen, e.g. on the left half, when the which-way detector on the right side has clicked. ESSW conclude that the Bohmian trajectory is here macroscopically at variance with the “actual”, observed one. Thus, Bohmian trajectories must be surrealistic. [4]

In order to experimentally observe these ‘surreal’ trajectories Braverman and Simon proposed [74] an experimental setup, which was later realized by Mahler et al. [7], where, instead of using a which-way detector in front of each slit, in a photon experiment the traversed slit of the photon in the double slit is entangled with the polarization of a second photon the wave function in the interference region is given by

$$\Psi(x, t) = \frac{1}{\sqrt{2}}(\psi_L(x, t)|H\rangle + \psi_R(x, t)|V\rangle). \quad (2.18)$$

Since now the which-way information is encoded in the second particle’s polarization, the ‘surreality’ is that SQM intuition is that the second particle should reliably carry the which-way information about which slit the first particle ‘actually’ went through, but in the experiment it is found that the predicted Bohmian

## 2 Bohmian mechanics and the double slit experiment

trajectories often fail to agree with the outcome of the which-way measurement performed on the second particle [7]. Say, a photon on the left hand side of the screen is detected, whereas its partner photon has the polarization indicating the right slit (V) (see Fig. 2.5).

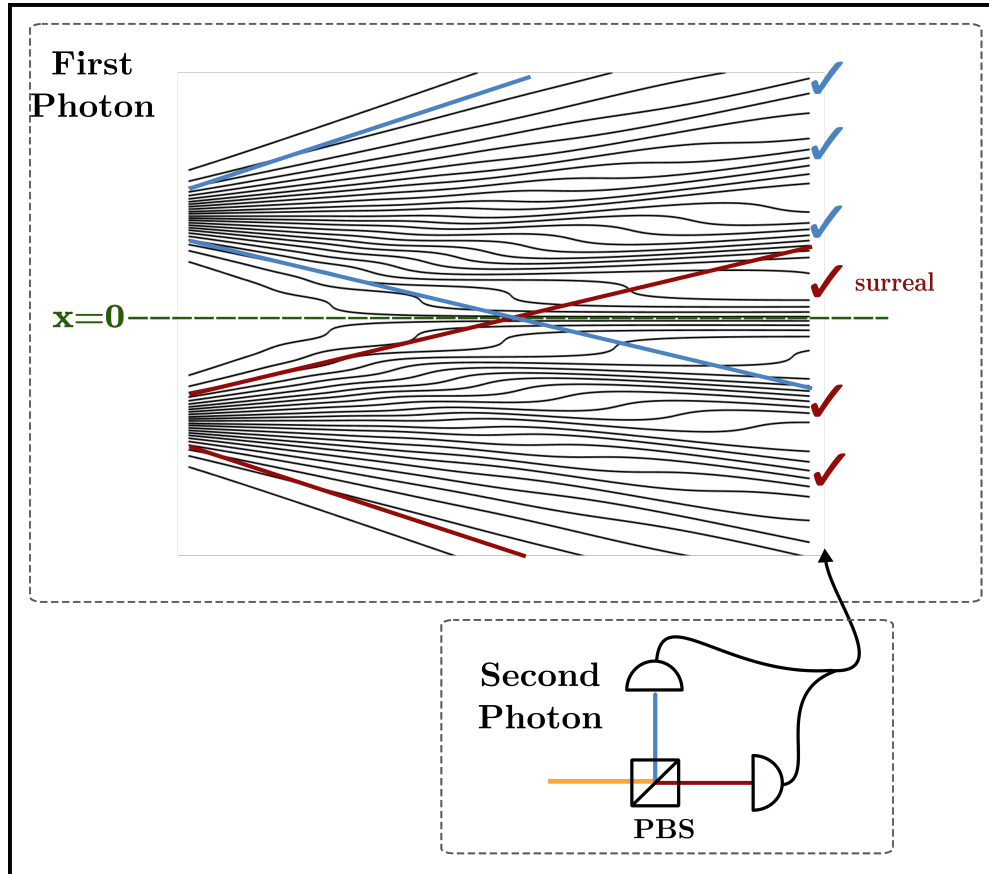


**Figure 2.5:** Illustration of the ‘surreal’ scenario: The which-way information of the first photon is entangled with the polarization of a second photon. Due to the geometry of the setup, the trajectories do not cross  $x = 0$ .

**Defense of the realism of Bohmian trajectories** The attack on the reality of the Bohmian interpretation raised a huge debate among the proponents of the theory [75–79]. While Dürr et al. [76] are accusing the incorrect usage of the theoretical framework and the “self-destructive” argumentation of ESSW, Dewdney et al. [77] see the point in the non-locality of the quantum potential.

Dewdney et al. explain in their paper that, due to the non-locality of the quantum-potential, the detector can be “fooled” and click, even though the particle did not pass through the detector. They emphasize, like Dürr et al., that both theory and calculations must be applied rigorously and consistently in order to avoid confusion.

The problem of the ‘wrong’ polarization is not a problem in the Bohmian theory. It has to be kept in mind, that in the Bohmian picture the actual particle

position  $Q$  and the argument of the wavefunction  $q$  are separate variables [80]. Therefore, as long as the wave functions of the two slits overlap, as is the case in the interference region, the direction of the polarization can still change, since only position is a property of the particle and everything else, like spin or polarization, is a property of the wavefunction. Hence, due to the entanglement, the second photon can be detected to be  $H$ - or  $V$ -polarized dependent on the amplitudes of the contributing wavefunctions at the position of the first photon in the interference region (see Fig. 2.5). This does not differ from the view of SQM in the point that the polarization of the second photon is also correlated to the detected position of the first photon, but in SQM no association with a trajectory is made.

The experiment by Mahler et al. [7] then provided an illustration of the non-locality of the theory. They claim to demonstrate the non-locality present in Bohmian mechanics by showing that the trajectory of the photon in the slit system is affected by the remote choice of the basis, the second photon is measured in [7]. Moreover, they also addressed the surreality issue and indeed observed Bohmian trajectories originating at the right slit accompanied by which-way measurement results associated with the left slit. They find that while traversing the double slit photon 1 enters a region where both wave functions  $\psi_L$  and  $\psi_R$  overlap, leading to correlations between the motion of photon 1 and the polarization of photon 2. The polarization of photon 2 is therefore not constant in time and its final state no longer faithfully records the which-way information of the first photon. It is concluded that the non-locality arising from the necessary entanglement is the reason for this ‘surreal’ behavior and the ‘surreality’ is only a compelling visualization of the “non-locality inherent in any realistic interpretation of quantum mechanics” [7].

### Delayed choice measurement

Delayed choice experiments have highlighted peculiarities and non-classical features of the theory (for a summary see [81]) since the beginning of QM. The main idea is to choose later, when the particle has already entered an interferometer or in our double-slit experiment the interference region, if one is going to perform a which-way measurement or not and therefore observe interference or not. It is also possible to observe a continuous transformation between the particle and wave character, which rules out the naive classical interpretation that every quantum system behaves either definitely as a particle or definitely as a wave by adapting a priori to the specific experimental situation. [81]

In the Bohmian context it is very interesting to consider situations, in which the quantum potential is changed, after the particle has already entered the interference region. As already mentioned the quantum potential reacts immediately to changes in any part of the system, like altering the slit sizes or performing a which-way measurement at any point. In the setup considered in Fig. 2.5, the which-way degree of freedom of the photon in the double slit is entangled with

## 2 Bohmian mechanics and the double slit experiment

---

the polarization of a second photon outside the slit system via Eq. (2.18), which can be written in real space as

$$\Psi(q_1, q_2) = \frac{1}{\sqrt{2}}(\psi_L(q_1)\psi_H(q_2) + \psi_R(q_1)\psi_V(q_2)). \quad (2.19)$$

In the Bohmian view the inseparable – even if spacelike separated – evolution of the entangled photons is a consequence of the non-locality of the theory. Thus a deeper investigation of the non-local features can be performed, when separating the photons and performing spacelike separated (delayed) which-way measurements on them.

**Different measurement scenarios** Dependent on the point in time of the polarization measurement of the second photon, which can be performed before, while or after the first photon has entered the interference region, in BM the photons will take different paths and result in different patterns on the screen. The complete calculation of those has already been made in detail in the master thesis of Maria Galli [20] in chapter 3.4 and will only be briefly summarized here.

The interference pattern will only be observed, when the entanglement is destroyed before photon 1 reaches the slit by projecting photon 2 onto some polarization state, e.g.  $P$ , without gaining information about its initial polarization state. When calculating the Bohmian velocity via Eq. (2.14), one sees interference terms containing the product of  $\psi_L$  and  $\psi_R$ . When performing the polarization measurement and therefore obtaining complete information about the second photon's polarization in the  $H/V$  basis before the photon is entering the double slit, which corresponds to the closure of one slit, the interference pattern is destroyed and no interference terms are guiding the particle evolution; the particle is guided either only by  $\psi_L$  or only by  $\psi_R$ . When photon 2 is not measured at all or only after the first photon had already been detected, the interference pattern is still destroyed, but in the interference region the photon is guided by the complete entangled wave function Eq. (2.18), which results in a velocity field which depends on both the waves  $\psi_L$  and  $\psi_R$  but does not show any interference. [20]

In order to illustrate the influence of the time ordering of the two measurements in BM, the polarization measurement on photon 2 is considered in  $\hat{\sigma}_x$ -direction. The wavefunction (2.19) can be expressed in this basis for photon 2 as

$$\Psi(q_1, q_2) = \frac{1}{\sqrt{2}}[(\psi_L(q_1) + \psi_R(q_1))\psi_P(q_2) + (\psi_L(q_1) - \psi_R(q_1))\psi_M(q_2)], \quad (2.20)$$

where  $\psi_{P,M}(q_2)$  are the wavefunctions of photon 2 according to  $P$ - and  $M$ -polarization. Same as in SQM there is no difference in the observed interference pattern in BM when only photons with a  $P$ -polarized partner photon 2 are entering the slits, or when only photons are counted for the reconstruction of the pattern when photon 2 is detected to be  $P$ -polarized after photon 1 already reached the screen. In case photon 2 is projected onto  $P$  before photon

1 is entering the slit, thus  $\psi_M(q_2) = 0$ , it is obvious that photon 1 is guided by the interfering wave  $\psi(q_1) \propto \psi_L(q_1) + \psi_R(q_1)$ , resulting in an interference pattern dependent on the polarization measurement. In the other case when the measurement on photon 2 is performed when photon 1 already reached the screen, photon 1 is guided by the entangled wavefunction (2.19) through the interference region, not resulting in an interference pattern. Nevertheless, the outcome of the polarization measurement is dependent on the point of impact on the screen of photon 1. When photon 1 arrived at position  $Q_1$  where  $|\psi_L(Q_1) + \psi_R(Q_1)|^2$  is minimal and therefore  $|\psi_L(Q_1) - \psi_R(Q_1)|^2$  maximal, photon 2 will be detected to be  $M$ -polarized, whereas it will be  $P$ -polarized for photon 1 arriving in a maximum of  $|\psi_L(q_1) + \psi_R(q_1)|^2$ . This is why the interference pattern can be reconstructed taking only the photons with a later detected  $P$ -polarized partner into account. The difference in BM is that the points of impact on the screen are reached on different paths according to the different quantum potential guiding the photons through the interference region dependent on the time ordering of the measurements.

When photon 2 is spacelike separated from photon 1 while the measurement is performed, the non-local character of the theory will become visible, as the two participating photons affect each other while being separated. Also the special scenario in which the polarization is measured, while the photon is in the interference region, will lead to an immediate change of the quantum potential and hence result in an immediate change of the photon's paths, which makes possible to directly observe the effect of a delayed choice measurement.

## 2.3 Observing Bohmian trajectories

In order to make these trajectories visible, techniques are needed to measure the path of particles in an experiment. In this section two possible techniques for observation of Bohmian trajectories are introduced. Afterwards also the resolution of the scenarios is analyzed.

### 2.3.1 Bohmian velocity as a weak value

The first idea to observe Bohmian trajectories is formulated by Wiseman [5]. Based on the definition of the Bohmian velocity via the quotient of the probability current  $j^\psi(q, t)$  (2.12) and the probability density  $|\psi(q, t)|^2$  (2.14), Wiseman showed that out of infinitely many probability currents  $j$  satisfying the continuity equation (2.11) one “standard”  $j$  can be singled out, when it is determined experimentally as a weak value. With this an operational definition for the Bohmian dynamics is obtained and the Bohmian trajectories can be observed via weak measurement on a large enough ensemble [5].

In order to provide an operational definition for the velocity of a pointlike particle Wiseman introduces the “naively observable” velocity as

$$v(q, t) = \lim_{\tau \rightarrow 0} \frac{1}{\tau} (q_f(t + \tau) - \mathbb{E}[q_i(t) \mid q_f(t + \tau) = q]), \quad (2.21)$$

where  $\mathbb{E}[q_i(t) \mid q_f(t + \tau) = q]$  is the average initial position taken over a large ensemble for all of which the result of a following measurement of position at time  $t + \tau$  is  $q$ . For a quantum particle it is plausible to first, at some time  $t$ , perform a weak measurement of the position in order to not disturb the further evolution, and then strongly measure the position at a some later time  $t + \tau$ . In order to gain information about the first position, the weak measurement has to be repeated on a large ensemble of identically prepared particles, but still it won’t be possible to prepare the particles such that they all follow the same trajectory. This is why only particles should be taken into account for the determination of the velocity at a certain position which are found later at this certain position by the strong measurement.

It is therefore reasonable to rewrite the conditioned initial position as a weak value defined in section 1.4

$$\mathbb{E}[q_i(t) \mid q(t + \tau) = q_f] = \text{Re} \left[ \frac{\langle q_f | \hat{U}(\tau) \hat{q} | \psi(t) \rangle}{\langle q_f | \hat{U}(\tau) | \psi(t) \rangle} \right]. \quad (2.22)$$

Here  $\hat{U}$  is the unitary evolution the particle experiences in between the first and second measurement corresponding to the Hamiltonian  $\hat{H}$  of the system:

$$\hat{U}(\tau) = e^{-\frac{i}{\hbar} \hat{H} \tau}, \quad \hat{H} = \frac{\hat{p}^2}{2m} + V(\hat{q}). \quad (2.23)$$

With this Eq. (2.21) can be simplified to a general expression for the average velocity at the position of the postselection as

$$v(q_f, t) = \text{Re} \left[ \frac{\langle q_f | i[\hat{H}, \hat{q}] | \psi(t) \rangle}{\hbar \langle q_f | \psi(t) \rangle} \right], \quad (2.24)$$

which simplifies with  $i[\hat{H}, \hat{q}] = \frac{\hat{p}}{m}$  to the Bohmian velocity

$$v(q_f, t) = \frac{1}{m} \text{Re} \left[ \frac{\langle q_f | \hat{p} | \psi(t) \rangle}{\langle q_f | \psi(t) \rangle} \right] \quad (2.25)$$

This “naive” way [5] yields the Bohmian velocity (2.14). This can be seen when reformulating the Bohmian velocity to Eq. (2.25) with  $\langle q | \hat{p} | \psi \rangle = -i\hbar \frac{\partial}{\partial q} \psi(q)$  and therefore  $\nabla \psi(q) = \langle q | \frac{i}{\hbar} \hat{p} | \psi \rangle$ , such that

$$v(q) = \frac{\hbar}{m} \text{Im} \left[ \frac{\nabla \psi(q)}{\psi(q)} \right] = \frac{1}{m} \text{Im} \left[ \frac{\langle q | i \hat{p} | \psi \rangle}{\langle q | \psi \rangle} \right] = \frac{1}{m} \text{Re} \left[ \frac{\langle q | \hat{p} | \psi \rangle}{\langle q | \psi \rangle} \right].$$

**First realization by Kocsis et al.** The first realization of a measurement of Bohmian trajectories via a weak measurement has been done by Kocsis et al. [6] in 2011. They perform a weak measurement of the photon momentum by using the photon’s polarization as a pointer. The postselection on the particle’s position combined with the measurement of the polarization yielded the momentum weak value. By performing such a measurement throughout the interference region of a double slit setup, the average photon trajectories as discussed in section 2.2.2 could be reconstructed. An experimental implementation of such an weak measurement will be discussed in section 3.3.

### 2.3.2 Poynting vector as Bohmian velocity

Another surprisingly intuitive way to measure the Bohmian velocity is to measure the wavefront directly, as the trajectories are oriented normal to them (see section 2.1.3). In a paper from 2013 Bliokh et al. [82] show that the weak momentum measurement corresponds to measuring the transverse Poynting vector. This also explains that Wiseman’s idea for massive particles can be transferred to massless particles like photons.

For an electromagnetic wave with magnetic field  $\mathbf{B}(\mathbf{r})$  and electric field  $\mathbf{E}(\mathbf{r})$  the Poynting vector, representing the energy current, in Gaussian units is given by

$$\mathbf{P} = \frac{c}{2} \text{Re}[\mathbf{E}^* \times \mathbf{B}]. \quad (2.26)$$

The Poynting vector can be written in terms of two physically meaningful contributions, orbital and spin currents  $\mathbf{P}_o$  and  $\mathbf{P}_s$

$$\mathbf{P} = \frac{c^2}{2\omega} \text{Im}[\mathbf{E}^* (\nabla) \mathbf{E}] + \frac{c^2}{4\omega} \nabla \times \text{Im}[\mathbf{E}^* \times \mathbf{E}] = \mathbf{P}_o + \mathbf{P}_s, \quad (2.27)$$

## 2 Bohmian mechanics and the double slit experiment

---

with  $[\mathbf{E}^*(\nabla)\mathbf{E}]_i = \sum_j E_j^* \nabla_i E_j$  [83].

Because the spin current does not transport energy, and only generates the spin angular momentum of the field, the orbital part of the Poynting vector should be associated with the observable momentum density of the field. Furthermore, for a linearly polarized field the spin contribution vanishes  $\mathbf{P}_s = 0$ , such that the Poynting vector coincides with its orbital part  $\mathbf{P} = \mathbf{P}_o$ . [82]

Considering a paraxial, monochromatic and uniformly polarized wave, the complex electric field can be written as

$$\mathbf{E}(\mathbf{r}, t) = \mathbf{e}\psi(\mathbf{r})e^{-i\omega t}, \quad (2.28)$$

where  $\mathbf{e}$  is the transverse complex unit polarization and  $\psi(\mathbf{r})$  is the complex scalar field.

Therefore, the ratio of the orbital Poynting vector to the energy density  $W = \frac{|\mathbf{E}|^2}{2}$ , one obtains

$$\frac{\mathbf{P}_o(\mathbf{r})}{W(\mathbf{r})} = \frac{c^2 \text{Im}[\psi^*(\nabla)\psi]}{\omega|\psi|^2}. \quad (2.29)$$

Except for the constant prefactor this formula equals the expression for the Bohmian velocity (2.14). It is well known that the direction of the Poynting vector coincides with the direction of the wavevector  $\mathbf{k}$  in an isotropic medium like e.g. air [84]. Consequently the Bohmian trajectories can be reconstructed by directly measuring the wavevector of the photons.

### 2.3.3 Uncertainty analysis

Since the two ways extracting the Bohmian velocity explained above are equivalent, it is interesting to have a look at the statistical limitations of the measurement, and therefore determine when trajectories are observable. This will be done in the following section.

**Weak measurement scenario** In this measurement scenario the weak value of the momentum is proportional to the shift of the pointer variable according to equation (1.54), such that the Bohmian momentum is given by

$$\gamma k_B \approx E_R,$$

where  $E_R$  is the expectation value of the pointer shift and  $\gamma$  is the measurement strength. Due to the fact that this measurement is performed repeatedly  $N$  times, for each run a value  $E_M$  is obtained according to the Gaussian probability distribution [85]

$$p(E_M | E_R) = \frac{1}{\sqrt{2\pi}\sigma} e^{-\frac{(E_M - E_R)^2}{2\sigma^2}} \quad (2.30)$$

centered around  $E_R$  with a standard deviation  $\sigma = \sqrt{\frac{1-E_R^2}{N}}$ . Hence, the uncertainty of the weak measurement  $\sigma_{k_B}$  decreases with an increasing number of measurements as

$$\sigma_{k_B} = \frac{\sigma}{\gamma} = \frac{\sqrt{1 - (\gamma k_B)^2}}{\gamma \sqrt{N}}. \quad (2.31)$$

As the position of the particle can never be determined more precise than the measurement strength, one can define

$$\sigma_x = \gamma. \quad (2.32)$$

Hence from Eq. (2.31) it follows that for a single measurement the product of the uncertainties of the momentum and position measurement are constant for  $\gamma$  being small

$$\sigma_x \sigma_{k_B} = c. \quad (2.33)$$

**Wavefront measurement** To perform a wavefront measurement in an experiment, it is common to use an Shack-Hartmann-Sensor [86]. It consists of a lens array and a 2D detector. An incoming collimated beam is focused by the lenses onto the detector, where the location of the different foci on the detector depends on the angle of the incident wave vector at the respective lens. Therefore, the wavefront can be reconstructed through the positions of the foci at each lens (see Fig. 2.6). In a paraxial approximation, assuming propagation in  $z$ -direction with only small deviations only in  $x$ -direction by the angle  $\theta$ , the direction of the incident wavevector and the focus position on the detector  $x_f$  are connected via the relation

$$\tan \theta = \frac{x_f}{f}, \quad (2.34)$$

where  $f$  is the focal length of the lens.

Theoretically, the wavefront measurement can be regarded as a determination of position and momentum at the same time: the photon was somewhere in the area of the lens with a momentum proportional to the position on the detector. The accuracy of these two measurements is determined by the transformation of the lens, which is lower bounded by Heisenberg's uncertainty relation

$$\Delta k_x \Delta x \geq \frac{1}{2}, \quad (2.35)$$

where  $\Delta k_x$  with  $p = \hbar k$  is proportional to the momentum uncertainty and  $\Delta x$  is proportional to the lens pitch.

The incident wavefronts to each lens of the array can be approximated by plane waves (see Fig. 2.6). An easy and quick way to categorize the order of magnitude of  $\Delta k_x$  is to assume a Gaussian beam with its waist of size  $w_0 = \Delta x$  directly in

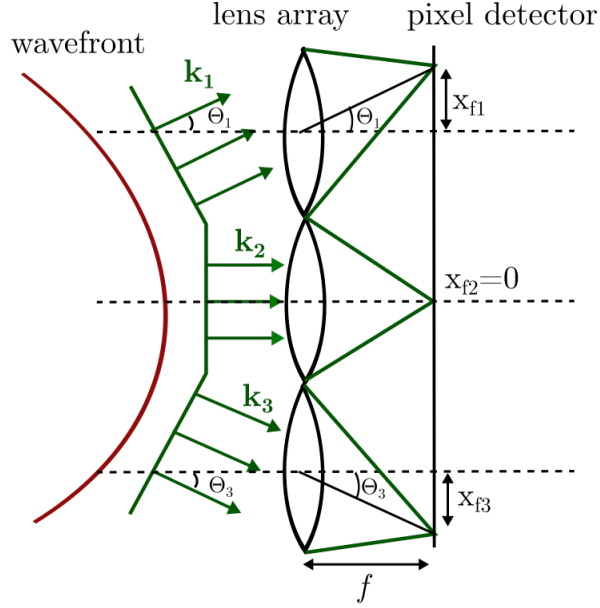


**Figure 2.6:** Schematic illustration of a Shack-Hartmann wavefront sensor. The wavefront is imaged by a lenslet array onto the imageplane, where the deviations  $x_f$  from the center position indicate the average direction of the wavefront in the area of one lenslet.

front of the lens. The focus spot size after the lens  $w'_0$  depends then on the initial beam characteristics  $\lambda$ ,  $w_0$  and the focal length  $f$  of the lens via [87]

$$w'_0 = \frac{w_0}{\sqrt{1 + \left(\frac{\pi w_0^2}{\lambda f}\right)^2}}. \quad (2.36)$$

Hence, a detected photon at position  $x_f$  arises from a Gaussian distribution with standard deviation  $\frac{w'_0}{2}$  and its position can not be determined more precisely than within this standard deviation. As the deviation of the propagation direction in  $x$ -direction is small compared to the total wave vector  $k_z \approx |\mathbf{k}|$  and therefore

$$k_x \approx \frac{2\pi}{\lambda} \tan \theta = \frac{2\pi x_f}{\lambda f}, \quad (2.37)$$

holds, which lets us define the uncertainty for the determination of the wave vector in  $x$ -direction:

$$\Delta k_x = \frac{\pi w'_0}{\lambda f} = \frac{\pi w_0}{\lambda f} \frac{1}{\sqrt{1 + \left(\frac{\pi w_0^2}{\lambda f}\right)^2}}. \quad (2.38)$$

Eq. (2.36) can be approximated for  $\frac{w_0^2}{\lambda f} \gg 1$  as

$$w'_0 = \frac{\lambda f}{\pi w_0} \quad (2.39)$$

which lets us write the uncertainty for the momentum measurement as

$$\Delta k_x = \frac{1}{w_0}. \quad (2.40)$$

With  $\Delta x \propto w_0$  this also reduces to a constant relationship between the uncertainties in momentum and position measurement like for weak measurements (2.33)

$$\Delta x \Delta k_x = c. \quad (2.41)$$

By repeating the experiment and detecting  $N$  photons at each lens, the uncertainty decreases with  $\frac{1}{\sqrt{N}}$ , which allows to measure the  $k_x$  distribution as accurate as desired.

Figure 2.7 shows the theoretically expected  $k_x$  distribution for  $\lambda = 810$  nm 40 cm behind a double slit of 1 mm separation in red. The  $k_x$  profile is then averaged over a specific interval in  $x$  given by the size of one lens of the SHS. The uncertainty is then calculated by Eq. (2.38) for an initial waist of half of the lens size and indicated by the vertical lines. Obviously, for big lenses the interference pattern can never be resolved, as the uncertainty of the position determination is too large. However, the uncertainty on the momentum is small, which is why in the area of the first intensity minimum, where the momentum is maximal, the lens could still resolve that  $k_x$  is positive or negative dependent on which side of the intensity maximum the photon is detected (Fig. 2.7 (a)). However, it should be noted here, that the approximation of a Gaussian or plane incident wave does not really work anymore, as the wavefront is strongly curved in the interval of the large lens. Smaller lenses (Fig. 2.7 (b)) better resolve the position of the photons but lead to a bigger uncertainty in the momentum space, such that a single photon measurement had an uncertainty such big that the direction of the measured momentum wouldn't be resolvable at all.

### 2.3.4 Demonstration of a wavefront measurement

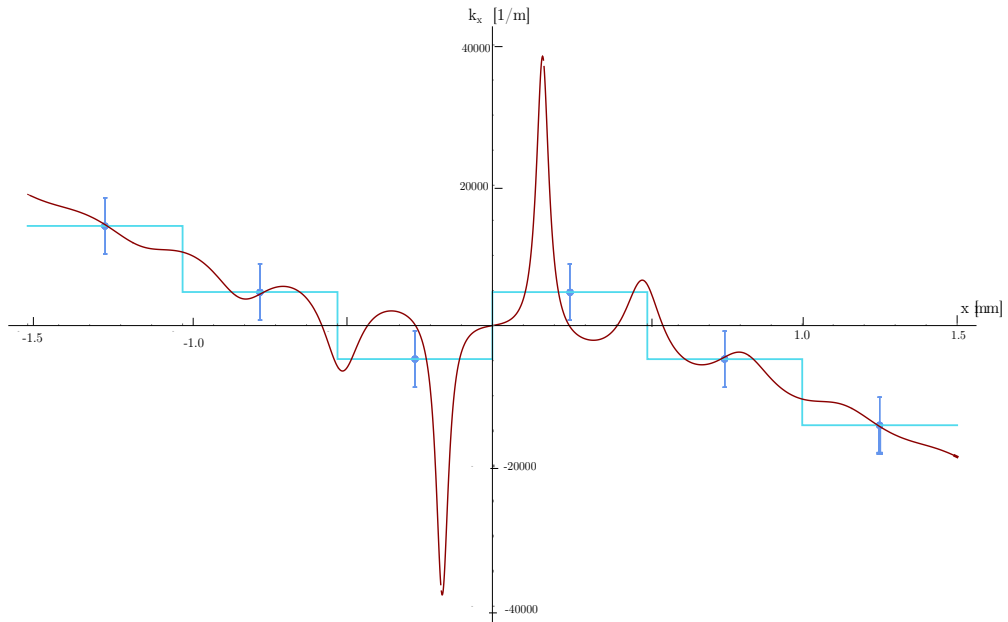
In order to test the previous proposition, the wavefront of the double slit interference was reconstructed at one position in the the interference region by a Thorlabs Shack-Hartmann wavefront sensor WFS150. This sensor uses an array of 39 lenslets each of the size of 150  $\mu\text{m}$ . The best image was obtained, when looking at only a small area of the interference pattern, which is why for this test the wavefront is only reconstructed in an area of approximately 1 mm in the region of the main interference maximum.

The observed wavefront was then compared to the theoretically expected one which is obtained by the  $z$ -profile of constant phase of the wavefunction given by

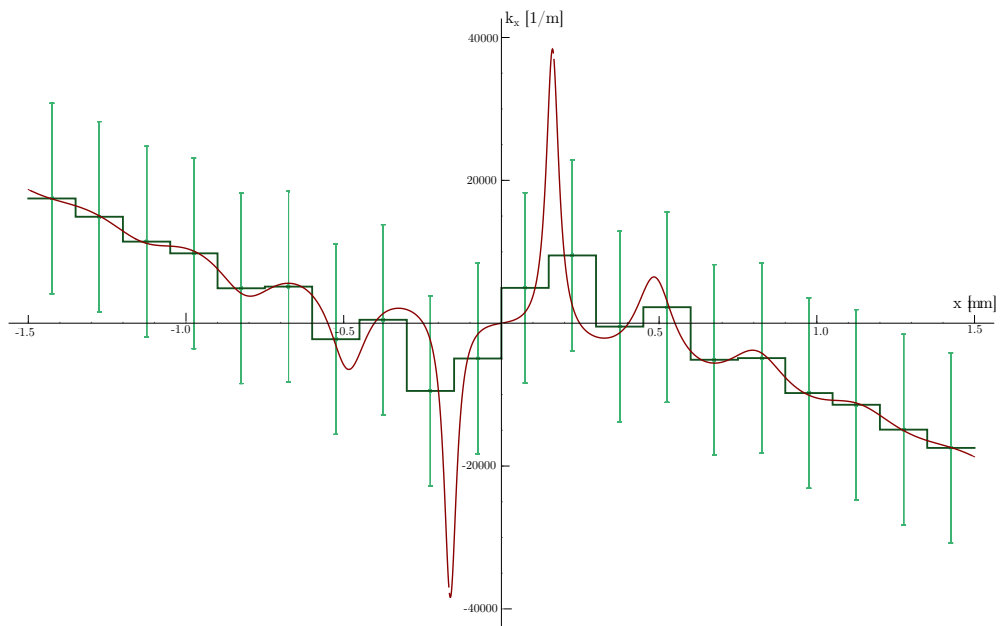
$$\psi(x, z) = \psi_G(x - x_{sep}, z) + e^{i\phi} \psi_G(x + x_{sep}, z), \quad (2.42)$$

where the slits are separated by and the slits are separated by  $2x_{sep}$  with  $x_{sep} = 0.978$  mm and  $\psi_G(x, z)$  is the wavefunction of one of the slits described by a

## 2 Bohmian mechanics and the double slit experiment



(a)  $x_{pitch} = 500 \mu\text{m}$  ,  $f = 13.8 \text{ mm}$



(b)  $x_{pitch} = 150 \mu\text{m}$  ,  $f = 5.6 \text{ mm}$

**Figure 2.7:** Theoretical transverse momentum distribution together with their averaged values for two different lens pitches  $x_{pitch}$  and the error bars calculated via Eq. (2.38).

Gaussian beam dependent on the waist  $w_0 = 115 \mu\text{m}$  and the wavelength  $\lambda = 810 \text{ nm}$  as described in section 3.1.1. For the extraction of the phase  $\phi$  the area was again imaged with a CCD camera and theoretical intensity profiles with various  $\phi$  were fitted onto the observed one until they matched for the correct phase

$\phi \approx 6.0319$ . The theoretically expected together with the measured wavefront at a distance of  $z = 44.5$  cm from the slits is shown in Fig. 2.8.

In the theoretical profile in red the large central dip is caused by the main maximum of the interference pattern, while the smaller dips are caused by the side maxima. Maxima in the wavefront profile stand for minima in the interference pattern as the  $k$ -vector is pointing away from this region. Hence, the transverse wave vector  $k_x$  vanishes at every point of inflection of the wavefront, causing the bright fringes of the interference pattern for the wavefront's minima and dark fringes for maxima. The pink curve is the averaged theoretical wavefront over the area of the lenslets. The blue curve is the measured wavefront approximately in the center in  $y$ -direction.

The main minimum is clearly visible in the measured data. The influence of a small tilt of the camera with respect to the propagation direction on the measured direction of the  $k$ -vector and hence on the reconstructed wavefront, can be a reason for the slope at the edges which cause the asymmetry of the measured profile not fitting to the theory. Also, due to the size of the lenslets, the reconstructed wavefront is very sensitive to the position of the array in  $x$ -direction and therefore the choice of the averaged areas. A more accurate alignment is thus required in order to obtain an even better image of the observed wavefront, which goes beyond a simple test of the sensor's capabilities. Nevertheless, while a Gaussian wavefront would not change its curvature, the wavefront observed here does significantly, suggesting fruitful ways to measure the complete wavefront, providing the possibility of reconstructing Bohmian trajectories.

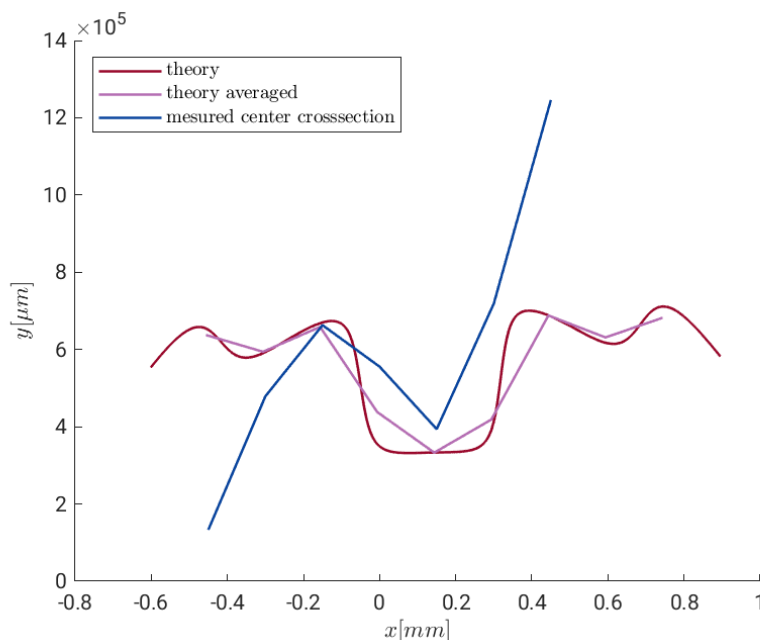


**Figure 2.8:** Theoretically expected and measured wavefront in a double slit at a distance  $z = 44.5$  cm from the slits.



# 3 Experimental implementation

In this chapter the experimental realization of the experiment for the observation Bohmian trajectories via weak measurement is explained. Therefore, first the optical concepts which are needed to understand the experimental setup are explained, special attention is paid to the spontaneous parametric downconversion process needed to build a entangled photon source. Second, the experimental implementation of the entangled photon source, the double slit, the trajectory observations and the which-way measurement is explained.

## 3.1 Optics

### 3.1.1 Gaussian beam

The transverse modes of lasers which are generated in a laser cavity can be described in terms of Hermite Gaussian  $TEM_{mn}$  modes. The most commonly used laser mode is the  $TEM_{00}$  also known as the Gaussian beam. The field amplitude  $E_G$  of a Gaussian beam propagating in  $z$ -direction can be written as

$$E_G(z, r) = E_0 \frac{w_0}{w(z)} e^{-\left(\frac{r}{w(z)}\right)^2} e^{-ik \frac{r^2}{R(z)}} e^{-i(kz - \eta(z))}, \quad (3.1)$$

such that  $r = \sqrt{x^2 + y^2}$  denotes the distance to the propagation axis and  $k$  is the wavevector in the medium. The place of the smallest transverse extension of the beam, the so called beam waist  $w_0$ , is located at  $z = 0$ .

The transverse profile of a Gaussian beam is given by a Gaussian distribution. The beam radius  $w(z)$  is defined as the value of  $r$  where the field amplitude has dropped to  $\frac{1}{e}$  and therefore the intensity to  $\frac{1}{e^2}$ . The  $z$ -dependence of the beam radius is given by

$$w(z) = w_0 \sqrt{1 + \left(\frac{z}{z_R}\right)^2} \quad (3.2)$$

with the characteristic Rayleigh length  $z_R$  given by Eq. (3.3) defined as the distance from  $z = 0$  at which the area of the beam is doubled, i.e. the radius has increased by a factor of  $\sqrt{2}$  compared to the waist,

$$z_R = \frac{n\pi w_0^2}{\lambda}, \quad (3.3)$$

where  $n$  is the refractive index of the medium and  $\lambda$  the wavelength of the described light. For distances from the waist  $|z| \gg z_R$  the beam radius is approximately linear in  $z$  as the beam spreads out over a cone with half angle  $\theta_0 = \frac{\lambda}{\pi w_0}$ .

### 3 Experimental implementation

---

The curvature of the wavefronts, denoting points of constant phase of the wave, is given by the curvature radius

$$R(z) = z \left[ 1 + \left( \frac{z_R}{z} \right)^2 \right], \quad (3.4)$$

which goes to infinity at  $z = 0$ , hence describing plane waves at the waist while approximately spherical wavefronts at distances much larger than the Rayleigh length are obtained.

The Guoy phase  $\eta(z)$  arises from a phase retardation of  $\pi$  the beam acquires traveling through the focus from  $z = -\infty$  to  $z = +\infty$ :

$$\eta(z) = \arctan \left( \frac{z}{z_R} \right). \quad (3.5)$$

In experimental practice, there is never an ideal Gaussian beam. Therefore the quality of a beam is evaluated in terms of its deviation from the ideal Gaussian beam. Using the second moment of the intensity profile, the beam radius of any arbitrary beam propagating in  $z$  direction and waist at  $z_0$  can be expressed via [88]

$$w_{x,y}^2 = w_{0x,y}^2 + (M_{x,y}^2)^2 \cdot \left( \frac{\lambda}{4w_{0x,y}} \right)^2 \cdot (z - z_{0x,y})^2 \quad (3.6)$$

where  $M_x^2$  and  $M_y^2$  are parameters characteristic of the particular beam describing the evolution of the beam radii in x- and y-directions respectively. These so called ‘‘M-squared’’-values give a measure for the beam quality in the sense that  $M_{x,y}^2 \geq 1$  for any arbitrary beam profile with the lower limit of an ideal Gaussian beam with  $M_{x,y}^2 = 1$ . A typical experimental beam can therefore be fully characterized by the six parameters  $M_x^2$ ,  $M_y^2$ ,  $w_{0x}$ ,  $w_{0y}$ ,  $z_{0x}$  and  $z_{0y}$ .

#### 3.1.2 Optical components

**Optical filters** Optical filters selectively transmit only a certain part of the spectrum. In general, they either absorb unwanted light or reflect it. A *dichroic filter* works by reflecting undesired wavelengths, while transmitting the wanted portion of the spectrum through the addition of interference coatings, whereas an *absorptive filter* blocks light of specific wavelengths dependent on the absorption properties of the glass substrate used [89]. Additionally *bandpass and edgepass filters* are distinguished. Edgepass filters are determined by their cut-off or cut-on wavelength, the wavelength where the transmission intensity has fallen (cut-off) or risen (cut-on) to 50%, which means that the spectrum is divided into one part transmitted and the other part reflected or absorbed by the filter. Bandpass filters are only transmitting a specific narrow region of the spectrum determined by a central wavelength and the full width-half maximum (FWHM) which describes the spectral bandwidth over which a bandpass filter transmits light. The central wavelength of a bandpass filter is dependent on the angle of incidence on the filter.

The relationship between the angle of incidence  $\phi$  and the wavelength drift can be approximated for  $\phi < 15^\circ$  [90]

$$\frac{\lambda_\phi}{\lambda_0} = \frac{\sqrt{n_F^2 - \sin^2 \phi}}{n_F}, \quad (3.7)$$

where  $\lambda_0$  is the central wavelength at,  $\lambda_\phi$  the shifted wavelength at an angle of incidence  $\phi$  and  $n_F$  the index of refraction of the filter.

**Polarization devices** It is possible to describe the polarization state light with the Jones vector [87]

$$\mathbf{J} = \begin{pmatrix} E_x e^{i\phi_x} \\ E_y e^{i\phi_y} \end{pmatrix}, \quad (3.8)$$

where the components  $E_i$  and  $\phi_i$  denote the amplitude and the phase of the electric field perpendicular to the propagation direction  $z$ . The polarization space corresponds exactly to the space of a qubit and thus the polarization can be expressed in the quantum formalism using to the natural basis states defined in section 1.1 with

$$|H\rangle := \begin{pmatrix} 1 \\ 0 \end{pmatrix}, \text{ and } |V\rangle := \begin{pmatrix} 0 \\ 1 \end{pmatrix}. \quad (3.9)$$

The change of the polarization of a plane wave by an optical system can be described using the input and output Jones vectors  $\mathbf{J}_1$  and  $\mathbf{J}_2$  and the transmission Jones matrix  $\hat{T}$  as [87]

$$\mathbf{J}_2 = \hat{T}\mathbf{J}_1. \quad (3.10)$$

In the quantum formalism this transformation corresponds to a unitary rotation of the polarization qubit. In optical experiments, these polarization rotations are implemented by so called *waveplates* or wave retarders, which consist of birefringent, transparent plates of anisotropic crystals, introducing a phase delay between two polarization states, dependent on the amount of birefringence (see section 3.2) and the adjustment of the optical axis of the waveplate. *Half-wave plates* (HWP) introduce a phase delay between the ordinary and extraordinary beam of  $\pi$  and thus can rotate the axis of linear polarization, while *quarter-wave plates* (QWP) introduce a phase of  $\pi/2$  and can therefore convert linear to circular polarization and vice versa.

The Jones or equivalent unitary matrices of a HWP or QWP rotated by the angle  $\theta_H$  or  $\theta_Q$  with respect to the horizontal polarization are given by [91]

$$\begin{aligned} \hat{T}_{HWP} &= \begin{pmatrix} \cos^2 \theta_H - \sin^2 \theta_H & 2 \cos \theta_H \sin \theta_H \\ 2 \cos \theta_H \sin \theta_H & \sin^2 \theta_H - \cos^2 \theta_H \end{pmatrix}, \\ \hat{T}_{QWP} &= \begin{pmatrix} \cos^2 \theta_Q + i \sin^2 \theta_Q & (1 + i) \cos \theta_Q \sin \theta_Q \\ (1 - i) \cos \theta_Q \sin \theta_Q & \sin^2 \theta_Q + i \cos^2 \theta_Q \end{pmatrix}. \end{aligned} \quad (3.11)$$

### 3 Experimental implementation

---

*Polarizers* transmit a desired polarization state while reflecting, absorbing or deviating the other part. The Jones matrix of a linear polarizer with a transmission axis sharing an angle  $\theta_P$  with the horizontal axis is given by [87]

$$\hat{T}_{Pol} = \begin{pmatrix} \cos^2 \theta_P & \cos \theta_P \sin \theta_P \\ \cos \theta_P \sin \theta_P & \sin^2 \theta_P, \end{pmatrix} \quad (3.12)$$

such that only light linearly polarized in the direction defined by  $\theta_P$  is transmitted by the polarizer.

## 3.2 Birefringence and nonlinear optics

In a nonlinear optical medium the relation between the dielectric Polarization  $P$  and the electric field  $E$  is not linear, but instead described by the matter equation [84]

$$P(E) = \epsilon_0(\chi^{(1)}E + \chi^{(2)}E^2 + \chi^{(3)}E^3 + \dots), \quad (3.13)$$

where  $\chi^{(1)}$  is the linear dielectric susceptibility,  $\chi^{(n)}$  are the dielectric susceptibility coefficients of higher order and  $\epsilon_0$  is the vacuum permittivity. Under most conditions the nonlinear contributions are very small and can be neglected, but for some materials or very high intensities of the electric fields the higher order terms become significant. In this section second order nonlinear processes will be regarded such that the expansion can be cut off after the quadratic term.

Note that in general the polarization and the  $E$ -field are vectors with three components and the susceptibilities  $\chi^{(n)}$  are tensors of rank  $n + 1$  [84], such that (3.13) can be reformulated to

$$P_i = \sum_j \chi_{ij}^{(1)} E_j + \sum_{jk} \chi_{ijk}^{(2)} E_j E_k \quad (i, j, k) = 1, 2, 3. \quad (3.14)$$

The linear susceptibility tensor  $\chi^{(1)}$  has – when written in an appropriate coordinate basis, namely the principal axes of the medium – three non-vanishing components which are directly connected to the refractive indices of the medium  $n_i = \sqrt{1 - \chi_{ii}^{(1)}}$ , where  $i = (1, 2, 3)$  represents the X, Y and Z axes of the coordinate system respectively.

When  $n_1 \neq n_2 \neq n_3$  the crystal is called biaxial, whereas in the special case when two refractive indices are equal  $n_o = n_1 = n_2$  and the third one is different  $n_e = n_3 \neq n_o$  the crystal is called uniaxial [92, 93]. The refractive indices can be calculated by the Sellmeier equation

$$n_i = \sqrt{A_i + \frac{B_i}{\lambda^2 - C_i} + D_i \lambda^2}, \quad (3.15)$$

where the direction dependent coefficients  $A_i, B_i, C_i, D_i$  can be found in the literature [93].

### 3.2.1 Propagation of polarized light in birefringent crystals

**Uniaxial crystals** In uniaxial crystals the direction with the refractive index  $n_o$  is called the optical axis. A beam with a polarization perpendicular to the plane which contains the optical axis of the crystal and the  $\mathbf{k}$ -vector of the beam (principal plane) is called “ordinary” beam and experiences the ordinary refractive index  $n_o$ . A beam with polarization parallel to the principal plane experiences the extraordinary refractive index  $n_e$  and is called “extraordinary” polarized. Hence the polarization of an arbitrarily polarized beam in an uniaxial birefringent crystal can be decomposed in the basis of the crystal axes into two orthogonally polarized components experiencing the two different refractive indices of the medium.

Since the polarization direction of the ordinary beam is always perpendicular to the optical axis the refractive index of the ordinary beam is not dependent on the propagation direction of the beam. The extraordinary refractive index  $n_e$ , however, is a function of the polar angle  $\theta$  between the optical axis and the  $\mathbf{k}$ -vector [92, 93]

$$n_e(\theta) = n_o \sqrt{\frac{1 + \tan^2\theta}{1 + \left(\frac{n_o}{n_e}\right)^2 \tan^2\theta}}. \quad (3.16)$$

When entering a uniaxial birefringent medium from a medium with refractive index  $n_1$ , an ordinary beam is deflected as described by Snell’s law

$$n_1 \sin(\theta_1) = n_o \sin(\theta_{o,2}). \quad (3.17)$$

The  $\mathbf{k}$ -vector of the extraordinary beam is also refracted by Snell’s law, but with the angle dependent refractive index as

$$n_1 \sin(\theta_1) = n_e(\theta) \sin(\theta_{e,2}). \quad (3.18)$$

Additionally its direction is tilted relative to the ordinary beam by the walk off angle  $\rho$  [93]

$$\rho(\theta) = \pm \arctan \left( \left( \frac{n_o}{n_e} \right) \tan(\theta) \right) \mp \theta, \quad (3.19)$$

where the upper signs corresponds to a negative crystal ( $n_o > n_e$ ) and the lower ones for a positive crystal ( $n_o < n_e$ ) [93]. Therefore an arbitrarily polarized beam, when entering a crystal of length  $L$  orthogonal to the input surface, is divided into two orthogonally polarized components, which after the passage through the crystal are separated by (see Fig. 3.1)

$$\delta = L \tan(\rho). \quad (3.20)$$

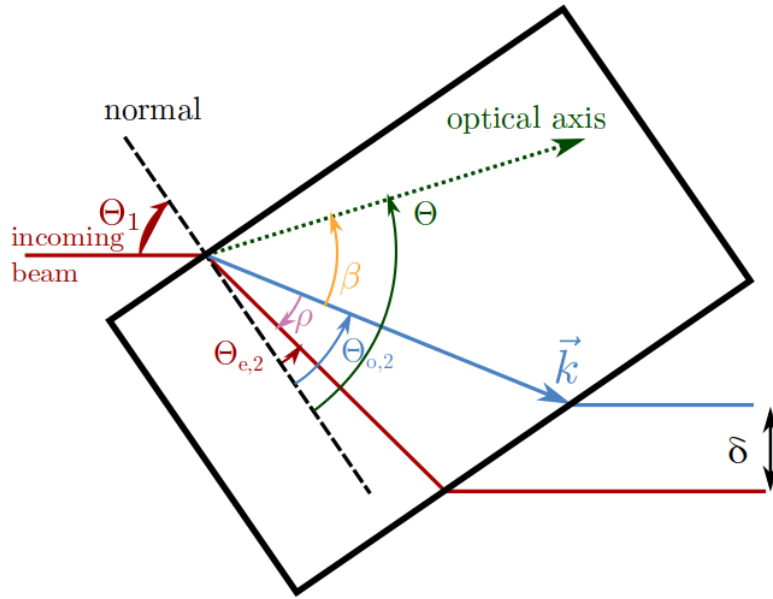


**Figure 3.1:** Definition of the main parameters of the passage of light through an uniaxial birefringent crystal.

**Biaxial crystals** In biaxial crystals – due to Fresnel’s equation [94] – for every wave there are two polarization directions with different refractive indices called the slow and the fast axis with  $n_s > n_f$ . The angular dependence of both refractive indices results in a bilayer structure with four points of interlayer contact through which two optical axes pass [93]. The refractive indices depend both on the propagation direction according to

$$n_{f/s} = \sqrt{\frac{2}{B \pm \sqrt{B^2 - 4C}}} \quad (3.21)$$

$$B = x^2 \left( \frac{1}{n_y^2} + \frac{1}{n_z^2} \right) + y^2 \left( \frac{1}{n_x^2} + \frac{1}{n_z^2} \right) + z^2 \left( \frac{1}{n_x^2} + \frac{1}{n_y^2} \right) \quad (3.22)$$

$$C = \frac{x^2}{n_y^2 n_z^2} + \frac{y^2}{n_x^2 n_z^2} + \frac{z^2}{n_x^2 n_y^2},$$

where  $x, y$  and  $z$  are the projection of the unit wave vector on the principal coordinate system of the crystal.

**Temperature dependence of the refractive indices** When using the refractive indices it has to be kept in mind that they change as a function of temperature. There is various literature [95–97] which experimentally explores the behavior of the biaxial periodically poled Potassium titanyl phosphate (PPKTP) crystals – also used in our setup – at different temperatures. In [95] it is stated that for wavelengths between 500 nm and 1550 nm the refractive indices change according to

$$n(\lambda, T) = n^0 + n_1(\lambda)(T - 25^\circ C) + n_2(\lambda)(T - 25^\circ C)^2 \quad (3.23)$$

with

$$n_{1,2}(\lambda) = \sum_{i=0}^3 \frac{a_i}{\lambda^i}, \quad (3.24)$$

where  $n^0$  is the refractive index at room temperature and the coefficients  $a_i$  are indicated individually for each direction by the values found in [95]. The wavelength  $\lambda$  here is given in micrometers. For wavelengths lower than 550 nm the refractive index mentioned in [98] can be used.

### 3.2.2 Principle of spontaneous parametric down-conversion

Considering equation (3.13) and a plane wave  $E = E_0 \cos(\omega t)$  in a quadratic nonlinear medium such that only the lowest order of non-linearity has to be taken into account, its dielectric response can be written as [92]:

$$\begin{aligned} P(t) &= \epsilon_0 \chi^{(1)} \cos(\omega t) + \frac{1}{2} \epsilon_0 \chi^{(2)} E_0^2 [1 + \cos(2\omega t)] = \\ &= P_L + P_{NL} \end{aligned} \quad (3.25)$$

where additionally to the linear contribution  $P_L$  which is oscillating at the frequency of the incoming light there is the nonlinear contribution  $P_{NL}$  composed of a stationary part and one oscillation at the second harmonic frequency  $2\omega$ . Due to this term a portion of the incoming light is converted to light of doubled frequency, which can be regarded in the photon picture as the creation of one photon out of two incoming photons of half frequency.

Down-conversion can be seen as the inverse of a second harmonic generation process, where one incoming, so called “pump” photon decays into two photons with lower frequencies, which are called “signal” and “idler” photon. Due to energy conservation for the three frequencies

$$\omega_p = \omega_s + \omega_i, \quad (3.26)$$

holds, where  $\omega_{p,s,i}$  refers to the pump, signal and idler frequencies respectively. A second condition is that the momenta of the photons have to be conserved

$$\mathbf{k}_p = \mathbf{k}_i + \mathbf{k}_s, \quad (3.27)$$

where  $\mathbf{k}_m$  are the wave vectors of the waves with frequencies  $\omega_m$ .

These phase-matching conditions can be achieved by using birefringent and anisotropic crystals. In general, there are two types of SPDC processes to be distinguished. In type I the generated photon pair shares a polarization which is orthogonal to the polarization of the pump photon, whereas in type II processes the polarizations of the two generated photons are orthogonal to each other, and one of them shares the pump photon’s polarization. In order to obtain phase matching it is important to note, that the incoming pump photon is polarized in

### 3 Experimental implementation

---

the direction that corresponds to the lower value of the two possible refractive indices [92].

The different possibilities for the polarization of the incoming photon and the two generated ones result in two types of SPDC processes in biaxial crystals for  $n_x < n_y < n_z$  [94]:

Type I	Type II
$n_p^f \omega_p = n_s^s \omega_s + n_i^s \omega_i$	$n_p^f \omega_p = n_s^s \omega_s + n_i^f \omega_i$

To facilitate down-conversion it is also possible to employ a technique called “quasi-phase-matching”. There, a periodically poled material is utilized the structure of which has been fabricated in such a manner that the orientation of one of the crystal axes is inverted periodically along another direction, which can compensate a wave vector miss-match. Quasi-phase-matching can be implemented even when birefringent phase-matching does not work and it can allow for broader phase-matching angles and wavelengths. Additionally, it makes it possible to utilize a larger nonlinear coefficient increasing the efficiency of nonlinear conversion processes. [99]

The phase-matching condition (3.27) then changes to the quasi-phase-matching condition to

$$\mathbf{k}_p = \mathbf{k}_i + \mathbf{k}_s + \frac{2\pi}{\Lambda} \mathbf{a}, \quad (3.28)$$

where  $\Lambda$  is the poling period and  $\mathbf{a}$  is the direction of the poling alteration.

In periodically poled crystals also the poling period alters due to expansion of the material when the temperature changes. The thermal expansion was measured in [95] and was found to approximately parabolically depend on the temperature:

$$\Lambda(T) = \Lambda^0 [1 + \alpha(T - 25^\circ) + \beta(T - 25^\circ)^2], \quad (3.29)$$

where  $\Lambda^0$  is the initial length at room temperature and  $\alpha$  and  $\beta$  are the thermal expansion coefficients also given in [95].

**Phasematching conditions** The phasematching condition (3.28) can be rewritten with  $k_m = |\mathbf{k}_m| = \frac{\omega_m n_m}{c}$  and  $\omega_m = \frac{2\pi c}{\lambda_m}$  in a component wise form as

$$\begin{aligned} \Delta k_x &= \frac{n_p(\lambda_p, T)x_p}{\lambda_p} - \frac{n_i(\lambda_i, T)x_i}{\lambda_i} - \frac{n_s(\lambda_s, T)x_s}{\lambda_s} - \frac{1}{\Lambda(T)} = 0 \\ \Delta k_y &= \frac{n_p(\lambda_p, T)y_p}{\lambda_p} - \frac{n_i(\lambda_i, T)y_i}{\lambda_i} - \frac{n_s(\lambda_s, T)y_s}{\lambda_s} = 0 \\ \Delta k_z &= \frac{n_p(\lambda_p, T)z_p}{\lambda_p} - \frac{n_i(\lambda_i, T)z_i}{\lambda_i} - \frac{n_s(\lambda_s, T)z_s}{\lambda_s} = 0, \end{aligned} \quad (3.30)$$

where  $x_m, y_m$  and  $z_m$  are the projections of the unit wave vector onto the axes of the principal coordinate system of the system, with  $x_m^2 + y_m^2 + z_m^2 = 1$ .

Using this normalization condition and the energy conservation, Eq. (3.30) can be reduced to

$$\begin{aligned}
 |\Delta \mathbf{k}|^2 = & \left( \frac{n_p(\lambda_p, T)x_p}{\lambda_p} - \frac{n_i(\lambda_i, T)x_i}{\lambda_i} - \frac{1}{\Lambda(T)} \right)^2 + \\
 & + \left( \frac{n_p(\lambda_p, T)y_p}{\lambda_p} - \frac{n_i(\lambda_i, T)y_i}{\lambda_i} \right)^2 + \left( \frac{n_p(\lambda_p, T)z_p}{\lambda_p} - \frac{n_i(\lambda_i, T)z_i}{\lambda_i} \right)^2 + \\
 & - n_s(\lambda_s, T)^2 \left( \frac{1}{\lambda_p} - \frac{1}{\lambda_i} \right)^2 = 0.
 \end{aligned} \tag{3.31}$$

where the different refractive indices are still dependent on the directions of the photons via Eq. (3.21). For perfect phase matching Eq. (3.30) as well as Eq. (3.31) must hold since for biaxial crystals Eq. (3.30) does not imply Eq. (3.31). With these equations, being aware of the process type and the central wave vector  $\mathbf{k}_p$ , the spatial distribution of the generated photons can be calculated.

**Gaussian beam and crystal length** In the ideal case with an infinitely long crystal and an infinitely wide pump beam  $|\Delta k| = 0$  and therefore equations (3.30) and (3.31) hold. For a finite crystal length  $L$  and a pump intensity profile of width  $\omega$  downconversion can also occur when  $\Delta k \neq 0$ . In contrast to perfect phase matching, where the interaction Hamiltonian yields a delta function, it produces for imperfect phase matching a weighting function for the intensity of the emitted downconversion:

$$\Phi = e^{-\frac{1}{2}\omega^2(\Delta k_y^2 + \Delta k_z^2)} \text{sinc}^2\left(\frac{1}{2}L\Delta k_x\right). \tag{3.32}$$

Accepting only wavelengths which are weighted by  $\Phi \geq 0.5$  gives a reasonable estimation about the possible wavelength and their spacial distribution emerging from a specific SPDC [94].

### 3.2.3 Spatial analysis of SPDC processes in biaxial crystals

**Coordinate systems** For a more convenient analysis, following [94] two distinct spherical coordinate systems are employed. The propagation direction of the pump beam is best described in spherical coordinates with respect to the crystal axes (see Fig. 3.2), while the signal and idler directions are described with respect to the pump beam

$$\begin{aligned}
 x_p &= \sin(\theta_p) \cos(\varphi_p) \\
 y_p &= \sin(\theta_p) \sin(\varphi_p) \\
 z_p &= \cos(\theta_p),
 \end{aligned} \tag{3.33}$$

### 3 Experimental implementation

$$\begin{pmatrix} x_m \\ y_m \\ z_m \end{pmatrix} = \begin{pmatrix} \cos \theta_p \cos \varphi_p & -\sin \varphi_p & \sin \theta_p \cos \varphi_p \\ \cos \theta_p \sin \varphi_p & \cos \varphi_p & \sin \theta_p \sin \varphi_p \\ -\sin \theta_p & 0 & \cos \theta_p \end{pmatrix} \begin{pmatrix} \sin(\theta_m) \cos(\varphi_m) \\ \sin(\theta_m) \sin(\varphi_m) \\ \cos(\theta_m) \end{pmatrix}, \quad (3.34)$$

where the index  $m$  stands for the signal or idler photon. For a pump momentum parallel to the poling direction  $\varphi_s = \varphi_i + \pi$  holds as  $\mathbf{k}_p$ ,  $\mathbf{k}_s$  and  $\mathbf{k}_i$  must lie in one plane in order to make momentum conservation possible (3.27).

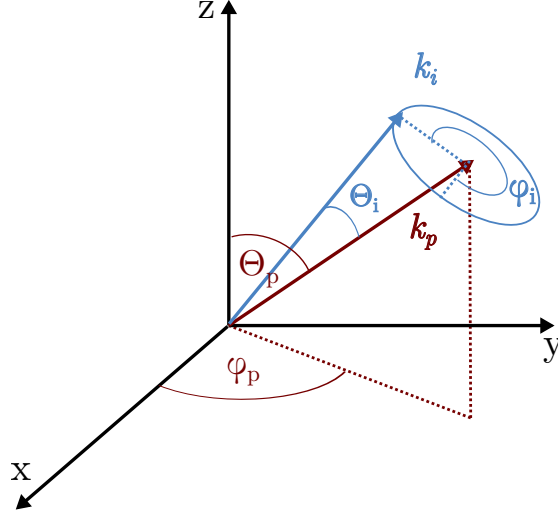


**Figure 3.2:** Illustration of the coordinate systems for a SPDC process. The coordinate angles for the pump photon are defined with respect to the crystal axes, while the signal and idler photon's angles are defined with respect to the  $\mathbf{k}$ -vector of the pump beam.

Please note that only for this section – in order to keep the crystal orientation as usually given in literature – the direction of the maximal refractive index is the  $z$ -direction, pointing upwards. In the rest of the thesis, the  $z$ -direction will be the propagation direction of the beam, while  $y$  is pointing upwards.

#### Simulation of the spatial distribution of a SPDC process in a PPKTP

In order to solve Eq. (3.30) and Eq. (3.31) and find phasematched photons we consider the possible configurations for  $\lambda_i$ ,  $\varphi_i$ ,  $\varphi_s$ ,  $\theta_i$  and  $\theta_s$ . After finding a matching wavelength at a set of matching angles via  $|\Delta k| = 0$  (3.31), the weighting function (3.32) is considered at exactly this wavelength and angles.

In a collinear process, which is treated first, the signal and idler photon emerge in the same direction  $\mathbf{k}_s/|\mathbf{k}_s| = \mathbf{k}_i/|\mathbf{k}_i|$ . Since our setup is dependent on the collinearity of the downconversion, the PPKTP crystal of 25 mm length is manufactured with a periodic poling of  $\Lambda = 10 \mu\text{m}$  in  $x$ -direction such that collinear photon pairs in  $x$ -direction are primarily produced. Under these conditions it is interesting to investigate at which temperature  $T$  a degenerate photon pair is created. This can be done by finding a solution for the idler wavelength  $\lambda_i$  in Eq. (3.31) with fixed angles  $\theta_p = \pi/2$  and  $\theta_i = \theta_s = 0$  and  $\varphi_p = \varphi_i = \varphi_s - \pi = 0$  when varying the temperature. In Fig. 3.3 the collinear wavelength dependence

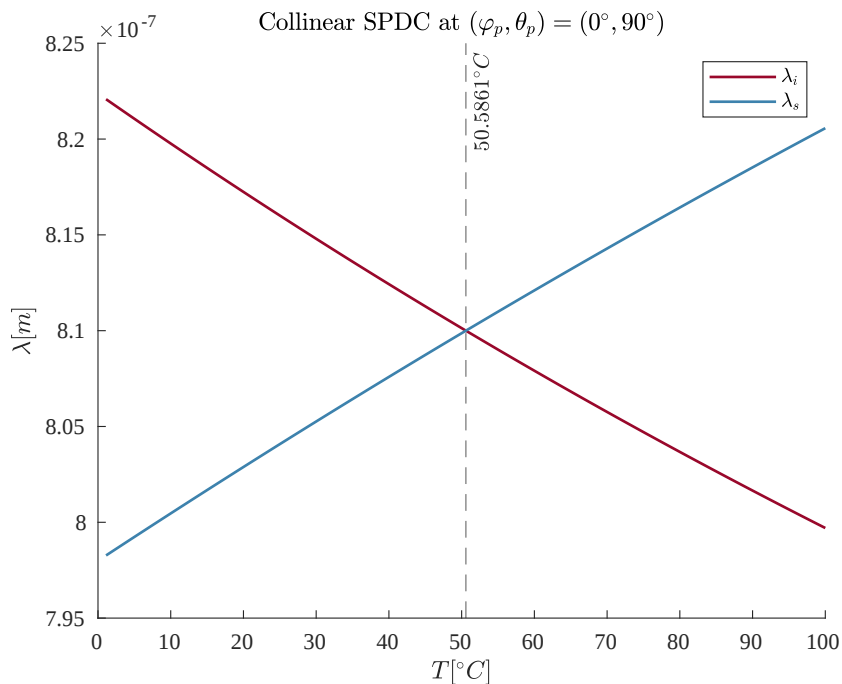


**Figure 3.3:** Theoretical calculation of the wavelength of a collinear SPDC photon pair for a straight pump beam as a function of temperature.

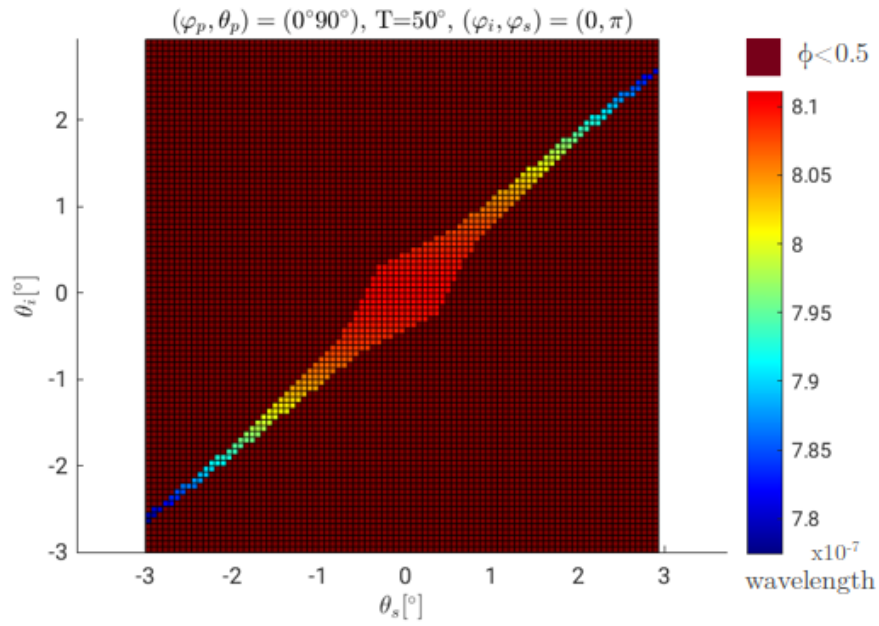
on the temperature is shown, where one can see that the collinear creation of a degenerate pair happens at  $\sim 50^\circ C$  as specified by the manufacturer.

Next, the spectral and spatial distribution at a fixed temperature has to be considered. For a fixed polar angle  $\varphi_i$  and a pump entering in  $x$ -direction the solution space of possible idler wavelength at variation of  $\theta_i$  and  $\theta_s$  can be seen in Fig. 3.4. The dark red parts here are combinations of signal and idler angles, where either energy is not conserved or the weighting function (3.32) gets too small. We can see that the signal and idler angles are correlated, especially for larger angles, where there exist only phase matched photon pairs, when both, signal and idler photon, emerge at the same opening angle  $\theta$ . For angles close to  $0^\circ$ , i.e. close to the pump beam and the poling direction, there is more deviation of direction of the two emerging photons possible. For smaller possible angles it can be seen that the minimum possible idler wavelength for  $\theta_i, \theta_s \in [-1^\circ, 1^\circ]$  is about 806 nm.

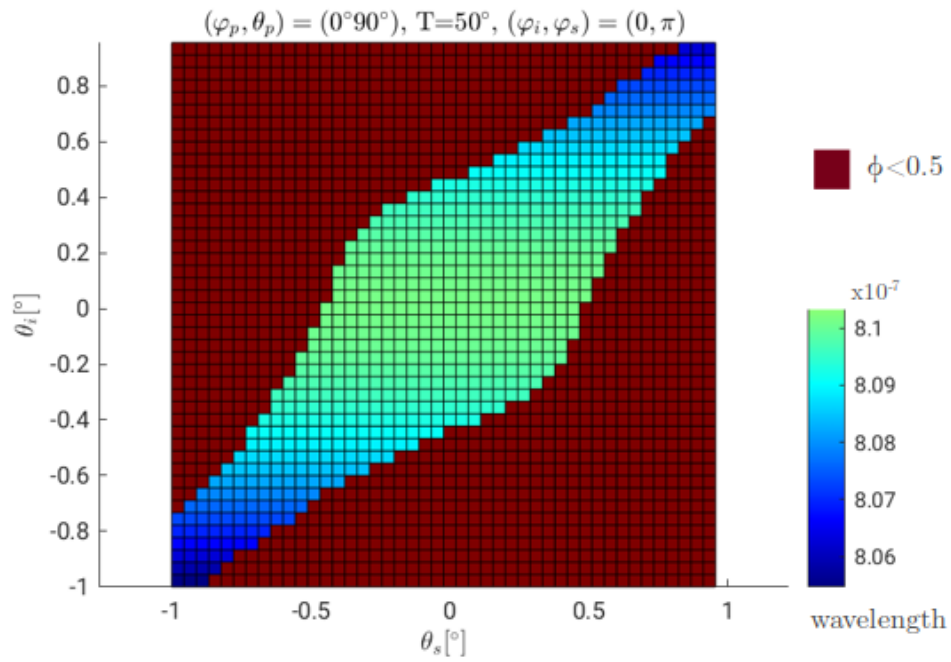
The spatial distribution for degenerated signal and idler photons  $\lambda_{s,i} = 810 \pm 0.2$  nm is shown in Fig. 3.5. Since the simulation checks, if for a given set of idler angles, there exists a solution for a signal configuration, for redder points the partner photon is more widely spread. Considering deviating wavelength like  $\lambda_i = 808 \pm 0.2$  nm and  $\lambda_s = 812 \pm 0.2$  nm, it can be seen that the photons do not emerge parallel to the pump anymore but within a ring around it (Fig. 3.6).

**Alteration of the pump direction** For a pump wavevector not entering normal to the crystal axes anymore the calculation becomes even more complicated, as now  $\varphi_i$  and  $\varphi_s$  are not connected anymore, because the pump wavevector is

### 3 Experimental implementation



(a)  $\theta_{i,s} \in (-5^\circ, 5^\circ)$



(b)  $\theta_{i,s} \in (-1^\circ, 1^\circ)$

**Figure 3.4:** Wavelength of the idler photon dependent on the azimuthal angles  $\theta_{i,s}$  at fixed temperature  $T = 50^\circ$

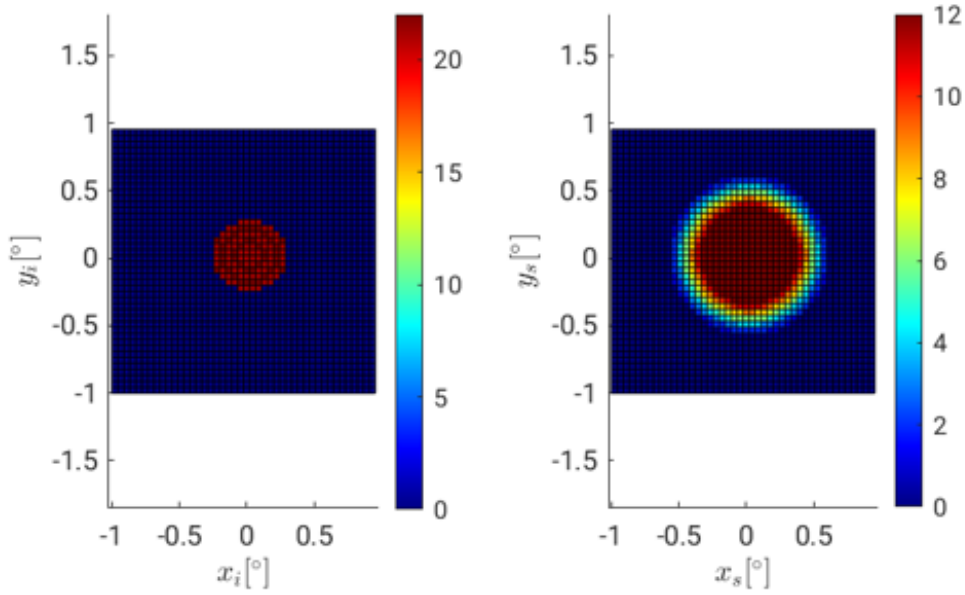


**Figure 3.5:** Spatial emission of signal and idler photons at  $\lambda_{s,i} = 810 \pm 0.2$  nm, for  $(\varphi_p, \theta_p) = (0^\circ, 90^\circ)$ ,  $T = 50^\circ$ ,  $x_m = \theta_m \cos \varphi_m$ ,  $y_m = \theta_m \sin \varphi_m$

no longer parallel to the poling period and hence the four vectors in Eq. (3.28) do not necessarily have to lie in one plane. Still it is of interest to know at which temperature degenerated photons are emerging parallel to the pump. It can be shown that the temperature needed for collinearly emerging photons parallel to the pump beam at a tilted pump beam decreases until  $45^\circ C$  for an increasing  $\theta_p$  until there is no solution anymore for  $\theta_p > 1.9^\circ$ . The temperature dependence of collinearly emerging photons parallel to the pump at a pump tilted by  $1.8^\circ$  can be seen in Fig. 3.7.

Hence, the temperature for a tilted crystal can be adjusted such that degenerate photon pairs are still produced collinearly. Nevertheless, this won't leave the spatial distribution and the efficiency unaltered. The maximum intensity will be at a position, where momentum conservation holds and the weighting function is 1 (3.32). This is why in this case the possible emission angles of one wavelength are not distributed symmetrically around the pump wavevector anymore, but one side is more likely than the other.

Furthermore, it has to be kept in mind, that all calculated angles will change when the photons diffract at the crystal surface when exiting the PPKTP. Here the idler and signal photon experience a different refraction angle because they are perpendicularly polarized. Hence photons not exiting normal to the crystal surface are separated even if they emerged collinearly.

### 3 Experimental implementation

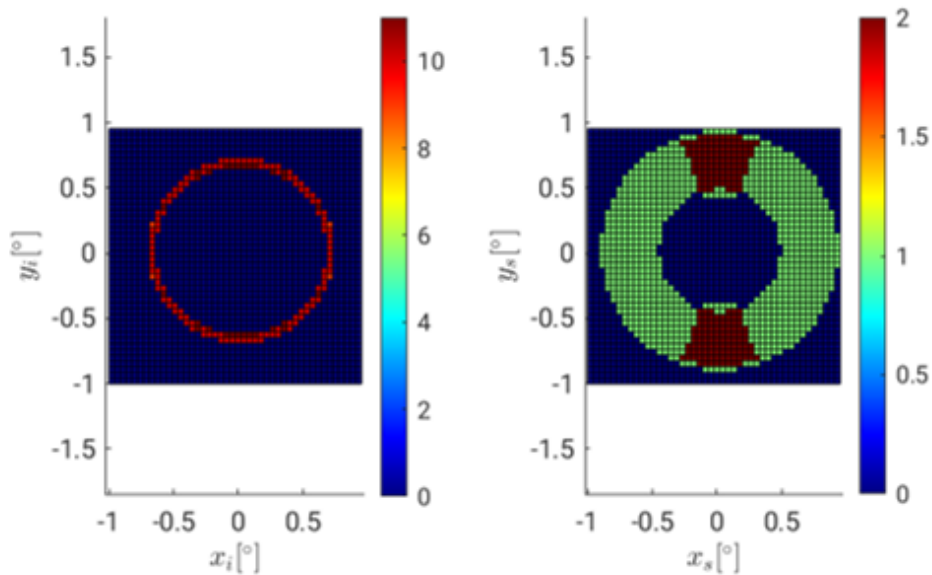


**Figure 3.6:** Spatial emission of signal and idler photons at  $\lambda_i = 808 \pm 0.2$  nm and  $\lambda_s = 812 \pm 0.2$  nm, for  $(\varphi_p, \theta_p) = (0^\circ, 90^\circ)$ ,  $T = 50^\circ$ ,  $x_m = \theta_m \cos \varphi_m$ ,  $y_m = \theta_m \sin \varphi_m$

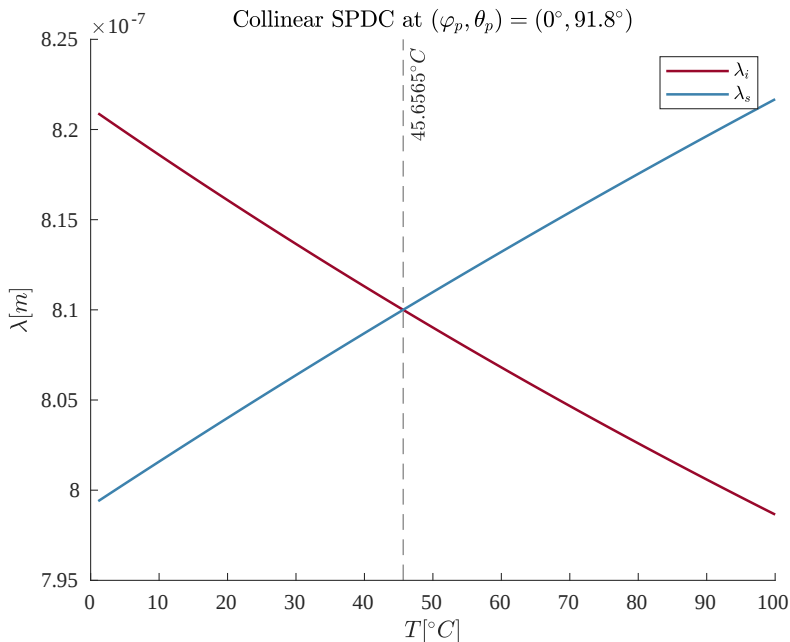


**Figure 3.7:** Theoretical calculation of the wavelength of a collinear SPDC photon pair parallel to the pump wavevector for a tilted pump beam  $\theta_p = 91.8^\circ$  as a function of temperature. Degenerated photon pairs in this direction are produced at about  $45.7^\circ$ .

### 3.3 Experimental setup

In order to realize the observation of Bohmian trajectories via weak measurement and the delayed choice measurement of the which-way information, three principle parts of the setup are required (see Fig. 3.3). First of all there is the source, creating pairs of entangled photons. One photon of a pair is then sent to a polarization measurement unit. The polarization measurement can be performed at any time independently of the other photons position in the slit system, which enables to switch between the different measurement scenarios explained in section 2.2.2. The other photon is meanwhile sent to the double slit, where the trajectories are observed via weak measurement as explained in section 2.3.1.

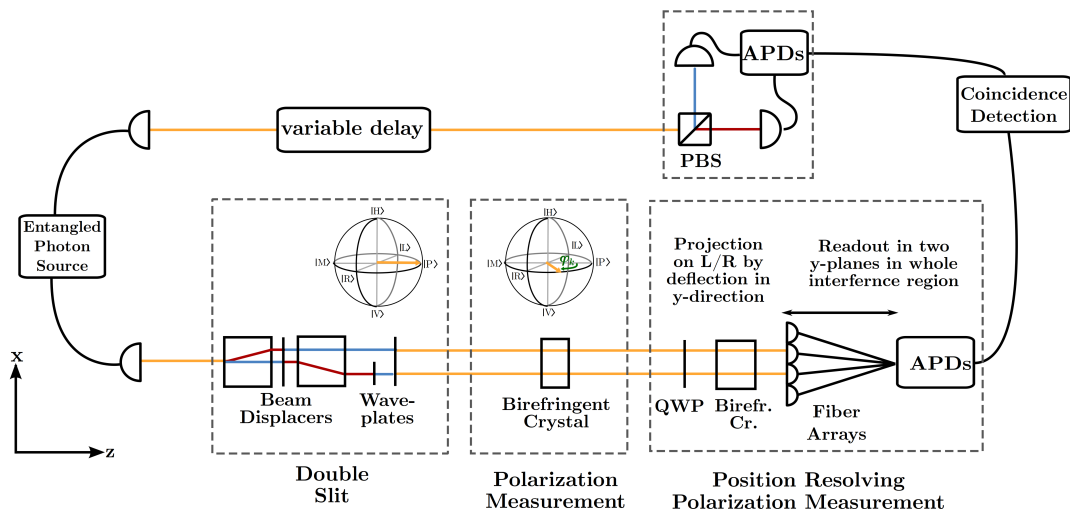


**Figure 3.8:** Complete experiment setup: Photon 1 of an entangled photon pair is sent to the double slit and is weakly measured in the interference region while a polarization measurement is performed at arbitrary time on photon 2.

Since the experimental work linked to this thesis was mostly focused on the creation of the entangled photon source, the source will be explained and analyzed in great detail, while the other parts of the setup are explained only conceptually.

#### 3.3.1 Double slit setup

The double slit itself is composed of two birefringent Yttriumvanadat crystals ( $\text{YVO}_4$ ), also called YVO, which are adjusted such that that  $H$ -polarized light experiences the extraordinary refractive index of the crystal and is hence diffracted with respect to  $V$ -polarized light. This is achieved by aligning the optical axis of both YVOs in the horizontal plane at an angle of approximately  $45^\circ$  with respect to the propagation direction of the beam but orthogonally to each other, such that the two crystals both deflect  $H$  but into opposite directions. After the first YVO separated the incoming light into two beams of  $H$ - and  $V$ -polarization, the polarization of the two is flipped by a HWP and the new  $H$ -beam is redirected

### 3 Experimental implementation

---

then by the second YVO into the other direction. The sum over the two deflections then defines the separation of the slits. The fact that both beams were deviated ensures that both wavepackets propagate the same optical path and are therefore still able to interfere. They are then passing through a parted waveplate, which only swaps the polarization of one slit side while the other one remains unchanged, such that afterwards both slit sides are vertically polarized, allowing interference. This setup has the advantage that not only a small part of the incident light reaches the interference region, since, in contrast to the double slit experiments usually considered, no light is absorbed by the mask defining the two slits.

#### 3.3.2 Weak measurement implementation

For the experimental implementation of the weak measurement we weakly couple the photon's momentum with its polarization and postselect on the position, as it was already done before [6, 7]. This enables us to observe the average photon trajectories, where no further measurement apparatus is needed as the photon itself encodes the pointer in its polarization [20].

For this first the polarization of the two beams is again changed via a QWP rotating the  $V$ -states into  $P$ -polarized ones. Second, the weak measurement is implemented by another YVO, which separates  $H$  and  $V$  polarization and therefore couples the transverse momentum of the photon  $\hat{p}_x$  (system observable) to the polarization in the  $H/V$ -basis (pointer variable) via the interaction Hamiltonian  $\hat{H} = \epsilon \hat{p}_x \otimes \hat{\sigma}_z$ . The weak interaction strength  $\epsilon$  is given by the thickness of the YVO and the tilt of the crystal relative to the propagation direction as they define the separation of the  $H$ - and  $V$ -polarized light after the crystal.

Performing the weak measurement on an initial system pointer pair  $|\Psi\rangle = |\psi_S\rangle \otimes |P\rangle$  and then postselecting on a certain position  $q$  yields for small interaction strength  $\epsilon \ll 1$  as in Eq. (1.51)

$$\begin{aligned} |\Phi_M^F\rangle &= \langle q | e^{-\frac{i}{\hbar} \epsilon \hat{p}_x \otimes \hat{\sigma}_z} | \psi_S \rangle | P \rangle \\ &= \frac{1}{\sqrt{2}} (e^{-\frac{i}{\hbar} \epsilon p_w} | H \rangle + e^{\frac{i}{\hbar} \epsilon p_w} | V \rangle) \\ &\propto \frac{1}{\sqrt{2}} (| H \rangle + \frac{2i}{\hbar} \epsilon p_w | V \rangle), \end{aligned} \tag{3.35}$$

where  $p_w = \frac{\langle q | \hat{p}_x | \psi \rangle}{\langle q | \psi \rangle}$  is the weak value of the transverse momentum expressing the transverse Bohmian velocity via  $v_{Bx}(q) = \text{Re}[p_w]/m$  (see Eq. (2.3.1)). This means that the polarization of photons arriving at a certain position is rotated by a phase  $\varphi_x$  in the  $xy$ -plane of the Bloch sphere (see Fig. 3.8) proportional to the weak value and the interaction strength  $\varphi_x \propto \epsilon p_w$ . The weak value can then be read off via the measurement of the expectation value of conjugate pointer variable  $\hat{\sigma}_y$ . This measurement is implemented by another QWP at  $45^\circ$ , which does not change the  $P$  component of the state but rotates  $|R/L\rangle$  to  $|H/V\rangle$ , and another YVO which now again separates  $H$  and  $V$ . The two together therefore

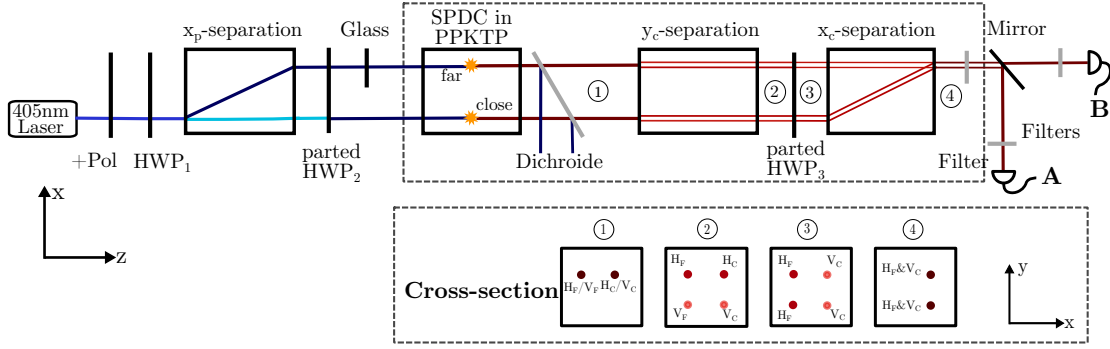


**Figure 3.9:** Entangled photon source as seen from above. Double lines stand for a lower and an upper beam.

don't deflect right handed light while left handed light is redirected downwards so that the at a given position  $q$  a single photon detector – in our case an avalanche photo diode (APD) – detects the number of arriving  $R$ -polarized photons  $I_R$  while another APD directly underneath the number of  $L$ -polarized photons  $I_L$ . The expectation value of  $\hat{\sigma}_y$  is then given by

$$\langle \hat{\sigma}_y \rangle = \frac{I_R - I_L}{I_R + I_L}. \quad (3.36)$$

As the initial pointer state had an expectation value of  $\langle P | \hat{\sigma}_y | P \rangle = 0$ , the transverse Bohmian momentum is given via Eq. (1.54) by

$$k_x = \text{Re}[p_w] = \frac{1}{\epsilon} \left[ \frac{I_R - I_L}{I_R + I_L} \right]. \quad (3.37)$$

These measurements are performed in the interference region by a fiber array connected to  $2 \times 10$  APDs movable in  $x$ - and  $z$ -direction allowing us to scan the whole space. This possibility of performing postselections on every position in the interference region makes possible to observe the Bohmian velocity at any point and enables a reconstruction of the average Bohmian trajectories.

### 3.3.3 Entangled photon source setup

Since a high number of photons is needed in order to reconstruct the Bohmian photon trajectories, a source producing entangled photon pairs at high photon rate is needed. For this we adapt the source of Evans et al. [100].

**Main setup** In order to obtain the maximally entangled Bell-state  $|\psi\rangle = \frac{1}{\sqrt{2}}(|H\rangle|H\rangle + |V\rangle|V\rangle)$  two photons are created via SPDC at two sites in a PPKTP crystal and are then redirected by a set of birefringent crystals (calcites), such that their point of creation becomes indistinguishable. The exact setup can be seen in Fig. 3.9. Plus polarized laserlight of 405nm wavelength  $|P\rangle = \frac{1}{\sqrt{2}}(|H\rangle + |V\rangle)$  is sent onto a halfwaveplate ( $HWP_1$ ) in order to be able to

### 3 Experimental implementation

---

manipulate the amplitudes of the  $H$ - and  $V$ -polarized parts later on, such that the resulting state is

$$|\psi_i\rangle = a|V\rangle + b|H\rangle, \quad (3.38)$$

where  $|a|^2 + |b|^2 = 1$  and  $a, b \in \mathbb{R}$ .

The light then traverses the first birefringent calcite crystal ( $x_P$ -crystal) where the horizontally polarized part is redirected in the  $x$ -direction by 4.16 cm (Eq. (3.20)), such that there are now two beams, denoted with the indices  $C$  and  $F$  for close (right hand side in propagation direction) and far (left hand side in propagation direction). The difference in the distance traveled results in a path and phase difference  $\varphi_1$  between  $|H\rangle$  and  $|V\rangle$

$$|\psi_F\rangle = |H\rangle, \quad |\psi_C\rangle = |V\rangle. \quad (3.39)$$

The following  $\text{HWP}_2$  is parted such that only the far beam is affected by the  $45^\circ$ -HWP, which flips  $H$  to  $V$ , whereas the close beam is only traversing a glass, such that no phase difference is emerging. The two states then read

$$|\psi_F\rangle = |V\rangle, \quad |\psi_C\rangle = |V\rangle, \quad (3.40)$$

which is important, because only vertically polarized light will be down converted in the PPKTP (see section 3.2.2). At each site two 810nm photons are created out of one 405nm  $V$ -polarized photon via collinear SPDC type II (see section 3.2.2), one horizontally and one vertically polarized:

$$|\psi_F\rangle = |V_F\rangle \otimes |H_F\rangle, \quad |\psi_C\rangle = |V_C\rangle \otimes |H_C\rangle. \quad (3.41)$$

Light of the pump laser which did not undergo downconversion is reflected out of the path of the photon pairs by a dichroide. The photon pairs are then redirected in the  $y$ -direction to a lower ( $l$ ) and a upper ( $u$ ) photon by the  $y_c$ -crystal, such that the four spatial positions correspond to polarization states as follows (see second picture in the cross section shown in Fig. 3.9)

$$\begin{aligned} |\psi_{Fu}\rangle &= |H_F\rangle, & |\psi_{Cu}\rangle &= |H_C\rangle, \\ |\psi_{Fl}\rangle &= |V_F\rangle, & |\psi_{Cl}\rangle &= |V_C\rangle. \end{aligned}$$

The four of them then traverse another retarder combination where there is a  $45^\circ$ -HWP in the far upper and close lower beams while a  $0^\circ$ -HWP is in the others (see third picture in the cross section shown in Fig. 3.9). The resulting states are

$$\begin{aligned} |\psi_{Fu}\rangle &= |V_F\rangle, & |\psi_{Cu}\rangle &= |H_C\rangle, \\ |\psi_{Fl}\rangle &= |V_F\rangle, & |\psi_{Cl}\rangle &= |H_C\rangle, \end{aligned}$$

where now it is important to see that both  $V$ -polarized photons come from the far SPDC site, while the  $H$ -polarized ones emerge from the other site. The lower and upper beams are then brought back together via a third birefringent calcite crystal ( $x_c$ -crystal) which redirects the close  $H$ -polarized beam onto the far  $V$ -polarized one, causing another path difference and phase  $\varphi_2$ . The single photon

detectors to which the upper and lower beam are sent, after having traversed a set of exchangeable filters and the lower beam being redirected by a mirror, then indistinguishably observe either both a horizontally polarized photon from the close SPDC site with intensity proportional to the amplitude of the light shining in to the close side, hence  $\propto |a|^2$ , and phase  $\varphi_2$  or a vertically polarized one from the far SPDC site with intensity  $\propto |b|^2$  and phase  $\varphi_1$ , which results in a final state

$$|\psi\rangle = a|HH\rangle + be^{i\varphi}|VV\rangle, \quad (3.42)$$

with  $\varphi = \varphi_1 - \varphi_2$  is the phase difference between the close and far beam. As we can see, the arrangement is such that the close as well as the far beam travel once the longer way in the two crystals in order to not reduce the coherence of the photons when they arrive at the detectors. Nevertheless, we have to keep this phase and path length differences in mind for a later search for errors.

Eliminating the phases in between the two components from two downconversion sites and detecting equally photons from both sites by adjusting the amplitudes  $a$  and  $b$  to compensate for different coupling efficiencies then results in the desired Bell state

$$|\psi\rangle = \frac{1}{\sqrt{2}}(|HH\rangle + |VV\rangle). \quad (3.43)$$

The photons coupled into single mode fibers are sent to the tomography stage, where their state is analyzed, such that the lower beam corresponds to coupler and arm A of the tomography while the upper one corresponds to B.

**Polarization compensation** Due to random stress and imperfections in the singlemode fibers, it must be taken into account that the polarization of each arm is rotated by each fiber by a random unitary transformation  $\hat{U}$ , e.g.

$$\hat{U} = \begin{pmatrix} \cos(\alpha) & e^{i\theta} \sin(\alpha) \\ \sin(\alpha) & -e^{i\theta} \cos(\alpha) \end{pmatrix}. \quad (3.44)$$

Therefore the uncompensated state arriving at the tomography is

$$\begin{aligned} |\psi'\rangle &= (\hat{U}_1 \otimes \hat{U}_2) \frac{1}{\sqrt{2}}(|HH\rangle + |VV\rangle) \\ &= \frac{1}{\sqrt{2}}[(c_1c_2 + s_1s_2)(|HH\rangle + e^{i(\theta_1+\theta_2)}|VV\rangle) + \\ &\quad + (c_1s_2 - s_1c_2)(e^{i\theta_2}|HV\rangle - e^{i\theta_1}|VH\rangle)], \end{aligned} \quad (3.45)$$

where  $c_i = \cos(\alpha_i)$  and  $s_i = \sin(\alpha_i)$  and which is not correlated in the  $H/V$ -basis as required for the trajectory experiment anymore. The entanglement can be recuperated by adjusting the unitary transformations such, that the polarization of each photon is rotated by the same angle  $\alpha_1 = \alpha_2 = \frac{n\pi}{2}$  in each fiber. This can be realized by using manual polarization controllers (so called 'bat-ears') for each fiber, which coil the fiber and thereby induce stress, which in turn leads to

### 3 Experimental implementation

---

birefringence. The birefringence introduces a retardation between different polarization components of the wave, such that three coils in a row and the adjustment of stress can generate any desired polarization state from any arbitrary input polarization [101].

It is a common procedure to adjust the fibers such that they only conserve two states of a linear polarization basis and hence control the angles  $\alpha_i$  and compensate the remaining phase difference with an additional device (see section 3.3.3). For the adjustment a  $H$ -polarizer is inserted into the source directly in front of one of the couplers where the photons are fed into the fibers, and the bat-ears are adjusted in such a manner that all photons in this arm are detected to be  $H$ -polarized by the tomography, when measuring  $\hat{\sigma}_z$ . Applying this procedure and then blocking one SPDC-site in the source, we saw that not all photon pairs were detected to be  $HH$ - or  $VV$ -polarized, according to the blocked site, but around 3% of the photons from the A-arm were detected also  $VH$  or  $HV$  respectively, even though the fibers did not rotate the state anymore. This can only be explained by the mirror which redirects the photons in arm A onto the coupler. If the mirror is rotating the beam not only around a vertical axis, but also around a horizontal one, the eigenstates of the polarization are not  $H$  and  $V$  anymore but rotated by another unitary. This can easily be undone by adjusting the bat-ears such, that when blocking one SPDC site all photon coincidences are detected to be  $HH$  or  $VV$ , according to the blocked site, as it is only important that the state after the fibers in the tomography or the double slit has the correct polarization correlation.

**Phase compensation** Any difference in optical path length as well as the fiber connection to the tomography and the double slit establishes a phase between the components emerging from the two SPDC sites. One way to eliminate the phase is to benefit from the birefringent properties of two  $YVO_4$  crystals. Applied behind each other with one optical axis in horizontal, one in vertical direction and tilted in opposite directions the first YVO (horizontal optical axis) induces a phase shift between  $H$  and  $V$  corresponding to the angle dependent extraordinary refractive index  $n_e(\alpha)$  (see Eq. (3.16)), while the second one refracts only via Snell's law counteracting the separation between the beams by the first YVO and hence preserving spatial coherence.

Since it is the same to introduce a phase between the components of SPDC of the state as between the two polarizations in one arm, another way to eliminate the phase is to introduce a thin glass plate of thickness  $d_G$  and refractive index  $n_G$  plate into one of the arms (see Fig. 3.9), such that one photon travels a longer optical path  $\xi = n \cdot d_G$  due to a greater optical index of the glass plate (coherence will be regarded later in section 4.3). The effective thickness of the glass plate can be adjusted by rotating it and therefore achieving a thickness dependent of the rotation angle  $\beta$ . The resulting optical pathlength difference then reads

$$\Delta\xi = \frac{(n_0 - n_G) \cdot d_G}{\cos(\beta)}, \quad (3.46)$$

where  $n_0 \approx 1$  is the refractive index of air. The introduced phase is then given by  $\Delta\varphi = \frac{2\pi\Delta\xi}{\lambda}$ .

Obviously, for the pure phase compensation it is easier to only employ the YVO system as it is independent of the source setup and can be used either in the tomography or the double slit. Nevertheless, the glass plate will be needed later in order to increase coherence (section 4.3) and hence its phase compensation is also to be considered.

#### 3.3.4 Tomography and Coincidence Detection

**Tomography** The generated photon state is analyzed by the tomography setup. Here a measurement of  $\hat{\sigma}_x$ ,  $\hat{\sigma}_y$ , and  $\hat{\sigma}_z$  can be performed on each photon of the pair at the same time (Fig. 3.10). A combination of an HWP, a QWP and a polarizing beamsplitter realizes the measurement in the three direction by appropriate settings of the waveplates.

	QWP	HWP
$\hat{\sigma}_x$	0°	22.5°
$\hat{\sigma}_y$	45°	22.5°
$\hat{\sigma}_z$	0°	0°

With these settings the positive eigenvector of the measurement is rotated into  $|H\rangle$  and the negative into  $|V\rangle$  such that the PBS, which splits incoming light into its horizontal and vertical component, is projecting on the positive or negative eigenvalue of the chosen measurement direction.

Measuring all combinations of  $\hat{\sigma}_i \otimes \hat{\sigma}_j$  on the photon pair, enables a complete scan of the state and a full reconstruction of the density matrix via Eq. (1.23)

$$\hat{\rho} = \sum_{i,j} \frac{E_{ij} \hat{\sigma}_i \otimes \hat{\sigma}_j}{4}, \quad i, j = 0, 1, 2, 3 \quad (3.47)$$

where  $E_{ij}$  is the expectation value of the measurement of  $\hat{\sigma}_i \otimes \hat{\sigma}_j$  and  $\{\hat{\sigma}_0, \hat{\sigma}_1, \hat{\sigma}_2, \hat{\sigma}_3\} = \{\mathbb{1}, \hat{\sigma}_x, \hat{\sigma}_y, \hat{\sigma}_z\}$ .

In order to correctly reconstruct the density matrix of the entangled photon state which will be later used for the observation of the Bohmian trajectories and the polarization measurements, it is necessary to pay attention to the coupling efficiencies for measurements in different bases. Firstly, due to the rotation of the waveplates it is possible that the coupling improves or decreases at the different ports of the PBS for measurements in different bases. Hence, the detected number  $\tilde{N}_{ij}$  of pairs, where the first photon arrives at  $i$  (e.g the  $H$ -port for  $\hat{\sigma}_z$  measurement on the first photon in arm A) while the second one arrives at the  $j$ -port, is governed by the detection efficiency  $\eta_{ij}$  via

$$\tilde{N}_{ij} = \eta_{ij} \cdot N_{ij}, \quad i, j \in \{H, V, P, M, L, R\}, \quad (3.48)$$

with  $N_{ij}$  being the actual number of coincidences of ports  $i$  and  $j$ . The relative coupling efficiency can be easily determined by sending only polarized light into

### 3 Experimental implementation

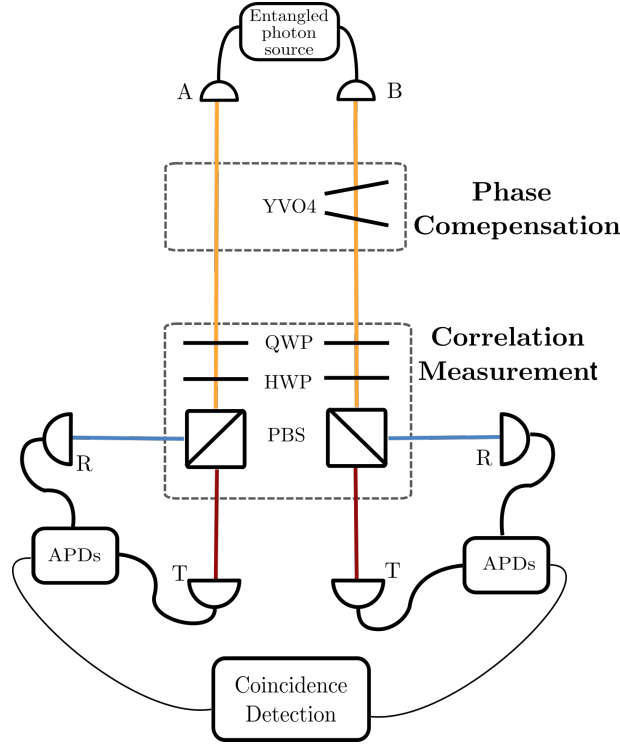


**Figure 3.10:** Illustration of the tomography setup

the two arms of the tomography such that at a specific choice of measurement basis in an arm, an equal amount of light should be collected by the two couplers behind the PBS. Thus, for  $\hat{\sigma}_z$  a polarizer of one of the other directions  $y$  or  $x$ , e.g a  $P$ -polarizer, is needed in front of the corresponding coupler in the source. The difference in the distribution of the detected coincidences from  $\frac{1}{4} : \frac{1}{4} : \frac{1}{4} : \frac{1}{4}$  in the four ports then determines the efficiencies for the four ports in the chosen basis.

A density matrix reconstruction based on the measured expectation values of all  $\hat{\sigma}_i \otimes \hat{\sigma}_j$  via Eq. (3.47) can lead to not physical reconstructed states, where the density matrix does not fulfill the conditions of a density matrix explained in section 1.1, as the reconstruction is limited by the experimental issues like losses, noise or the coupling efficiencies. A method to find the closest physical state to the measured data is to perform a maximum likelihood estimation from standard statistics. For this the algorithm of Shang et al. [102] is used.

Before performing a complete tomography it is useful to have a look at the correlations in  $xx$ -,  $yy$ - and  $zz$ -directions, the expectation values of  $\hat{\sigma}_i \otimes \hat{\sigma}_i$  in all three bases read off from the outcomes at the transmission (T) and reflection (R) ports of the PBSs of the tomography setup

$$\kappa = \frac{N_{RR} + N_{TT} - N_{RT} - N_{TR}}{N_{total}}, \quad (3.49)$$

where  $N_{tot}$  is the total number of coincidences and  $R \in \{V, M, L\}$  and  $T \in \{H, P, R\}$ . For the desired state (3.43) the outcomes here should be

$$\kappa_{xx} = 1, \quad \kappa_{yy} = -1, \quad \kappa_{zz} = 1. \quad (3.50)$$

The uncompensated state (3.42) reads in the three bases

$$\begin{aligned} |\psi\rangle &= a|HH\rangle + be^{i\varphi}|VV\rangle = \\ &= (a + be^{i\varphi})(|MM\rangle + |PP\rangle) + (a - be^{i\varphi})(|PM\rangle + |MP\rangle) \\ &= (a - be^{i\varphi})(|LL\rangle + |RR\rangle) + (a + be^{i\varphi})(|RL\rangle + |LR\rangle). \end{aligned} \quad (3.51)$$

with  $|a|^2 + |b|^2 = 1$  and  $a, b \in \mathbb{R}$ . This yields to correlations in the three different bases of

$$\kappa_{xx} = 2ab \cos(\varphi), \quad \kappa_{yy} = -2ab \cos(\varphi), \quad \kappa_{zz} = 1. \quad (3.52)$$

For  $a = b = \frac{1}{\sqrt{2}}$  and  $\varphi = 2\pi n$  with  $n \in \mathbb{Z}$  this results in the desired correlations.

These three correlations let us estimate the proximity to the desired entangled state. The fidelity, a measure of distance between two arbitrary quantum states  $\hat{\rho}_1$  and  $\hat{\rho}_2$   $\mathcal{F} = \text{tr}(\sqrt{\sqrt{\hat{\rho}_1}\hat{\rho}_2\sqrt{\hat{\rho}_1}})$  simplifies for  $\hat{\rho}_1$  being pure to [10]

$$\mathcal{F}(|\psi\rangle, \hat{\rho}) = \sqrt{\langle \psi | \hat{\rho} | \psi \rangle}. \quad (3.53)$$

Since for the Bell states the non diagonal correlations are all zero, the density matrix of the created state is  $\hat{\rho} = \frac{1}{2}(\mathbb{1} + \kappa_{xx}\hat{\sigma}_{xx} + \kappa_{yy}\hat{\sigma}_{yy} + \kappa_{zz}\hat{\sigma}_{zz})$  and the fidelity simplifies to

$$\mathcal{F} = \frac{1}{2}\sqrt{1 + \kappa_{xx} - \kappa_{yy} + \kappa_{zz}}. \quad (3.54)$$

**Coincidence detection** Only photon pairs which are generated coherently in the SPDC process result in the entangled state which is necessary in order to perform the trajectory measurement later in the experiment. In order to know exactly which incoming photons belong to a pair a coincidence unit is needed. This unit, designed and implemented by Lukas Knips, receives electrical pulses from the APDs to which the photons are sent, and then identifies those as a pair whose both signal starts within a clock cycle of certain length in time.

The coincidence detection unit is configured to record the four channels of singles from each of the four ports the photons reached via transmission or reflection at each side, as well as four coincidence channels providing the number of photon pairs whose singles arrived together in between a certain time interval at the detectors. From a purely statistical point of view, when  $s_1$  singles are detected in one channel in a time interval  $t_1$  and  $s_2$  singles in another channel in a time interval  $t_2$  then, without having an actual photon pair originating from the SPDC process, the number of detected accidental coincidence counts is given by

$$\zeta_{1,2} = \frac{s_1}{t_1} \cdot \frac{s_2}{t_2} \cdot t_C \cdot t_M \stackrel{t_M=t_1=t_2}{=} \frac{s_1 \cdot s_2 \cdot t_C}{t_M} \quad (3.55)$$

### 3 Experimental implementation

---

in a time interval  $t_M$  with a coincidence interval set to  $t_C$ . This causes a loss of correlation because the accidentals wash out the contrast between the coincidences the Bell state has and those it does not have. For approximately equally distributed singles, the accidentals are also approximately the same in each channel  $\zeta$  and the correlation decreases

$$\begin{aligned} \kappa^{acc} &= \frac{(N_{RR} + \zeta) + (N_{TT} + \zeta) - (N_{RT} + \zeta) - (N_{TR} + \zeta)}{N_{total} + 4\zeta} \\ &= \frac{N_{RR} + N_{TT} - N_{RT} - N_{TR}}{N_{total} + 4\zeta} \end{aligned} \quad (3.56)$$

Therefore, it is purposeful to decrease the number of accidentals by reducing the coincidence time interval, which was finally set to 4 ns.

## 4 Alignment of the photon source

In order to setup the source a proper alignment of all the optical components, especially the four birefringent crystals, is necessary. For this two laser beams are used. One is the pump laser, which travels from left to right in Fig. 3.9 with pump wavelength  $\lambda_p = 405$  nm, from now on called the “pump beam”. Since it is not possible to observe the position of the single photons generated in the SPDC process, laser light of the wavelength of the collected photons  $\lambda_c = 810$  nm is sent backwards through the collection optics to make alignment possible. This beam, travelling backwards in the setup is from now on called the “collection beam”. The goal of the alignment lies in the adjustment of the couplers and crystals in such a manner that the four components of the collection beam perfectly overlap with the two parts of the pump beam in the center of the PPKTP, all six of them having their focus at that point.

### 4.1 Beam focus alignment

Since the average photon numbers in the signal and idler mode are proportional to the intensity of the pump field, focusing the beam into the center of the PPKTP will increase the number of photon pairs [92]. Hence, the foci of the pump beams as well as the ones of the collection beams have to be measured and adjusted very precisely, such that the PPKTP can be centered onto the average focus position.

For the measurement of the beam profile a CCD camera is used, taking images of the beams at various  $z$ -positions. The beam parameters from Eq. (3.6) can then be determined by the extraction of the standard deviation of the intensity profile which provides the beam radii in  $x$ - and  $y$ -direction. Then the beam parameters  $M_{x,y}^2$ ,  $w_{0x,y}$  and  $z_{0x,y}$  can be determined via a fit of the data onto Eq. (3.6) via the Levenberg-Marquardt algorithm. In order to place the PPKTP as best as possible in the waist of pump and collection beam, appropriate focal lengths are chosen for the lenses of the fiber in- and outcouplers, followed by a fine adjustment of the relative distances of the respective coupler lenses.

Since the collection beam traverses more crystals than the pump beam and is also divided into more parts, its alignment therefore is more complicated. The idea is to first setup the collection side of the source and then adjust the pump side accordingly. As for the determination of the beam parameters beam radii close to the focus as well as outside the Rayleigh length are needed, it is problematic to determine the waist position while the PPKTP is inserted at the focus, since the camera cannot be placed there. Due to the different refractive index of the

## 4 Alignment of the photon source

---

(a) Beam parameters for close SPDC site

pump <b>close</b>	collection lower	collection upper
$\omega_{0x} = 39.1 \text{ } \mu\text{m}$ $z_{0x} = 0.5 \text{ mm}$ $M_x^2 = 1.71$	$\omega_{0x} = 44.8 \text{ } \mu\text{m}$ $z_{0x} = 0 \text{ mm}$ $M_x^2 = 1.63$	$\omega_{0x} = 48.9 \text{ } \mu\text{m}$ $z_{0x} = 0.4 \text{ mm}$ $M_x^2 = 1.94$
$\omega_{0y} = 50.2 \text{ } \mu\text{m}$ $z_{0y} = 2.0 \text{ mm}$ $M_y^2 = 2.20$	$\omega_{0y} = 43.2 \text{ } \mu\text{m}$ $z_{0y} = -0.4 \text{ mm}$ $M_y^2 = 1.76$	$\omega_{0y} = 68.3 \text{ } \mu\text{m}$ $z_{0y} = 3.3 \text{ mm}$ $M_y^2 = 2.94$

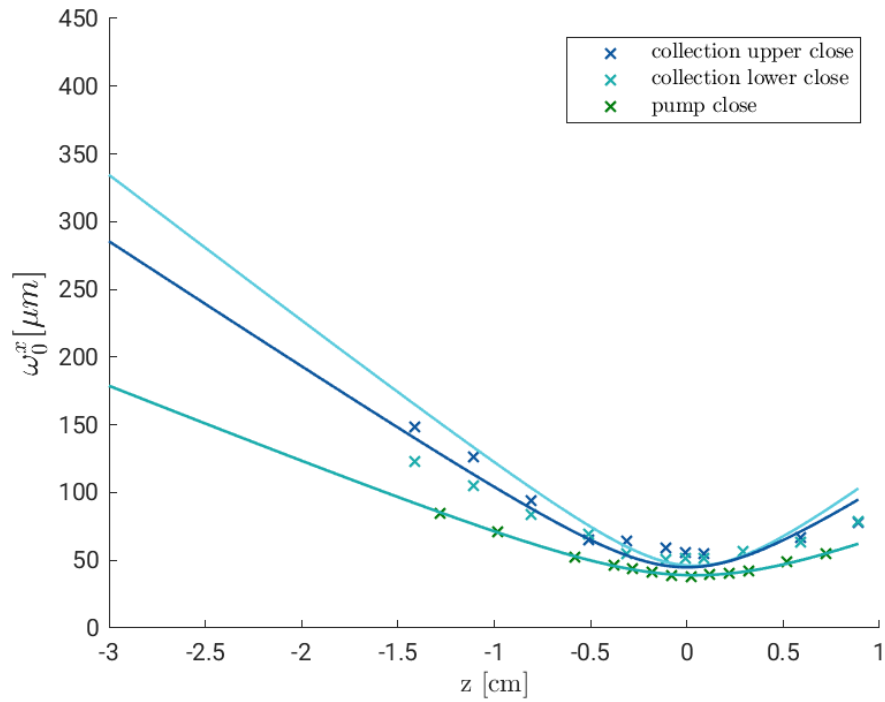
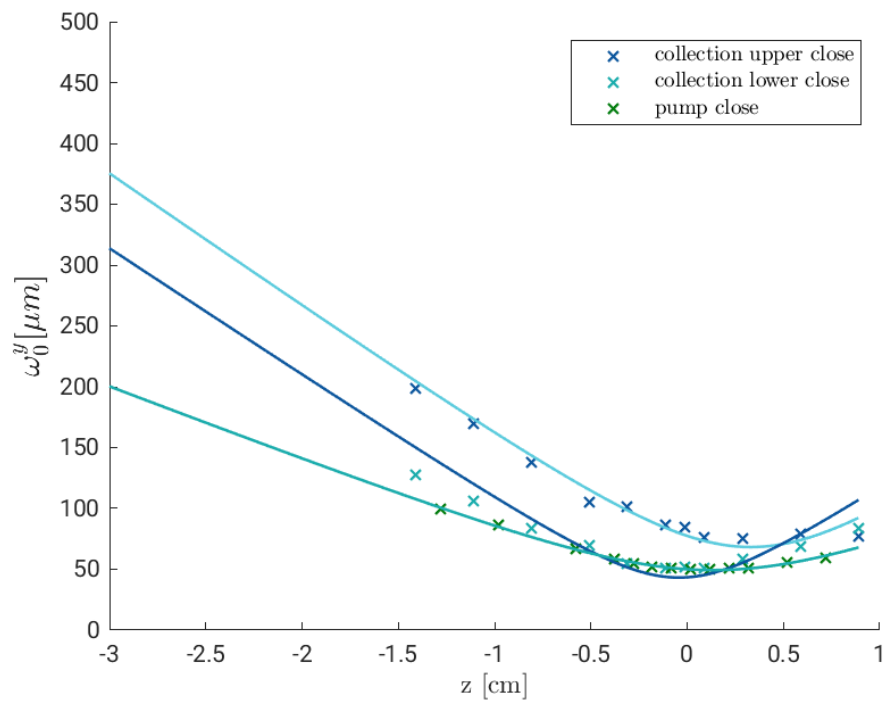
(b) Beam parameters for far SPDC site

pump <b>far</b>	collection lower	collection upper
$\omega_{0x} = 38.6 \text{ } \mu\text{m}$ $z_{0x} = -0.2 \text{ mm}$ $M_x^2 = 1.68$	$\omega_{0x} = 49.4 \text{ } \mu\text{m}$ $z_{0x} = 0.3 \text{ mm}$ $M_x^2 = 2.19$	$\omega_{0x} = 45.1 \text{ } \mu\text{m}$ $z_{0x} = -0.1 \text{ mm}$ $M_x^2 = 2.05$
$\omega_{0y} = 51.0 \text{ } \mu\text{m}$ $z_{0y} = -1.6 \text{ mm}$ $M_y^2 = 2.23$	$\omega_{0y} = 49.9 \text{ } \mu\text{m}$ $z_{0y} = -2.0 \text{ mm}$ $M_y^2 = 1.96$	$\omega_{0y} = 49.8 \text{ } \mu\text{m}$ $z_{0y} = 0.2 \text{ mm}$ $M_y^2 = 2.11$

**Table 4.1:** Beam parameter in  $x$ - and  $y$ -direction for the three beams overlapping at the two SPDC sites

PPKTP, the focus position of the beam in the PPKTP is shifted compared to its position in free space. Hence, after having inserted the  $x_c$ - and  $y_c$ -crystals the beam profiles of the four collection beams were measured without PPKTP and then the shift of the focus position caused by the inserted PPKTP was obtained from a fit with the focus position  $z_0$  as the only free parameter. This made it possible to find the final average focal position of the four collection beams on which to center the PPKTP in  $z$ -direction. After this position for the collection couplers was fixed, the longitudinal position of the pump focus had to be aligned accordingly. This was achieved by repeating the same procedure in forward direction. Due to spatial restrictions it was not possible to take images of the beam profile far away from the focus position of the pump beam, which decreases the accuracy of the fitted parameters. The measured beam parameter of pump and collection beam for the close and far side are given in table 4.1.

We noted that that for points close to the focus position the fitted beam radius was always bigger than the the focus radius determined via a Gaussian fit onto the intensity profile of a picture taken close to the focus position. While the radii used for the fit were determined by the standard deviation of the intensity distribution, these distribution consisted of an approximately Gaussian distribution, with a significant broadening at the lower ends of the edges (see Fig. 4.3  $x$ -direction). Hence, it can be assumed that the obtained standard deviation overestimates the width of the part of the intensity which is relevant for the downconversion process. An average waist of  $\omega_{0G} = 40.3 \text{ } \mu\text{m}$  could be determined for the collection

(a) Beam profile in  $x$ -direction(b) Beam profile in  $y$ -direction

**Figure 4.1:** Fitted and measured beam profile of the collection and pump beam for the close SPDC site. The measured data is indicated with a cross.

## 4 Alignment of the photon source

---

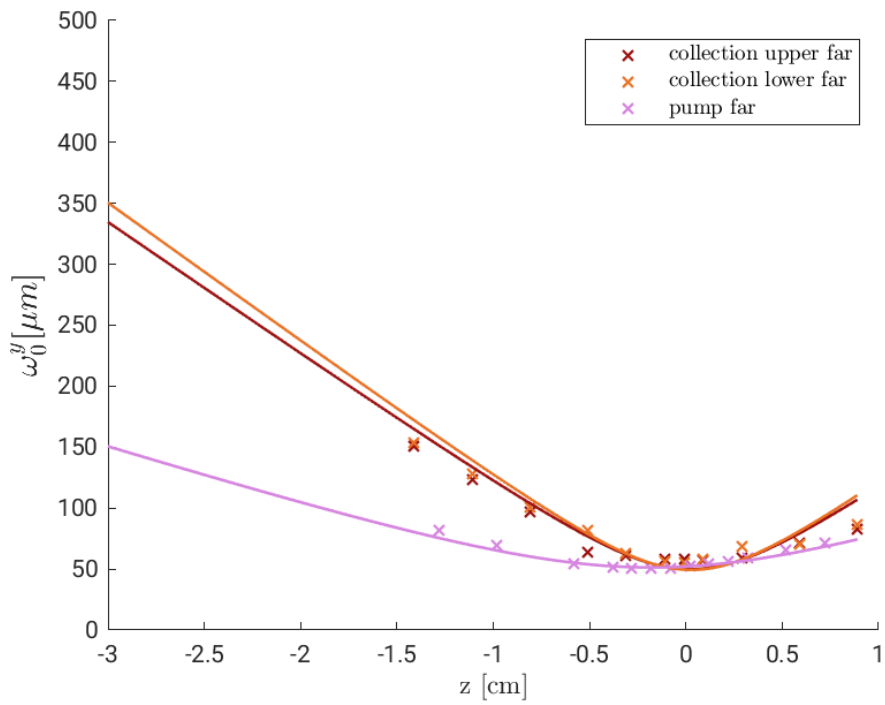
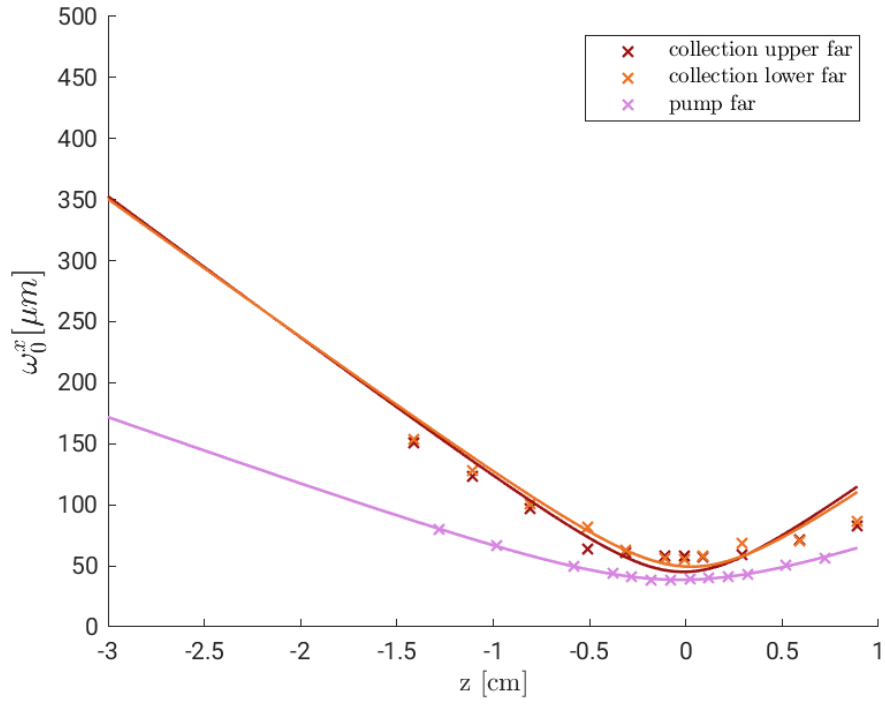


**Figure 4.2:** Fitted and measured beam profile of the collection and pump beam for the far SPDC site. The measured data is indicated with a cross.

beams. The intensity profiles of the close upper collection beam (Fig. 4.1) did not only show the broadening at the base of the distribution but also large tails in  $y$ -direction (see Fig. 4.3  $y$ -direction). Therefore, the determination of the  $z$ -distribution of the beam radius was not trustful, such that for the determination of the  $z$ -position of the PPKTP this focus position was not deemed reliable and thus only weighted with 50%. The measured evolutions for the close and far beams in  $x$ - as well as in  $y$ -direction can be seen in Fig. 4.1 and Fig. 4.2.

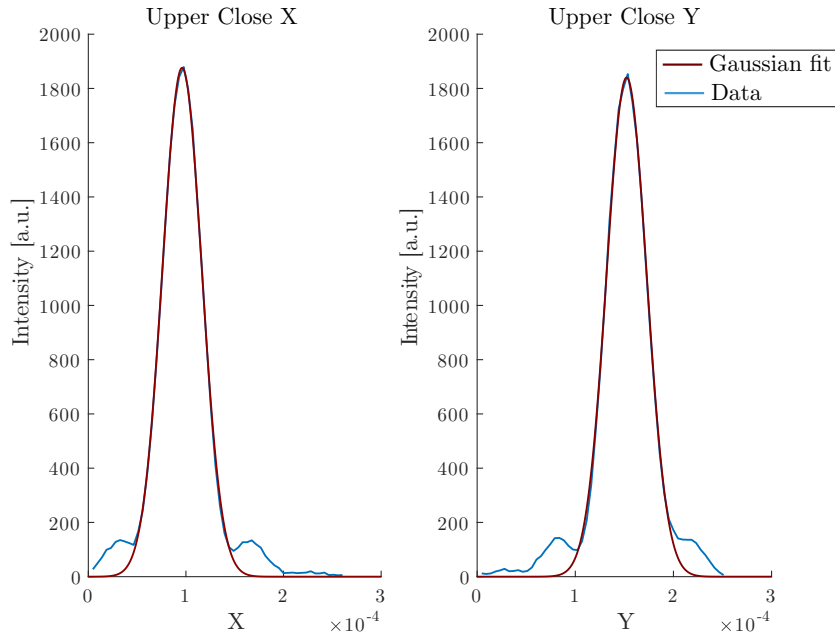


**Figure 4.3:** Measured intensity profile together with the Gaussian fit for the upper close collection beam. All collection beams showed a significant broadening at the lower end of the edges. Only the close upper beam additionally showed large tails in  $y$ -direction.

The root mean squared (RMS) a measure for the goodness of the fit, with  $RMS = \sqrt{\sum_i (f(z_i) - y_i)^2}$  where  $y_i$  are the measured data to corresponding  $z_i$  and  $f(z_i)$  the value achieved from the fit  $10 \mu\text{m}$  for the collection beam, for the pump beam it was lower.

## 4.2 Angular and spatial overlap of the beams

Apart from the adjustment of the waist position in  $z$ -direction it is also necessary to overlap the collection beams in  $x$ - and  $y$ -direction as well as in their angle, as a good overlap of the beams results in a higher collection of coincidences, because both couplers then collect the collinearly emerging SPDC photons from the same spot.

Responsible for the spatial overlap are the  $x_c$ - and  $y_c$ - crystals, which both can be adjusted such that they separate  $H$ - and  $V$ - polarization. As the direction of deflection is determined by the direction of the optical axis relative to the propagation direction, the separation of the polarizations is dependent on the orientation of the crystal. Hence, considering a  $x$ -crystal, which is constructed such that it deflects  $H$ -polarized light in the horizontal plane, a rotation around the  $y$ -axis changes the separation of the beams, whereas the polarization of the two beams can be fine tuned by rotation around the  $x$ - and  $z$ -axes. A rotation of the crystal around these axes is also responsible for a height difference of the two exiting beams, as it defines the plane of deflection.

Since the crystals do not change the propagation direction of the beams, but their effect on the beams depends on their propagation direction, the beam is aligned parallel to the horizontal plane before the crystals are inserted and again fine aligned afterwards. For the alignment again a CCD camera is used, where the separation of two beams can be read off via Gaussian fits to their intensity distributions on the screen. The deviation of the propagation direction from a horizontal plane can be determined by taking images of the beam profile at various  $z$ -positions and then corrected by tuning the angle of the couplers and the mirror.

The alignment was started with the  $x_c$ -crystal. An alignment such that  $H$  and  $V$  are the eigenaxes of the crystal transformation could be performed by only letting e.g.  $H$ -polarized light enter the crystal and then minimizing the amount of  $V$ -polarized outgoing light by rotating the crystal. At the same time it has to be ensured that there is no height difference between the outgoing beams, which is why the two axes of rotation  $x$  and  $z$  are walked against each other, one minimizing the height difference, the other defining  $H$  and  $V$  as eigenaxes. The same procedure is repeated for the  $y_c$ -crystal such that the four beams are merged to two. After fine tuning the angle of the propagation direction the two times two beams overlap close to their focus positions as shown in Fig. 4.4. The size of the foci is taken from the previous section. As the two images are recorded at  $z$ -planes separated by 2.5cm it is possible to extract the angular deviation of the beams from the position difference between the two images.

For the overlap of the pump and collection beam it is important that the collection beam is separated by its  $x_c$ -crystal by the same amount as the pump beam is by its  $x_p$ -crystal, which is why when the alignment is repeated for the pump beam the separation of the beams has to be exactly adjusted to the separation obtained by the  $x_c$ -crystal, which is around 4.16 mm.

## 4.2 Angular and spatial overlap of the beams

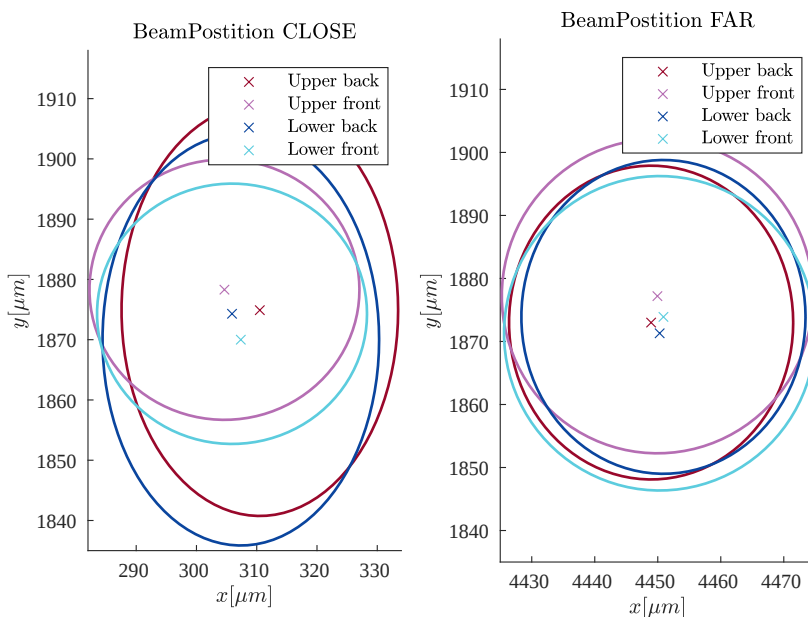


**Figure 4.4:** Overlap of the upper and lower collection beam at the focus position at two different  $z$ -positions.

As it is not possible to determine the exact  $x$ -positions of the collection and pump beam with respect to each other, this can be fine tuned after the SPDC crystal is inserted and the source is connected to the APDs, since small changes in position do not change the previous adjustments of the setup. The pump coupler is then moved in  $x$ -direction such that the number of singles and coincidences was maximized in order to increase the overlap of pump and collection beams. In the course of further alignment steps, the coupling was repeatedly further optimized by tuning the collection couplers' angles and positions against each other, always with the goal to get more coincidences at the same number of singles, hence, decreasing the rate  $R_{sc} = \frac{\text{coincidences}}{\text{singles}}$ , which means increasing the overlap of the parts of the beams containing corresponding photon pairs.

### 4.3 Sources of coherence reduction

After the alignment described in section 4.2 was completed a significantly better  $zz$ -correlation,  $\kappa_{zz} > 0.9$ , was obtained compared to the  $yy$ - or  $zz$ -direction  $|\kappa_{xx,yy}| < 0.7$ .

This effect can be explained by a loss of coherence. The created state can be described with all its degrees of freedoms via

$$|\Psi\rangle = \frac{1}{\sqrt{2}}(|H, R_1\rangle|H, R_2\rangle + |V, R_3\rangle|V, R_4\rangle), \quad (4.1)$$

with  $|a, b\rangle = |a\rangle \otimes |b\rangle = |a\rangle|b\rangle$  and where the  $|R_i\rangle$  denote the other degrees of freedom like wavelength or traveled optical path which can encode the information about the SPDC-site. Expressing this state with its density matrix and performing a partial trace with respect to the not measured degrees of freedom, the density matrix in the polarization basis of the two qubits  $\{|HH\rangle, |HV\rangle, |VH\rangle, |VV\rangle\}$  reads

$$\hat{\rho} = \frac{1}{2} \begin{pmatrix} 1 & 0 & 0 & \langle R_1|R_3\rangle\langle R_2|R_4\rangle \\ 0 & 0 & 0 & 0 \\ 0 & 0 & 0 & 0 \\ \langle R_3|R_1\rangle\langle R_4|R_2\rangle & 0 & 0 & 1 \end{pmatrix} \quad (4.2)$$

Hence, the overlap of the wavepackets in the space of the different degrees of freedom is relevant for the degree of entanglement. With decreasing overlap of the wavepackets, the two SPDC sites become more and more distinguishable such that entanglement decreases until a mixed state of 50%  $|HH\rangle$  and 50%  $|VV\rangle$ , is reached. This loss of coherence is reflected by a decrease of correlations  $\kappa_{xx} = -\kappa_{yy} = \text{Re}[\langle R_1|R_3\rangle\langle R_2|R_4\rangle]$  compared to  $\kappa_{zz} = 1$ .

The overlap of the wavepackets in time is given by the longitudinal coherence length

$$l_C \approx \frac{\lambda^2}{\Delta\lambda} \quad (4.3)$$

where  $\lambda = 810 \text{ nm} = \lambda_c$  is the collection wavelength. The width of the spectral distribution is not that easy to specify. For this the spectral emission of the SPDC photons from section 3.2.2 has to be regarded. Since the adjusted collection beam has a divergence of  $\theta_{div} = \frac{\lambda}{\pi w_0} \approx 0.3^\circ$ , the deviation of the collected wavelength from  $\lambda_c$  is in a perfect collinear process with perfect collection not larger than 1 nm. But as it was demonstrated in section 3.2.2 the wavelength of the collected photons is dependent on the angle between the pump beam and the axes of the PPKTP as well as on the angle of the collection beam. This is why here a larger spectral width is chosen corresponding to the FWHM of a spectral filter later introduced into the setup  $\Delta\lambda \approx 3 \text{ nm}$ . This leads to an coherence length of  $l_C \approx 219 \text{ }\mu\text{m}$ , which should be significantly greater than differences in traveled optical path.

Furthermore, the wavepackeges also have to overlap in their spectral degree of freedom, such that a difference in the center wavelength of the spectra of the

components can also lead to a loss of coherence. Additionally, as a difference in wavelength of the collected components introduces also a pathlength difference, it can lead to the phase between the components no longer being well-defined. This can be caused, e.g. by small spectral fluctuations of the pump laser.

### 4.3.1 Tilted crystals

Since all used waveplates are zero order, their passage does not lead to a difference in optical path length. Also the y-crystal does not introduce a path difference between the close and the far beam such that it does not disturb the indistinguishability of the SPDC sites. The effective path difference  $\Delta\xi$  can therefore come from differences in optical path in the two  $x$ -crystals at different wavelengths  $\lambda_p$  and  $\lambda_c$ .  $\Delta\xi$  is hence the difference between the path difference of the ordinary and extraordinary beam in the pump  $x$ -crystal and the corresponding path difference in the collection  $x$ -crystal,  $\Delta\xi = |\xi_{far} - \xi_{close}| = |\Delta\xi_p - \Delta\xi_c|$ .

For a perfectly aligned source the calculated optical path difference  $\Delta\xi$  is around  $34 \mu\text{m} \approx 42\lambda_c$ , since the beams traverse the two  $x$ -crystals at different wavelengths, before and after the downconversion, such that the optical pathlengths differences are not completely canceled out. It is a convenient property of the calcites, that the differences in optical path traveled by the 810 nm and 405 nm light is that small. However, if the crystals are slightly tilted, the differences in the optical pathlengths change, as now the ordinary as well as the extraordinary beam is deflected by Snell's law and the traveled distances inside the crystal where the two experience different refraction indices now depend on the incident angle  $\alpha$ . Fig. 4.5 shows the change in the optical path difference when the two  $x$ -crystals are rotated around the  $z$ -axis by the same angle  $\alpha$  but in different directions. As we can see, at angles around  $1^\circ$  to  $2^\circ$  easily path differences in the order of magnitude of the coherence length are reached. As a rotation by a that small angle can not be excluded, this is a possible explanation for the observed loss of coherence.

### 4.3.2 Collection of different wavelengths

A possible reason of spectral decoherence are correlations between emission angle and spectrum. If the components of a photon's state are collected at the two sites from different regions and under different angles, this may arise differences in the spectrum of these components. If the center wavelengths of two photons arriving at the coupler are further apart compared to their spectral width, it is obvious that the wavelength of the arriving photon encodes the which-site information, which reduces the entanglement, since  $\langle R_{1/2} | R_{3/4} \rangle \propto \exp - \frac{(\lambda_{1/2} - \lambda_{3/4})^2}{4\Delta\lambda^2} < 1$ , assuming Gaussian distributions for the wavelengths.

Hence, according to Eq. (4.2) the correlation  $\kappa_{xx} \propto \exp - \frac{(\lambda_1 - \lambda_3)^2 + (\lambda_4 - \lambda_4)^2}{4\Delta\lambda^2}$ , such that already small deviations in the center wavelengths lead to a loss of coherence. A correlation of 0.94 would therefore be reached when the center wavelengths of the components of the lower as well as of the upper beam are further off than

## 4 Alignment of the photon source

---

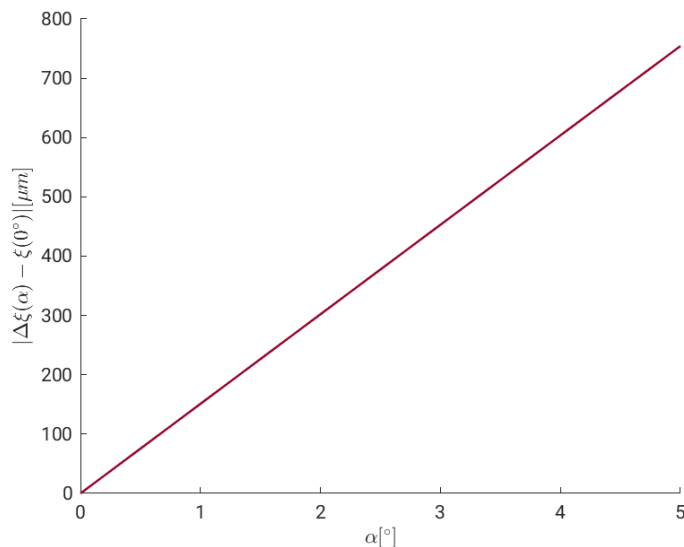


**Figure 4.5:** Additional optical path difference  $|\Delta\xi(\alpha) - \Delta\xi(0^\circ)|$  arising from tilted crystals

1.35 nm. The correlation of 0.7 could then be explained by coupling different wavelengths at both sites with center wavelengths further apart than 2.5 nm.

It has to be also kept in mind that the photons are traveling different paths in the setup, such that the non-equal wavelength result in different optical paths for distinct photons, which can affect coherence. The change of the optical path differences  $\Delta\xi(\lambda)$  compared to  $\Delta\xi(\lambda_c)$  at the degenerate wavelength can be calculated and is shown in Fig. 4.6 for wavelengths from 805 nm to 815 nm. The change in optical pathlength difference compared to the degenerated case is about 0.5 μm for wavelength  $\lambda = \lambda_c \pm 5$  nm. Since this is very small compared to the coherence length, decoherence due to optical path differences must come from tilted crystals.

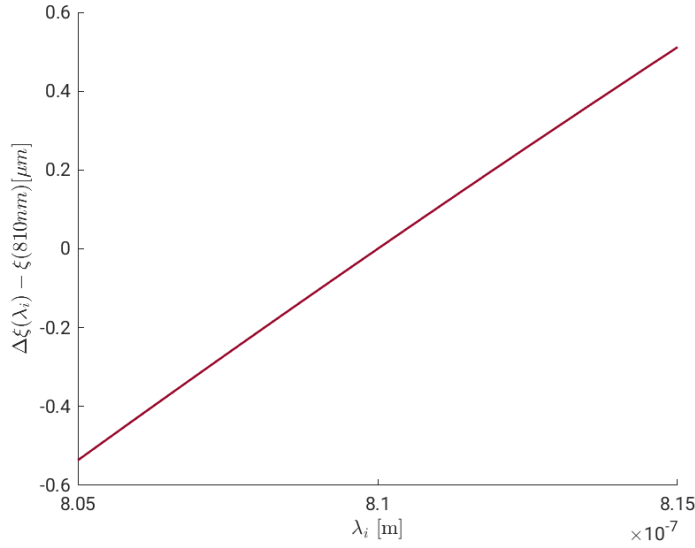


**Figure 4.6:** Additional optical path difference  $\Delta\xi(\lambda) - \Delta\xi(810 \text{ nm})$  arising from the collection of non degenerated photon pairs.

## 4.4 Increasing coherence

In order to eliminate this arising loss of coherence different ways of compensation were implemented. On the one hand, there were filters to adjust the center wavelength and on the other hand glass plates were inserted for pathlength compensation of one arm.

**Glass plate** An insertion of a 1mm glass plate of refractive index  $n_G \approx 1.52$  into the far beams before the PPKTP crystal (see Fig. 3.9) lifted up the  $xx$ -correlation from  $\sim 0.6$  up to  $\sim 0.9$ . When the glass plate is rotated, the  $xx$ -correlation oscillates determined by different influences. The correlation is observed to change quickly following the cosine of Eq. (3.51) due to the variation of the phase due to the rotation of the glass plate, while the maxima of this oscillation decrease slowly, indicating the influence of growing decoherence. It was noted also that this improvement to 0.9 was only visible when the glass plate was inserted into the far arm and not into the close one, which seems to indicate that the close arm traveled the longer optical path. Glass plates of different thicknesses were tested, resulting in best  $xx$ -correlation of the 1mm glass plate. A glass plate of  $d_G \approx 0.1$  mm thickness enabled only correlations  $|\kappa_{xx}| \leq 0.56$  and another one of thickness  $d_G \approx 0.3$  mm  $|\kappa_{xx}| \leq 0.8$ . Fig. 4.7 shows the calculated path difference introduced by glass plates of various thicknesses. The 1 mm glass plate hence induces a path difference of approximately  $500 \mu\text{m}$ , which would correspond to a tilt of the x-crystals of about  $3^\circ$  (Fig. 4.5).

The problem with this method is that the rotation of the glass plate also slightly changes the position of the beam, which can affect the coupling efficiency of

## 4 Alignment of the photon source

the photons at this site. Consequently, different wavelengths can be collected. Changes in the relation of amplitudes of the different SPDC sites can be compensated by the initial HWP each time the glass plate is rotated to a maximum of  $xx$ -correlation.

With the the glass plate it was possible to increase the correlation to  $|\kappa_{xx,yy}| \approx 0.9$ , but not above. One reason for this could be that the employed 1 mm glass plate is to thick and therefore induces a too large pathlength difference, whereas the 0.3 mm are still too thin.

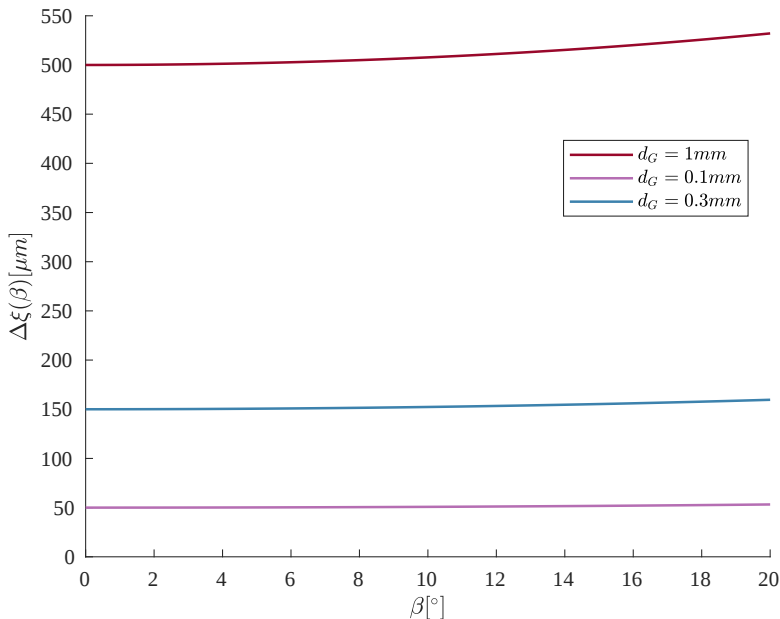


**Figure 4.7:** Additional path difference  $\Delta\xi(\beta)$  arising from a rotatable glass plate of various thickness  $d_G$  only traversed by photons of one SPDC site.

**Filters** Different filters were tested in order to firstly reduce the spectral width of the photons and secondly, as the PPKTP is manufactured to produce preferably 810 nm collinear photon pairs, to optimize the coupling and improve the coincidence-photon-rate.

The initial measurements were performed with edgepass filters, only transmitting wavelengths above 750 nm. It was observed that no pump photons were reaching the detection, as all detected singles and coincidences vanish when the waveplate in front of the PPKTP is flipped, such that no SPDC will happen anymore. Taking the filters out of the setup did not change the maximum correlation at all. This indicates that they did not affect the spectral properties of the downconverted photons significantly and also without them the pump beam is sufficiently excluded from the collection. Since, besides the tiny shift in position of the beam by the insertion of an optical component, also the angle of the emerging photons can be changed by filtering the wavelength due to correlation between emission angle and wavelength, after each insertion or rotation of a filter

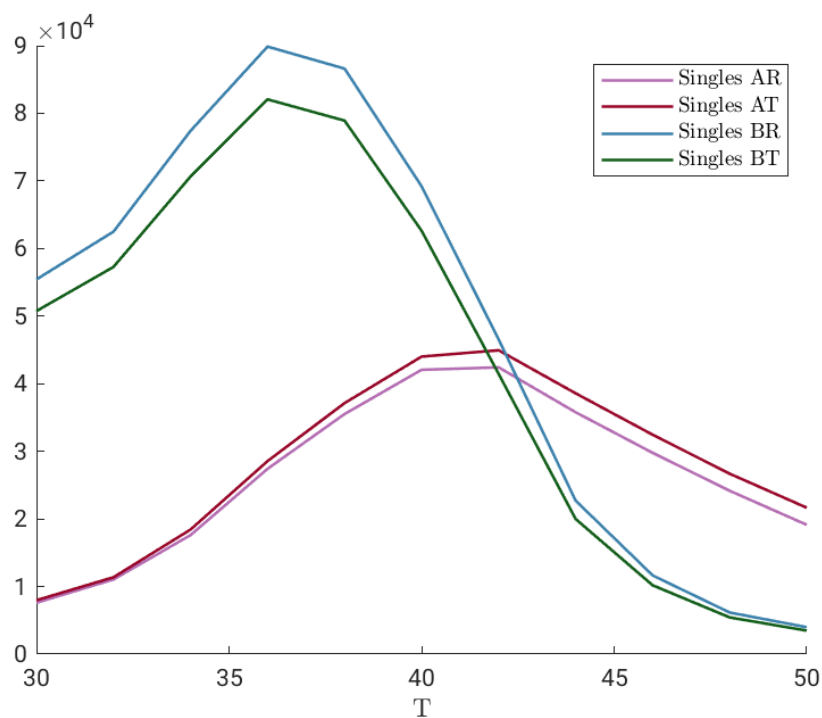
a new iteration of the coupling optimization was needed.

In the next step, in order to ensure the collection of degenerate photons, bandpass filters of 10 nm FWHM centered around 810 nm were inserted. No improvement of the correlation was found. Also changing the temperature of the PPKTP from 25°C to 50°C, which influences the wavelength of the generated photon pairs (section 3.2.2), did not affect the rate of detected photons, so it can be assumed that the filters' width was still too large.

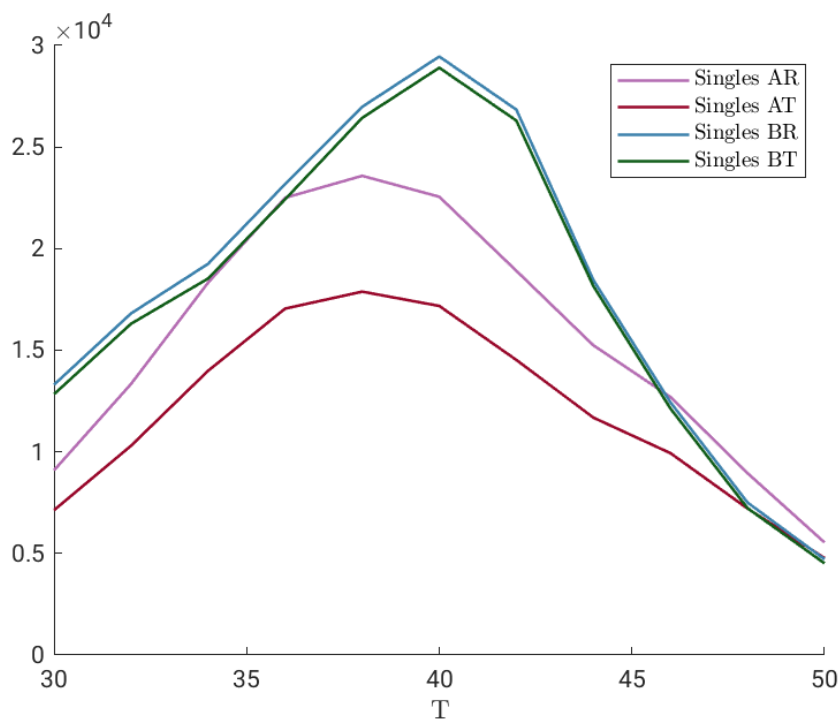
Finally, a narrower bandpass filter with 3 nm FWHM centered around 810 nm was tried. As explained before (see section 3.1.2) the center wavelengths of bandpass filters are highly dependent on the angle of incidence which is why we only replaced the filter before the mirror in order to assure the same filtering for both photons with only a single degree of angular adjustment. To adjust this angle, the PPKTP temperature is changed from 25° to 50° while the collected singles in the couplers are counted. A maximum of singles then corresponds to the center wavelength of the filter. Since the PPKTP creates collinear degenerated photon pairs only at one specific wavelength, the maxima of singles of both arms must lie at the same temperature if the filter transmits the degenerate wavelength, whereas when a deviating wavelength is filtered the maxima lie apart. Fig. 4.8 shows the first temperature scan, where both maxima are visibly displaced, whereas after a little rotation of the filter the maxima were found approximately at the same temperature  $T \approx 39^\circ\text{C}$ . This filter setting improved our correlations to  $|\kappa_{xx}| \approx 0.94$  at an operating temperature of  $39^\circ\text{C}$ .

The deviation of the temperature from the theoretical calculation  $T_{deg} \approx 50^\circ$  implies there might be other issues which still have to be checked. This deviation could be explained by a slight rotation of the PPKTP with respect to the pump beam changing the temperature dependence of the downconversion process.

## 4 Alignment of the photon source



(a) First insertion of the filter. Maxima are not at the same temperature.



(b) Rotation of the filter. Maxima move closer together, which indicates a better collection of the desired degenerated wavelength.

**Figure 4.8:** Detected singles as a function of temperature for two different filter positions of a 3 nm FWHM bandpass filter.

## 4.5 Final state tomography

A final measurement of the correlations in every basis  $\hat{\sigma}_i \otimes \hat{\sigma}_j$  and a resulting reconstruction of the density matrix as described in section 3.3.4 yields the density matrix

$$\hat{\rho} = \begin{pmatrix} 0.460 & 0.030 + 0.009i & -0.036 + 0.026i & -0.462 - 0.001i \\ 0.027 - 0.001i & 0.005 & -0.001 + 0.001i & -0.040 + 0.018i \\ -0.036 - 0.023i & -0.001 - 0.001i & 0.004 & 0.030 + 0.023i \\ -0.462 + 0.001i & -0.040 - 0.018i & 0.030 - 0.023i & 0.531 \end{pmatrix}.$$

The state is illustrated in Fig. 4.9. The negativity (1.28) of this state is  $\mathcal{N} = 0.460$  and the fidelity (3.53) between it and the Bell state  $|\Psi^-\rangle = \frac{1}{\sqrt{2}}(|HH\rangle - |VV\rangle)$  is  $\mathcal{F} = 0.959$ . The state  $|\Psi^-\rangle$  is only rotated by a phase of  $\pi$  with respect the desired state, which can be easily corrected via phase compensation with the YVO pair.

Note that the elements of the density matrix obtained by the expectation values of the measurements in each basis have a statistical error (see Eq. (2.30)) due to the finite number of counts. This error propagates into the maximum likelihood reconstruction which was shown to cause systematic errors [103].

The small deviations in fidelity and negativity from the ideal values of the maximally entangled Bell-state  $\mathcal{F}_{\Psi^-} = 1$  and  $\mathcal{N}_{\Psi^-} = 0.5$  are due to the reduction of coherence described in the previous sections. The optimization of this by rotations of the PPKTP crystal and testing glass plates of thickness  $0.3 \text{ mm} \leq d_G \leq 1 \text{ mm}$  will be a future task.

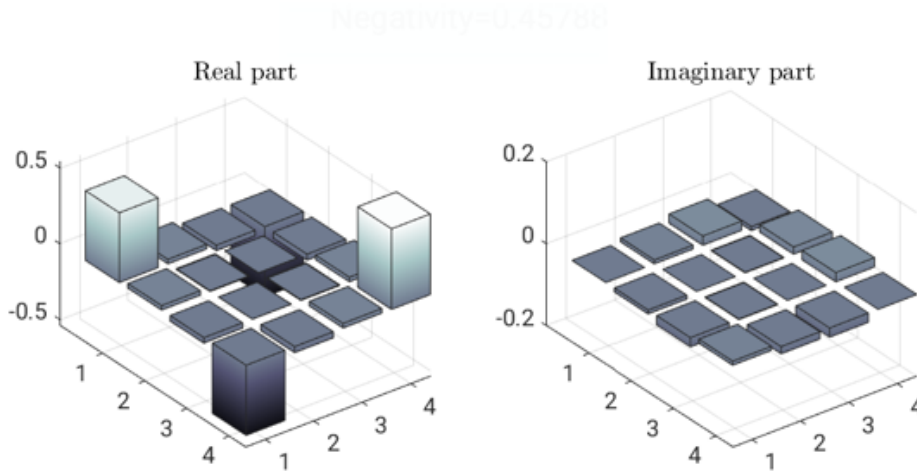


**Figure 4.9:** Illustration of the final density matrix.



# Conclusion

Bohmian trajectories of photons in a double slit interferometer have already been measured. The entanglement between the which-way information and another photon's polarization makes which-way measurements possible. Furthermore, the possibility of performing the which-way measurement while the photon is in the interference region or already detected on the screen will enable delayed choice measurements. Therefore, in this thesis an entangled photon source using spontaneous parametric down-conversion in a PPKTP crystal was implemented providing a Bell-state of fidelity  $\mathcal{F} = 0.959$ . The calculation of the spatial distribution of the emission of photons in the down-conversion process gives rise to possibilities of enhancing the quality of the photon source in the future: A final improvement of the coupling together with tiny rotations of the PPKTP crystal is expected to yield higher photon count numbers together with a high degree of entanglement.

Additionally, an alternative method to measure photon trajectories was elaborated. Measuring the wavefront of the photons in the interference region of the double slit allows the observation of Bohmian trajectories as via weak measurements. For this purpose a wavefront sensor was tested and turned out to be able to resolve the deviation in the wavefront caused by the main interference maximum for classical light. This provides a basis for further investigation with single photons.

With the results of this thesis it will soon be possible to start the experiment on the observation of Bohmian trajectories connected with which-way measurements. These can then be spacelike separated from the double slit in order to enable delayed-choice measurements, providing further understanding of the non-locality of the Bohmian theory. The explanation of the results of the experiment will then be a challenging task for the Bohmian theory. Nevertheless, the more knowledge gained, the greater the chances, that the theory and the long ongoing debate about it will evolve.

## Conclusion

---

# Abbreviations

<b>APD</b>	Avalanche photo diode
<b>BS</b>	Beam splitter
<b>BM</b>	Bohmian mechanics
<b>FWHM</b>	Full width at half maximum
<b>HWP</b>	Half-wave plate
<b>PPKTP</b>	Periodically poled potassium titanyl phosphate
<b>PBS</b>	Polarizing beam splitter
<b>QM</b>	Quantum mechanics
<b>QWP</b>	Quater-wave plate
<b>SPDC</b>	Spontaneous parametric down-conversion
<b>SQM</b>	Standard quantum mechanics
<b>YVO</b>	Yttrium-vanadate



# List of Figures

1.1	Bloch sphere . . . . .	6
1.2	Pre- and postselection . . . . .	13
1.3	Weak measurement on PPS . . . . .	15
2.1	Double slit . . . . .	26
2.2	Quantum potential . . . . .	29
2.3	Bohmian trajectories . . . . .	30
2.4	Transverse Bohmian momentum . . . . .	31
2.5	Surreal trajectories . . . . .	32
2.6	Shack-Hartmann wavefront sensor . . . . .	40
2.7	Estimation of transverse momentum measurement . . . . .	42
2.8	Wavefront measurement . . . . .	43
3.2	Coordinate system for SPDC calculation . . . . .	54
3.3	Wavelength-temperature dependence in SPDC . . . . .	55
3.4	Angular distribution for different wavelengths . . . . .	56
3.5	Spatial emission for $\lambda_{s,i} = 810 \pm 0.2$ . . . . .	57
3.6	Spatial emission for $\lambda_{s,i} = 808 \pm 0.2$ . . . . .	58
3.7	Wavelength-temperature dependence for tilted pump vector . . . . .	58
3.8	Complete setup . . . . .	59
3.9	Entangled photon source setup . . . . .	61
3.10	Tomography setup . . . . .	66
4.1	Beam profiles close SPDC site . . . . .	71
4.2	Beam profiles far SPDC site . . . . .	72
4.3	Measured intensity profile . . . . .	73
4.4	Overlap . . . . .	75
4.5	Path difference due to tilted crystals . . . . .	78
4.6	Path difference due to deviating wavelengths . . . . .	79
4.7	Path difference introduced by glass plate . . . . .	80
4.8	Temperature dependence of coupled singles . . . . .	82
4.9	Final state density matrix . . . . .	83



# Bibliography

- [1] D. Bohm, „A Suggested Interpretation of the Quantum Theory in Terms of ‘Hidden’ Variables. I“, *Physical Review*, vol. 85, no. 2, 1952. DOI: [10.1103/physrev.85.166](https://doi.org/10.1103/physrev.85.166).
- [2] D. Bohm, „A Suggested Interpretation of the Quantum Theory in Terms of ‘Hidden’ Variables. II“, *Physical Review*, vol. 85, no. 2, 1952. DOI: [10.1103/physrev.85.180](https://doi.org/10.1103/physrev.85.180).
- [3] R. Feynman, *The Feynman lectures on physics*. Reading, Mass: Addison-Wesley Pub. Co, 1963.
- [4] B.-G. Englert *et al.*, „Surrealistic Bohm Trajectories“, *Zeitschrift für Naturforschung A*, vol. 47, no. 12, 1992. DOI: [10.1515/zna-1992-1201](https://doi.org/10.1515/zna-1992-1201).
- [5] H. M. Wiseman, „Grounding Bohmian mechanics in weak values and bayesianism“, *New Journal of Physics*, vol. 9, no. 6, 2007. DOI: [10.1088/1367-2630/9/6/165](https://doi.org/10.1088/1367-2630/9/6/165).
- [6] S. Kocsis *et al.*, „Observing the Average Trajectories of Single Photons in a Two-Slit Interferometer“, *Science*, vol. 332, no. 6034, 2011. DOI: [10.1126/science.1202218](https://doi.org/10.1126/science.1202218).
- [7] D. H. Mahler *et al.*, „Experimental nonlocal and surreal Bohmian trajectories“, *Science Advances*, vol. 2, no. 2, 2016. DOI: [10.1126/sciadv.1501466](https://doi.org/10.1126/sciadv.1501466).
- [8] D. J. Griffiths, *Introduction to Quantum Mechanics*. Cambridge University Press, 2018. DOI: [10.1017/9781316995433](https://doi.org/10.1017/9781316995433).
- [9] J. J. Sakurai and J. Napolitano, *Modern Quantum Mechanics*. Cambridge University Press, 2017. DOI: [10.1017/9781108499996](https://doi.org/10.1017/9781108499996).
- [10] M. A. Nielsen and I. L. Chuang, *Quantum Computation and Quantum Information*. Cambridge University Press, 2009. DOI: [10.1017/cbo9780511976667](https://doi.org/10.1017/cbo9780511976667).
- [11] P. A. M. Dirac, „A new notation for quantum mechanics“, *Mathematical Proceedings of the Cambridge Philosophical Society*, vol. 35, no. 3, 1939. DOI: [10.1017/s0305004100021162](https://doi.org/10.1017/s0305004100021162).
- [12] B. Thaller, *Visual Quantum Mechanics*. Springer New York, 2000. DOI: [10.1007/b98962](https://doi.org/10.1007/b98962).
- [13] Barnett, *Quantum information*. Oxford University Press UK, 2009.
- [14] R. Horodecki *et al.*, „Quantum entanglement“, *Rev. Mod. Phys.*, vol. 81, 2 2009. DOI: [10.1103/RevModPhys.81.865](https://doi.org/10.1103/RevModPhys.81.865).
- [15] O. Gühne and G. Toth, „Entanglement detection“, *Physics Reports* 474, 1, 2008. DOI: [10.1016/j.physrep.2009.02.004](https://doi.org/10.1016/j.physrep.2009.02.004). arXiv: [0811.2803v3](https://arxiv.org/abs/0811.2803v3) [quant-ph].

- [16] G. Vidal and R. F. Werner, „A computable measure of entanglement“, *Phys. Rev. A* *65*, 032314, 2001. DOI: [10.1103/PhysRevA.65.032314](https://doi.org/10.1103/PhysRevA.65.032314). arXiv: [quant-ph/0102117v1](https://arxiv.org/abs/quant-ph/0102117v1) [quant-ph].
- [17] K. Życzkowski *et al.*, „Volume of the set of separable states“, *Physical Review A*, vol. 58, no. 2, 1998. DOI: [10.1103/physreva.58.883](https://doi.org/10.1103/physreva.58.883).
- [18] A. G. Kofman *et al.*, „Nonperturbative theory of weak pre- and post-selected measurements“, *Physics Reports*, vol. 520, no. 2, 2012. DOI: [10.1016/j.physrep.2012.07.001](https://doi.org/10.1016/j.physrep.2012.07.001).
- [19] J. von Neumann, *Mathematische Grundlagen der Quantenmechanik*. Springer Berlin Heidelberg, 1932. DOI: [10.1007/978-3-642-61409-5](https://doi.org/10.1007/978-3-642-61409-5).
- [20] M. Galli, „Measurement of average Bohmian trajectories of photons in a double slit interferometer“, Master’s thesis, 2018.
- [21] Y. Aharonov and L. Vaidman, „Properties of a quantum system during the time interval between two measurements“, *Physical Review A*, vol. 41, no. 1, 1990. DOI: [10.1103/physreva.41.11](https://doi.org/10.1103/physreva.41.11).
- [22] Y. Aharonov and L. Vaidman, „The Two-State Vector Formalism of Quantum Mechanics: an Updated Review“, 2001. arXiv: [quant-ph/0105101v2](https://arxiv.org/abs/quant-ph/0105101v2) [quant-ph].
- [23] Y. Aharonov *et al.*, „How the result of a measurement of a component of the spin of a spin-1/2 particle can turn out to be 100“, *Physical Review Letters*, vol. 60, no. 14, 1988. DOI: [10.1103/physrevlett.60.1351](https://doi.org/10.1103/physrevlett.60.1351).
- [24] B. E. Y. Svensson, „What is a quantum-mechanical ‘weak value’ the value of?“, 2013. DOI: [10.1007/s10701-013-9740-6](https://doi.org/10.1007/s10701-013-9740-6). arXiv: [1301.4328v3](https://arxiv.org/abs/1301.4328v3) [quant-ph].
- [25] B. E. Y. Svensson, „On the interpretation of quantum mechanical weak values“, *Physica Scripta*, vol. T163, 2014. DOI: [10.1088/0031-8949/2014/t163/014025](https://doi.org/10.1088/0031-8949/2014/t163/014025).
- [26] B. E. Svensson, „Non-representative quantum mechanical weak values“, *Foundations of Physics*, vol. 45, no. 12, 2015.
- [27] A. J. Leggett, „Comment on “How the result of a measurement of a component of the spin of a spin- $\frac{1}{2}$  particle can turn out to be 100”“, *Physical Review Letters*, vol. 62, no. 19, 1989. DOI: [10.1103/physrevlett.62.2325](https://doi.org/10.1103/physrevlett.62.2325).
- [28] R. Mir *et al.*, „A double-slit ‘which-way’ experiment on the complementarity-uncertainty debate“, *New J. Phys.* *9* (2007) 287., 2007. DOI: [10.1088/1367-2630/9/8/287](https://doi.org/10.1088/1367-2630/9/8/287). arXiv: [0706.3966v2](https://arxiv.org/abs/0706.3966v2) [quant-ph].
- [29] J. L. Garretson *et al.*, „The Uncertainty Relation in ‘Which-Way’ Experiments: How to Observe Directly the Momentum Transfer using Weak Values“, *J. Opt. B: Quantum Semiclass. Opt.* *6*, s506 (2004), 2003. DOI: [10.1088/1464-4266/6/6/008](https://doi.org/10.1088/1464-4266/6/6/008). arXiv: [quant-ph/0310081v1](https://arxiv.org/abs/quant-ph/0310081v1) [quant-ph].

- 
- [30] H. M. Wiseman, „Directly Observing Momentum Transfer in Twin-Slit ‘Which-Way’ Experiments“, *Physics Letters A* 311, 285-291 (2003)., 2003. DOI: [10.1016/S0375-9601\(03\)00504-8](https://doi.org/10.1016/S0375-9601(03)00504-8). arXiv: [quant-ph/0303139v1](https://arxiv.org/abs/quant-ph/0303139v1) [[quant-ph](#)].
- [31] Y. Xiao *et al.*, „Observing momentum disturbance in double-slit which-way measurements“, *Science Advances*, vol. 5, no. 6, 2019. DOI: [10.1126/sciadv.aav9547](https://doi.org/10.1126/sciadv.aav9547).
- [32] D. Duerr *et al.*, „On the Weak Measurement of Velocity in Bohmian Mechanics“, 2008. DOI: [10.1007/s10955-008-9674-0](https://doi.org/10.1007/s10955-008-9674-0). arXiv: [0808.3324v1](https://arxiv.org/abs/0808.3324v1) [[quant-ph](#)].
- [33] T. Mori and I. Tsutsui, „Quantum trajectories based on the weak value“, *Progress of Theoretical and Experimental Physics*, vol. 2015, no. 4, 2015. DOI: [10.1093/ptep/ptv032](https://doi.org/10.1093/ptep/ptv032).
- [34] J. Dressel *et al.*, „Colloquium: Understanding quantum weak values: Basics and applications“, *Reviews of Modern Physics*, vol. 86, no. 1, 2014. DOI: [10.1103/revmodphys.86.307](https://doi.org/10.1103/revmodphys.86.307).
- [35] L. Vaidman, „Weak-measurement elements of reality“, *Foundations of Physics*, vol. 26, no. 7, 1996. DOI: [10.1007/bf02148832](https://doi.org/10.1007/bf02148832).
- [36] Y. Aharonov and A. Botero, „Quantum averages of weak values“, *Physical Review A*, vol. 72, no. 5, 2005. DOI: [10.1103/physreva.72.052111](https://doi.org/10.1103/physreva.72.052111).
- [37] J. Dziewior *et al.*, „Universality of local weak interactions and its application for interferometric alignment“, *Proceedings of the National Academy of Sciences*, vol. 116, no. 8, 2019. DOI: [10.1073/pnas.1812970116](https://doi.org/10.1073/pnas.1812970116).
- [38] B. Tamir and E. Cohen, „Introduction to Weak Measurements and Weak Values“, *Quanta*, vol. 2, no. 1, 2013. DOI: [10.12743/quanta.v2i1.14](https://doi.org/10.12743/quanta.v2i1.14).
- [39] J. Dziewior, „The Concept of Weak Values“, Master’s thesis, 2016.
- [40] Y. Aharonov and L. Vaidman, „Complete description of a quantum system at a given time“, *Journal of Physics A: Mathematical and General*, vol. 24, no. 10, 1991. DOI: [10.1088/0305-4470/24/10/018](https://doi.org/10.1088/0305-4470/24/10/018).
- [41] Institut International de Physique Solvay, *Electrons et Photons, Rapports et Discussions*. 1927.
- [42] D. Bohm and B. Hiley, *The undivided universe : an ontological interpretation of quantum theory*. London New York: Routledge, 1993.
- [43] P. R. Holland, „The de Broglie-Bohm theory of motion and quantum field theory“, *Physics Reports*, vol. 224, no. 3, 1993. DOI: [10.1016/0370-1573\(93\)90095-u](https://doi.org/10.1016/0370-1573(93)90095-u).
- [44] G. Bacciagaluppi and A. Valentini, *Quantum Theory at the Crossroads: Reconsidering the 1927 Solvay Conference*. Cambridge University Press, 2006. arXiv: [quant-ph/0609184v2](https://arxiv.org/abs/quant-ph/0609184v2) [[quant-ph](#)].
- [45] D. Dürr and D. Lazarovici, *Understanding Quantum Mechanics*. Springer International Publishing, 2020. DOI: [10.1007/978-3-030-40068-2](https://doi.org/10.1007/978-3-030-40068-2).

- [46] W. Heisenberg, „Über den anschaulichen Inhalt der quantentheoretischen Kinematik und Mechanik“, *Zeitschrift für Physik*, Vol. 43, 1927.
- [47] C. Kiefer, „On the interpretation of quantum theory – from Copenhagen to the present day“, 2002. arXiv: [quant-ph/0210152v1](https://arxiv.org/abs/quant-ph/0210152v1) [[quant-ph](#)].
- [48] J. S. Bell, „Speakable and unspeakable in quantum mechanics“, *Cambridge University Press*, 1987.
- [49] G. C. Ghirardi *et al.*, „Unified dynamics for microscopic and macroscopic systems“, *Physical Review D*, vol. 34, no. 2, 1986. DOI: [10.1103/physrevd.34.470](https://doi.org/10.1103/physrevd.34.470).
- [50] H. Everett, „The Theory Of The Universal Wave Function“, *Princeton University*, 1956.
- [51] D. Bohm, *Wholeness and the implicate order*. London New York: Routledge, 2002.
- [52] L. de Broglie, „An Introduction To The Study Of Wave Mechanics“, 1930.
- [53] J. S. Bell, „On the Problem of Hidden Variables in Quantum Mechanics“, *Reviews of Modern Physics*, vol. 38, no. 3, 1966. DOI: [10.1103/revmodphys.38.447](https://doi.org/10.1103/revmodphys.38.447).
- [54] G. Hermann, „Die naturphilosophischen Grundlagen der Quantenmechanik“, *Die Naturwissenschaften*, vol. 23, no. 42, 1935. DOI: [10.1007/bf01491142](https://doi.org/10.1007/bf01491142).
- [55] C. L. Herzenberg, in *Frauen in Philosophie und Wissenschaft. Women Philosophers and Scientists*, Springer Fachmedien Wiesbaden, 2019. DOI: [10.1007/978-3-658-16241-2\\_6](https://doi.org/10.1007/978-3-658-16241-2_6).
- [56] A. Einstein *et al.*, „Can Quantum-Mechanical Description of Physical Reality Be Considered Complete?“, *Physical Review*, vol. 47, no. 10, 1935. DOI: [10.1103/physrev.47.777](https://doi.org/10.1103/physrev.47.777).
- [57] A. S. Sanz, „Bohm’s approach to quantum mechanics: Alternative theory or practical picture?“, *Frontiers of Physics*, vol. 14, no. 1, 2018. DOI: [10.1007/s11467-018-0853-4](https://doi.org/10.1007/s11467-018-0853-4).
- [58] J. S. Bell, „On the Einstein Podolsky Rosen paradox“, *Physics Physique*, vol. 1, no. 3, 1964. DOI: [10.1103/physicsphysiquefizika.1.195](https://doi.org/10.1103/physicsphysiquefizika.1.195).
- [59] A. Aspect, „Bell’s Theorem: The Naive View of an Experimentalist“, in *Quantum [Un]speakables*, Springer Berlin Heidelberg, 2002. DOI: [10.1007/978-3-662-05032-3\\_9](https://doi.org/10.1007/978-3-662-05032-3_9).
- [60] M. Ghadimi *et al.*, „Nonlocality in Bell’s Theorem, in Bohm’s Theory, and in Many Interacting Worlds Theorising“, *Entropy*, vol. 20, no. 8, 2018. DOI: [10.3390/e20080567](https://doi.org/10.3390/e20080567).
- [61] S. Goldstein, „Bohmian Mechanics“, in *The Stanford Encyclopedia of Philosophy*, E. N. Zalta, Ed., Stanford University, 2017.
- [62] D. Dürr *et al.*, „Bohmian Mechanics“, 2009. arXiv: [0903.2601v1](https://arxiv.org/abs/0903.2601v1) [[quant-ph](#)].

- 
- [63] D. Bohm *et al.*, „An ontological basis for the quantum theory“, *Physics Reports*, vol. 144, no. 6, 1987. DOI: [10.1016/0370-1573\(87\)90024-x](https://doi.org/10.1016/0370-1573(87)90024-x).
- [64] E. Madelung, „Quantentheorie in hydrodynamischer Form“, *Zeitschrift für Physik*, vol. 40, no. 3-4, 1927. DOI: [10.1007/bf01400372](https://doi.org/10.1007/bf01400372).
- [65] C. Beck *et al.*, *Frequently Asked Questions about Bohmian Mechanics*, 2013.
- [66] T. Young, „The Bakerian Lecture. Experiments and calculations relative to physical optics“, *Philosophical Transactions of the Royal Society of London*, vol. 94, 1804. DOI: [10.1098/rstl.1804.0001](https://doi.org/10.1098/rstl.1804.0001).
- [67] A. Einstein, „Über die von der molekularkinetischen Theorie der Wärme geforderte Bewegung von in ruhenden Flüssigkeiten suspendierten Teilchen“, *Annalen der Physik*, vol. 322, no. 8, 1905. DOI: [10.1002/andp.19053220806](https://doi.org/10.1002/andp.19053220806).
- [68] C. Davisson and L. H. Germer, „Diffraction of Electrons by a Crystal of Nickel“, *Physical Review*, vol. 30, no. 6, 1927. DOI: [10.1103/physrev.30.705](https://doi.org/10.1103/physrev.30.705).
- [69] P. Ball, „Two slits and one hell of a quantum conundrum“, *Nature*, vol. 560, no. 7717, 2018. DOI: [10.1038/d41586-018-05892-6](https://doi.org/10.1038/d41586-018-05892-6).
- [70] Á. S. Sanz, „Particles, waves and trajectories: 210 years after Young experiment“, *Journal of Physics: Conference Series*, vol. 504, 2014. DOI: [10.1088/1742-6596/504/1/012028](https://doi.org/10.1088/1742-6596/504/1/012028).
- [71] N. Bohr, „The Quantum Postulate and the Recent Development of Atomic Theory“, *Nature*, vol. 121, no. 3050, 1928. DOI: [10.1038/121580a0](https://doi.org/10.1038/121580a0).
- [72] J. Hilgevoord and J. Uffink, „The Uncertainty Principle“, in *The Stanford Encyclopedia of Philosophy*, E. N. Zalta, Ed., Stanford University, 2017.
- [73] C. Philippidis *et al.*, „Quantum interference and the quantum potential“, *Il Nuovo Cimento B Series 11*, vol. 52, no. 1, 1979. DOI: [10.1007/bf02743566](https://doi.org/10.1007/bf02743566).
- [74] B. Braverman and C. Simon, „Proposal to Observe the Nonlocality of Bohmian Trajectories with Entangled Photons“, *Physical Review Letters*, vol. 110, no. 6, 2013. DOI: [10.1103/physrevlett.110.060406](https://doi.org/10.1103/physrevlett.110.060406).
- [75] M. O. Scully, „Do Bohm trajectories always provide a trustworthy physical picture of particle motion?“, *Physica Scripta*, vol. 1998, no. T76, 1998.
- [76] D. Dürr *et al.*, „Comment on ”Surrealistic Bohm Trajectories”“, *Zeitschrift für Naturforschung A*, vol. 48, no. 12, 1993. DOI: [10.1515/zna-1993-1219](https://doi.org/10.1515/zna-1993-1219).
- [77] C. Dewdney *et al.*, „How late measurements of quantum trajectories can fool a detector“, *Physics Letters A*, vol. 184, no. 1, 1993. DOI: [10.1016/0375-9601\(93\)90337-y](https://doi.org/10.1016/0375-9601(93)90337-y).
- [78] B. J. Hiley *et al.*, „Quantum trajectories, real, surreal or an approximation to a deeper process?“, 2000. arXiv: [quant-ph/0010020v2](https://arxiv.org/abs/quant-ph/0010020v2) [quant-ph].
- [79] B. Hiley and P. V. Reeth, „Quantum Trajectories: Real or Surreal?“, *Entropy*, vol. 20, no. 5, 2018. DOI: [10.3390/e20050353](https://doi.org/10.3390/e20050353).

- [80] J. S. Bell, „On the impossible pilot wave“, *Foundations of Physics*, vol. 12, no. 10, 1982. DOI: [10.1007/bf01889272](https://doi.org/10.1007/bf01889272).
- [81] X.-S. Ma *et al.*, „Delayed-choice gedanken experiments and their realizations“, *Reviews of Modern Physics*, vol. 88, no. 1, 2016. DOI: [10.1103/revmodphys.88.015005](https://doi.org/10.1103/revmodphys.88.015005).
- [82] K. Y. Bliokh *et al.*, „Photon trajectories, anomalous velocities and weak measurements: a classical interpretation“, *New Journal of Physics*, vol. 15, no. 7, 2013.
- [83] M. V. Berry, „Optical currents“, *Journal of Optics A: Pure and Applied Optics*, vol. 11, no. 9, 2009. DOI: [10.1088/1464-4258/11/9/094001](https://doi.org/10.1088/1464-4258/11/9/094001).
- [84] W. Zinth and U. Zinth, *Optik*. De Gruyter, 2018. DOI: [10.1515/9783110495034](https://doi.org/10.1515/9783110495034).
- [85] L. Knips *et al.*, „Multipartite Entanglement Analysis From Random Correlations“, 2019. arXiv: [1910.10732v1](https://arxiv.org/abs/1910.10732v1) [quant-ph].
- [86] B. C. Platt and R. Shack, „History and principles of Shack-Hartmann wavefront sensing.“, *Journal of refractive surgery*, vol. 17 5, 2001.
- [87] B. Saleh, *Grundlagen der Photonik*. Weinheim: Wiley-VCH, 2008.
- [88] A. E. Siegman, „How to (Maybe) Measure Laser Beam Quality“, in *DPSS Lasers: Applications and Issues*, OSA, 1998. DOI: [10.1364/dlai.1998.mq1](https://doi.org/10.1364/dlai.1998.mq1).
- [89] Edmund Optics. (2021). Application Notes, [Online]. Available: <https://www.edmundoptics.eu/knowledge-center/application-notes/optics/>.
- [90] Semrock. (2021). Filter Spectra at non-normal Angles of Incidence, [Online]. Available: <https://www.semrock.com/filter-spectra-at-non-normal-angles-of-incidence.aspx>.
- [91] E. Hecht, *Optics*. Reading, Mass: Addison-Wesley Pub. Co, 1987.
- [92] P. Trojek, „Efficient Generation of Photonic Entanglement and Multiparty Quantum Communication“, PhD thesis, 2007.
- [93] V. G. Dmitriev *et al.*, *Handbook of Nonlinear Optical Crystals*. Springer Berlin Heidelberg, 1999. DOI: [10.1007/978-3-540-46793-9](https://doi.org/10.1007/978-3-540-46793-9).
- [94] N. Boeuf, „Calculating characteristics of noncollinear phase matching in uniaxial and biaxial crystals“, *Optical Engineering*, vol. 39, no. 4, 2000. DOI: [10.1117/1.602464](https://doi.org/10.1117/1.602464).
- [95] S. Emanuelli and A. Arie, „Temperature-Dependent Dispersion Equations for KTiOPO4 and KTiOAsO4“, *Applied Optics*, vol. 42, no. 33, 2003. DOI: [10.1364/ao.42.006661](https://doi.org/10.1364/ao.42.006661).
- [96] K. Kato and E. Takaoka, „Sellmeier and thermo-optic dispersion formulas for KTP“, *Applied Optics*, vol. 41, no. 24, 2002. DOI: [10.1364/ao.41.005040](https://doi.org/10.1364/ao.41.005040).

- 
- [97] J. D. Bierlein and H. Vanherzeele, „Potassium titanyl phosphate: properties and new applications“, *Journal of the Optical Society of America B*, vol. 6, no. 4, 1989. DOI: [10.1364/josab.6.000622](https://doi.org/10.1364/josab.6.000622).
- [98] M. Fiorentino *et al.*, „Source of polarization entanglement in a single periodically poled KTiOPO4 crystal with overlapping emission cones“, *Optics Express*, vol. 13, no. 1, 2005. DOI: [10.1364/opex.13.000127](https://doi.org/10.1364/opex.13.000127).
- [99] R. Boyd, *Nonlinear optics*. San Diego, CA: Academic Press, 2003.
- [100] P. G. Evans *et al.*, „Bright source of spectrally uncorrelated polarization-entangled photons with nearly single-mode emission“, *Physical Review Letters*, Vol. 105, 253601 (2010), 2010. DOI: [10.1103/PhysRevLett.105.253601](https://doi.org/10.1103/PhysRevLett.105.253601). arXiv: [1009.1609v2](https://arxiv.org/abs/1009.1609v2) [quant-ph].
- [101] Newport Corporation. (2021). Optic Tutorials, [Online]. Available: <https://www.newport.com/resourceListing/tutorials?facetName=ProductSection&q=:relevance:resourcecategory:Optics>.
- [102] J. Shang *et al.*, „Superfast maximum likelihood reconstruction for quantum tomography“, *Phys. Rev. A* 95, 062336 (2017), 2016. DOI: [10.1103/PhysRevA.95.062336](https://doi.org/10.1103/PhysRevA.95.062336). arXiv: [1609.07881v2](https://arxiv.org/abs/1609.07881v2) [quant-ph].
- [103] C. Schwemmer *et al.*, „Systematic Errors in Current Quantum State Tomography Tools“, *Physical Review Letters*, vol. 114, no. 8, 2015. DOI: [10.1103/physrevlett.114.080403](https://doi.org/10.1103/physrevlett.114.080403).



# Acknowledgments

First of all, I want to thank Prof. Dr. Harald Weinfurter for the opportunity to work on this thesis in his group. Thank you for your support.

Thanks to all the members of the xqp group for their warm and welcoming attitude. I am especially grateful to Jan Dzwiewior and Dr. Jasmin Meinecke for their friendly and qualified assistance. Thank you, Jan, for your patient and positive way of support and the interesting conversations, and thank you, Jasmin, for the always open ear and friendly assistance. Thank you both for the company in this extraordinary situation in this Corona-year.

Special thanks to my friends, especially Ines and Sebb, who accompanied me through the whole bachelor and master studies. Without you I would never have succeeded. Thank you, Leandra, Camilla, Elena, Lavinia and Valentina, for always being there and encouraging me. My grandparents, Christa and Hans, deserve special thanks for their ongoing support and love. I would also like to thank my parents for their love and for teaching me to look at the world with open eyes and to question things.

## Acknowledgments

---

# Declaration of authorship

## **Eigenständigkeitserklärung**

Hiermit erkläre ich, Carlotta Vermold, die vorliegende Arbeit selbstständig verfasst zu haben und keine anderen als die in der Arbeit angegebenen Quellen und Hilfsmittel benutzt zu haben.

Ort, Datum

Unterschrift

